UNIVERSIDAD TÉCNICA FEDERICO SANTA MARÍA
DEPARTAMENTO DE OBRAS CIVILES
SANTIAGO - CHILE

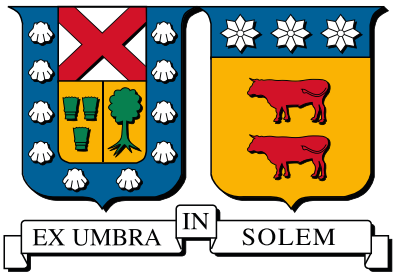

ADAPTIVE DYNAMIC COMPENSATION FOR REAL-TIME HYBRID SIMULATION TESTING

Master's Thesis by
Cristóbal Gonzalo Gálmez Villaseca

Submitted in partial fulfillment of the requirements for the degree of:
Civil Engineer
Master of Science in Civil Engineering

Advisor
Gastón Fermandois C.

August 21, 2021

A Tomás Orellana Solís...

Agradecimientos

Quiero agradecer profundamente a mis padres, Antonio Gálmez y Verónica Villaseca, por el amor que me han brindado toda la vida. A mis hermanos Sebastián, Paulina y Benjamín por todo su apoyo. A mi pareja Francisca Navarro por hacer mi vida más feliz. Y a Francisco y Minna por recibirme tan cariñosamente.

A mis amigos Abel Nova, Valentina Agusto, Diego Epuñan, Catalina Agloni y Tomás Orellana con los que reí, sufrí y viví cada día de este largo proceso. A la familia de Tomás porque les tengo un cariño enorme. A mis amigos Ignacio Ligueros, Felipe Hernandez, Christopher Faúndez y Oscar Sobarzo por esa amistad que le da sentido a la vida. A mi amigo Esteban Rebolledo que siempre ha estado presente. Y a Felipe Marchant por esas mañanas de mate en la biblioteca.

A mi profesor Gastón Fermandois por darme su apoyo y conocimientos durante este proceso. Y a mis compañeros, Diego Mera, María Quiroz y Diego Araya con quienes ha sido un agrado trabajar.

A la Universidad Técnica Federico Santa María por su apoyo través del Proyecto Interno de Línea de Investigación No. PI_L_18_07, y a la Dirección de Postgrado y Programas a través de sus becas. A la Agencia Nacional de Investigación y Desarrollo a través del proyecto FONDECYT Iniciación No. 11190774.

Abstract

Real-time hybrid simulation (RTHS) is an experimental technique to study structures subjected to dynamic excitations. A critical element of a structure is tested physically in the laboratory while the rest of the structure is modeled numerically. The interaction between substructures is imposed by a transfer system including actuators and sensors. In this technique, it is crucial to minimize synchronization errors between numerical and experimental subdomains to achieve stable and reliable results. Various dynamic compensation methods are available in the literature to control actuators in real-time. Unfortunately, the experimental substructure interacts with the actuator, so a specific compensator must be designed for each experimental substructure.

In this study, an adaptive compensation method is utilized to design a controller capable to compensate for different experimental substructures. A controller independent from the experimental substructure avoids the previous test of the physical specimen to design a controller, and the adaptation capacity allows keeping a good compensation in presence of time-varying properties of the experimental substructure. The initial conditions of the controller are defined using a model of the transfer system without considering the interaction with any experimental substructure. Then, adaptive compensation is implemented to update the control parameters during the test, maintaining excellent compensation when the experimental substructure interacts with the actuator. The proposed methodology is validated through numerical simulations in a virtual RTHS benchmark problem, but incorporating more complex scenarios such as different experimental substructures for the same controller and nonlinear experimental substructures. The results show excellent performance in terms of accuracy and robustness.

Additionally, considering the uncertain behavior of the experimental substructure interacting with the transfer system, it is essential to check the system's stability during the test execution. Therefore, an stability analysis using energy methods is performed to develop an online stability indicator for the RTHS test. This indicator's goal is to detect stability problems before it can cause excessive displacements in the system, thus damaging the physical specimen or the laboratory equipment. The effectiveness of the proposed online stability indicator is demonstrated through numerical simulations taking into account the virtual RTHS benchmark problem with different compensation designs. The proposed indicator is an excellent tool to monitor the RTHS test, improving the reliability of the experimental test while maintaining the safety of the laboratory resources.

Keywords: *real-time hybrid simulation; dynamic compensation; adaptive control; robustness; optimization*

Contents

List of Tables

List of Figures

1 Introduction

1.1 Motivation

Civil engineering structures are subjected to various external actions during their lifetime. Some of these loads are dynamic in nature, such as earthquakes, wind, or waves, and may produce complex and dangerous responses on the structures. Therefore, it is necessary to design efficient and safe structures when dealing with these natural phenomena, and laboratory tests are powerful tools for study structural systems, calibrate mathematical models, and support design methods.

In the case of earthquakes, maybe the most realistic and recognized testing method is the shake table testing (Nakashima et al., 2018; Wang et al., 2017). However, full-scale testing is extremely expensive, not only for the laboratory equipment but also by the cost of each structure, especially if it is tested until the collapse. As an alternative to shake table testing, a promising cost-effective technique called real-time hybrid simulation has been proposed (Nakashima et al., 1992; Horiuchi et al., 1999).

Real-time hybrid simulation (RTHS) combines physical testing with numerical modeling. The critical or complex elements of a structure are tested physically in the laboratory, while a numerical model represents the rest of the structural system. Due to only a portion of the structure is tested physically, the costs can be reduced considerably and it is possible to test full-scale elements.

In RTHS, the equation of motion (EOM) of the numerical substructure is solved with an integration algorithm, then, the calculated displacements are imposed over the experimental substructure using a transfer system (i.e., actuators). Finally. the experimental restoring forces are measured with sensors and incorporated into the equation of motion of the numerical substructure to calculate the displacement at the following time step (McCrum and Williams, 2016).

To capture the rate-dependent properties of the experimental structure, the boundary conditions must be imposed in real-time. This is one of the most challenging aspects of RTHS. The dynamical properties of the transfer system and its interaction with the physical specimen results in synchronization errors between the commanded and measured displacements (Dyke et al., 1995). The synchronization errors can be classified as amplitude or delay errors, and the delay errors are the most harmful for RTHS because it has been proved that delay is equivalent to introducing negative damping to the hybrid system (Horiuchi et al., 1999), which affects the accuracy of the experiment and even can cause instability in the experimental setup.

To reduce the synchronization error as much as possible, several dynamics compensation methods are available in the literature to control the transfer system connected to the experimental substructure (Carrion and Spencer, 2007; Phillips and Spencer Jr, 2011). Different compensation techniques have been demonstrated excellent performance in RTHS, but some disadvantages are recognized: (i) to obtain a control plant model, a previous test including the experimental substructure is generally performed. This previous test can alter the physical properties of the specimen. And (ii), the performance of classic compensation methods is not guaranteed if there are considerable uncertainties, non-linear behavior, or time-varying properties in the control plant.

The state of the art in RTHS consider adaptive compensation, where the control parameters are adjusted during the test to improve the performance in presence of uncertainties or unmodeled dynamics (Wallace et al., 2005b; Bonnet et al., 2007). Adaptive compensation has been demonstrated excellent performance, but the design and calibration depend on several parameters, initial conditions, and

adaptation constraints, therefore, it generally requires a good knowledge of the control plant including the experimental substructure which usually requires previous system identification or expertise tuning of several parameters.

1.2 Study Objective

The goal of this study is to design a robust adaptive dynamic compensator for real-time hybrid simulation, capable to compensate the transfer system dynamics connected to different uncertain experimental substructures, avoiding the previous testing that includes the physical specimen. Specific objectives are the following:

- To define a control architecture and adaptive laws that can be implemented without testing the physical specimen giving a detailed explanation of the design and calibration process.
- To define a methodology to detect stability issues before and during the test.
- Perform a numerical validation of the proposed methodology, including different experimental substructures and non-linear behaviors.

1.3 Organization of the document

- Chapter 2 presents a literature review about real-time hybrid simulation with a main focus in the state-of-the-art in dynamic compensation in section 2.3.
- Chapter 3 describes the substructuring problem in RTHS for the typical configurations with one actuator or using a shake table as a transfer system. Both cases include examples with numerical simulations.
- Chapter 4 presents the most utilized servo-hydraulic transfer system mathematical models, and the interaction between the transfer system and the physical specimen is analyzed.
- Chapter 5 studies the available stability analysis for real-time hybrid simulation, and an on-line stability indicator is developed to detect instability problems during a test.
- Chapter 6 presents the proposed compensation technique: the adaptive model-based compensation.
- Chapter 7 contains the numerical validation of the proposed compensation schemes. Section 7.1 describes the benchmark problem (Silva et al., 2020) selected as platform for the numerical validation. Section 7.2 presents the design and calibration process for the proposed compensation method. Section 7.3 presents the compensation results and analyze the performance and robustness of the compensator. Finally, Section 7.4 presents the implementation of the proposed stability indicator on the benchmark problem for different stable and unstable cases.
- Chapter 8 provides the conclusions of this study, and recognize possible directions to improve the proposed methodology.

2 Literature Review

2.1 Experimental testing in structural engineering

Earthquakes are complex phenomena that can be extremely dangerous for civil engineering structures and therefore for the safety of the people. Thus, it is imperative to provide a resilient infrastructure for society. Design codes and computational analysis are in constant improvement to achieve this goal. However, it should be noted that both, design codes and computational analysis base their methodology on results from experimental testing. This is more evident when new materials, structural components, or control systems are developed. Therefore, experimental testing is crucial to validate and calibrate mathematical models that allow analyzing the response of those systems with accuracy.

The most utilized seismic testing methods are the quasi-static test and the shake table test. In the quasi-static test, a predefined displacement is imposed on the physical specimen generally on an extended time scale (Carrion and Spencer, 2007). The displacements are applied cyclically with incremental amplitude, allowing to study the response of structural components against cyclic loads. This method has been useful to quantify the capacity of structural systems and develop equations and specifications for building codes (Nakashima, 2020). On the other hand, the shake table tests consist of mounting an entire structure on a rigid base connected to dynamic actuators capable to produce a ground motion. This test is executed in real-time, which allows capturing dynamic effects such as inertial forces and rate-dependant properties of structural components.

The shake table tests provide realistic seismic conditions but requires very expensive installations to test full-scale specimens, which results in the widespread use of scale models (McCrum and Williams, 2016). The reduced-scale model does not necessarily represent the behavior of local phenomena in particular elements, such as local buckling, welding effects or crack propagation, among others (Carrion and Spencer, 2007). On the other hand, the quasi-static test allows to study structural components at more realistic scales with smaller costs, but the predefined imposed displacement, may not be representative of the loading conditions during an earthquake (Dermitzakis and Mahin, 1985).

The need for low-cost and realistic seismic tests led researchers to develop new alternatives, this is how the pseudo-dynamic test (PsD) was introduced, giving way to hybrid and real-time hybrid simulation.

2.2 Hybrid simulation: from pseudo-dynamic to real-time tests

The first approximation to pseudo-dynamic test (PsD) was proposed in 1969 by Hakuno et al. (Hakuno et al., 1969), where an analog computer was utilized to solve a single degree of freedom equation of motion. The mass and damping were numerically represented while the restitutive force was obtained from a physical specimen. The pseudo-dynamic test was later formalized by Takanashi et al. in 1975 (Takanashi et al., 1975) who discretized the equation of motion in time domain to utilize a digital computer to solve it. Since the damage in structures is generally a local phenomenon, the structure does not need to be entirely physically tested. The concept of substructuring in PsD testing allows modeling physically the critical elements of a structure while the rest is modeled numerically. Substructured PsD testing was formally introduced by Dermitzakis & Mahin in 1985 (Dermitzakis and Mahin, 1985). The substructured pseudo-dynamic test is widely named as hybrid simulation test.

In a pseudo-dynamic test or conventional hybrid simulation, the equation of motion is solved in an extended time-scale which gives more time for the numerical calculations and allows a slow control of the actuators. However, an extended time scale does not enable to capture of the rate-dependent properties of the experimental substructure. For this reason, researchers have shown great interest in executing hybrid testing in real-time. In 1992, Nakashima et al. (Nakashima et al., 1992) present the first real-time pseudo-dynamic test. Real-time hybrid simulation (RTHS) is an excellent tool for testing rate-dependent devices such as passive, semi-active, and active control devices. In RTHS, the numerical substructure is subjected to the ground motion, and its equation of motion is solved at each time step to obtain the displacement to be imposed on the experimental substructure. Then, the displacements are imposed using dynamic actuators and the forces required to imposed these displacements are measured with sensors and fed back to the numerical substructure to compute the response at the next time step. A graphical scheme of the RTHS procedure is shown in Fig. 2.1.

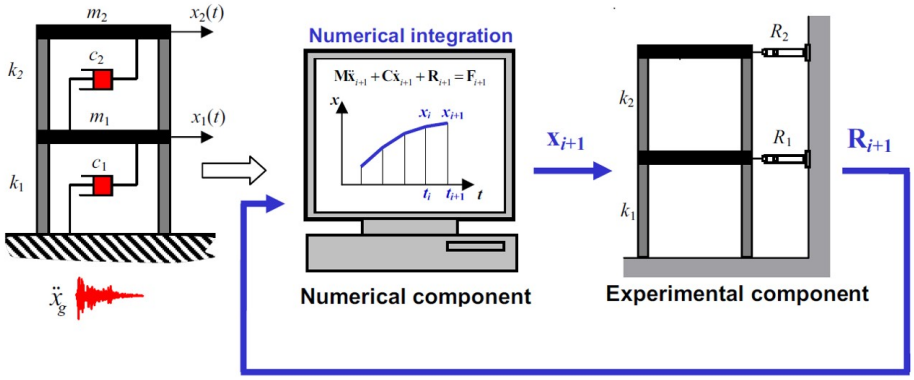

Figure 2.1: Real-time hybrid simulation scheme (Carrion and Spencer, 2007).

In the last decades, a lot of research around real-time hybrid simulation has been developed. Complete reviews including research and applications can be found in McCrum and Williams (2016) and Shao and Griffith (2013). Several lines of investigation are under constant development, for example, the integration methods and mathematical models (Bas and Moustafa, 2020; Wang et al., 2001) are constantly studied to improve stability and reliability.

Various integration methods are based on the Newmark method (Newmark, 1959) which can be explicit or implicit depending on the selection of integration parameters. However, in real-time hybrid simulation, explicit integration methods have been preferred over implicit methods due to the computational costs. The central difference method (CDM) is one of the most utilized integration methods in RTHS, which is conditionally stable, and therefore the time step and natural frequencies of the system should be carefully studied. Different modifications have been proposed to improve the stability of Newmark methods, such as the $HHT-\alpha$ method (Hilber et al., 1977) to allow the introduction of numerical damping for superior modes without major compromise of accuracy.

For another side, a technique known as model updating is implemented to update the numerical models during the test based on information obtained from the experimental substructure (Ou et al., 2017; Mei et al., 2019).

Other techniques consider the combination of hybrid simulation with shake table testing, where only

a part of the structure is mounted over the shake table, and the interface accelerations are calculated during the test Ashasi-Sorkhabi et al. (2015); Zhang et al. (2017).

Since hybrid simulation allows to divide a structure into two or more parts, it is possible to perform collaboration between remote laboratories, this technique is known as geographically distributed hybrid simulation (Takahashi and Fenves, 2006; Park et al., 2005).

However, one of the aspects that attracts more attention in the RTHS community is the correct application of the boundary conditions on the experimental substructure. Since the transfer systems utilized to impose displacements, i.e. actuators or shake tables, are dynamical systems, their response is delayed concerning their inputs. This issue leads to a dynamic compensation problem that has been treated with different strategies based on control theory.

2.3 Dynamic compensation in RTHS

In RTHS, it is crucial to ensure the compatibility of displacements and the force equilibrium at the interface between physical and numerical subdomains. For compatibility, a transfer system is utilized to impose the numerical substructure's response on the experimental substructure. If the numerical and experimental displacements are synchronized, the measured forces on the experimental substructure are considered as reliable, satisfying the force equilibrium.

However, displacement synchronization is very difficult to achieve in real-time. The transfer system is a dynamical system itself, and additionally, it interacts with the physical specimen, producing discrepancies between the commanded and measured displacements. This phenomenon is known as control-structure interaction (Dyke et al., 1995). Therefore, to reduce the synchronization error, a controller is implemented between the numerical substructure and the transfer system. In Fig. 2.2, the tracking problem is schematized. A target displacement x_t comes from the numerical substructure and is processed in the controller to generate the command signal x_c for the transfer system with the attached experimental substructure. The subsystem composed by the transfer system and the physical specimen is namely herein as control plant. Finally, the achieved displacement x_m is measured and is sent back to the controller. The goal of the dynamic compensation is to reduce the synchronization error $e = x_t - x_m$, and several methods has been proposed in the literature.

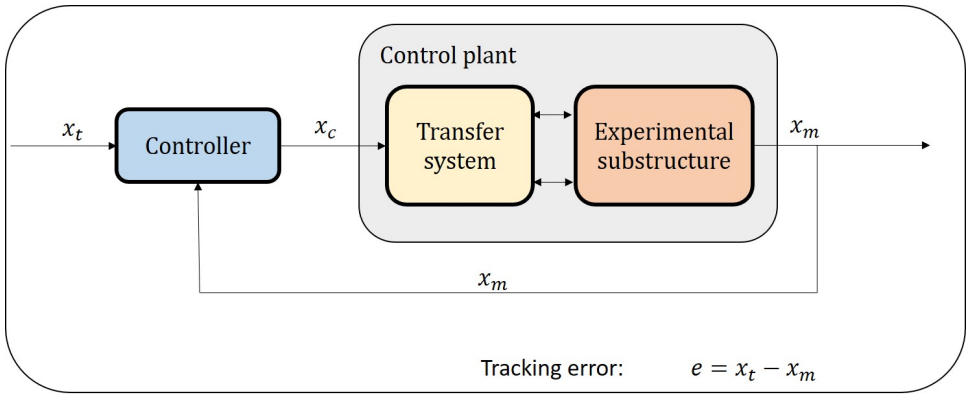

Figure 2.2: Tracking problem in RTHS.

The synchronization errors can be classified as amplitude or delay errors. In 1996, Horiuchi et al. demonstrate that the actuator delay is equivalent to introduce negative damping to the hybrid system (Horiuchi et al., 1996). If the negative damping overcomes the inherent damping of the system, the response becomes unstable, i.e. the displacements tend to grow up without limit. Therefore, the earlier compensation methods attend to compensate for the actuator delay. The most widely used method is known as polynomial extrapolation (Horiuchi et al., 1996, 1999). In this method, the actuator delay is assumed as a constant value, so the actuator response after the time delay is estimated through the polynomial extrapolation, then, instead of command the desired displacement, the estimated displacement is commanded, and due to the delay, the achieved response is close to the desired one.

However, the time delay of an actuator is not a constant value, it depends on the commanded frequencies. Consequently, more sophisticated methods were implemented. Chen et al. proposed the utilization of first-order discrete transfer function to model the actuator dynamics and compensate it dynamics through inverse compensation (Chen, 2007). Another similar approach based on first-order transfer function is the phase-lead compensator implemented by Zhao (Zhao et al., 2003).

More complex control strategies are the model-based compensation techniques, where different control tools are applied based on a higher-order model of the actuator connected to the experimental substructure (Carrion and Spencer, 2007). In 2011, Phillips and Spencer (Phillips and Spencer Jr, 2011) proposed a feedforward-feedback compensation scheme shown in Fig. 2.3. In this method, the feedforward controller is based on the inverse of the control plant, so its function is to compensate the modeled dynamics of the plant and only takes the desired displacement as input (r in Fig. 2.3). On the other hand, in parallel, a feedback controller takes the tracking error to generate a command signal, improving the robustness of the compensation. The feedback controller consists of a Linear Quadratic Gaussian Regulator (LQG). The LQG controller is composed of a Kalman filter designed to estimate the states of the control plant and a Linear Quadratic Regulator designed to minimize the tracking error.

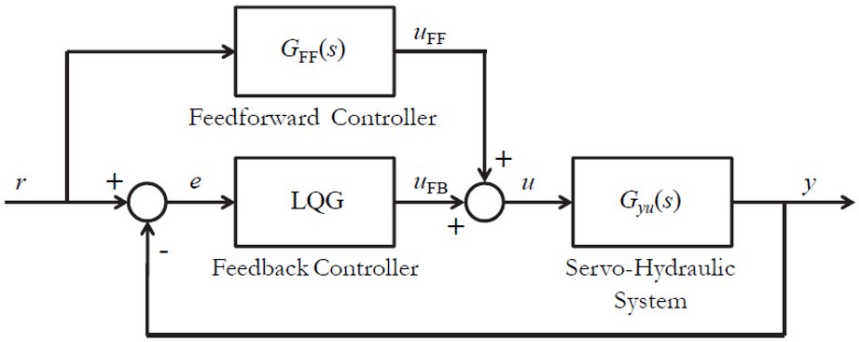

Figure 2.3: Feedforward-feedback compensation scheme (Phillips and Spencer Jr, 2011).

Recently, Najafi and Spencer proposed another architecture to the feedback-feedforward control (Najafi and Spencer Jr., 2020). Instead of the controllers in parallel, the feedforward controller is placed in series with the control plant, and the feedback controller is designed for an augmented plant considering the control plant and the feedforward controller as a new control plant.

Other authors such as Gao et al. or Ou et al (Gao et al., 2013; Ou et al., 2015) consider H_∞

feedback control, where noise, disturbances, and model uncertainties are considered in the design. The controller is designed by trading off tracking performance and robustness.

Model-based strategies have been demonstrated excellent performance in RTHS, especially if an accurate model of the control plant is available. Nevertheless, the uncertainty in the identified model may affect the accuracy of the controller. Additionally, the model-based strategies are generally based on linear time-invariant systems, while the actual properties of the control plant can exhibit non-linear behaviors or time-varying properties during the test. For this reason, the researchers have been applied more sophisticated control techniques such as non-linear control and adaptive control.

Adaptive control consists of a combination of control law and an adaptive law. The control law generates the command signal taking the target and measurement displacements, and depends on a set of control parameters. On the other hand, the adaptive law adjusts the control parameters using the information obtained during the test (Ioannou and Sun, 2012). In RTHS, earlier adaptive methods consider simple control strategies, and the adaptive laws were focused on estimate the actuator delay during the test (Wallace et al., 2005a; Bonnet et al., 2007). Other methods such as the Tracking Error Based Adaptive compensator by Chen et al. (Chen and Ricles, 2010) are based on a first-order transfer function as control law and one adaptive parameter based on the synchronization error integrated on time. On the other hand, Adaptive Phase Lead Compensator (APLC) by Tao et al. (Tao and Mercan, 2019), and Windowed Frequency Evaluation Index Compensation (WFEI) (Xu et al., 2019b) also consider first-order transfer functions for control, but the adaptation is based on a frequency domain analysis using Fast Fourier Transform FFT. For example, the APLC flow chart is presented in Fig. 2.4. Even though first-order adaptive controllers offer simple designs based on a few control parameters, their performance is limited compared to more sophisticated controllers, moreover, frequency domain adaptation is complex and less effective than others adaptive laws.

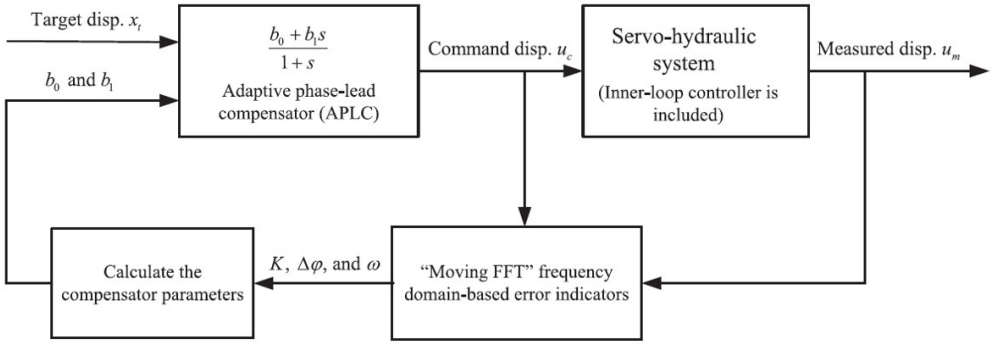

Figure 2.4: Adaptive Phase Lead Compensator flow chart (Tao and Mercan, 2019).

Effective and simple methods that can be classified as adaptive feedforward are described next. The Adaptive Time Series (ATS) proposed by Chae et al. (Chae et al., 2013) consists in approximating the control plant input-output relationship as a Taylor series expansion. The controller order depends on the number of coefficients in the expansion, but two or three terms are recommended by the authors. The adaptation is based on the least-square method (LS), and is implemented using the measured and commanded data during the test. Although the least-square method provides an excellent estimation of the required parameters, its calculation involves the inversion of a matrix at each time step, which

can be a restrictive issue considering the small time steps used in RTHS. Therefore, a modification to the ATS was proposed by Palacio-Betancur et al. (Palacio-Betancur and Gutierrez Soto, 2019) named as Conditional Adaptive Time Series (CATS). The control and adaptation architecture is equivalent to the ATS, but instead of the conventional least-square method, the recursive least-square (RLS) method was introduced. The RLS method is more cost-effective than the LS, but requires the selection of design parameters less intuitive than the LS. The CATS flow chart for a first-order controller is presented in Fig. 2.5. The block that contains $A_k = f(x_m, \dot{x}_m, x_c^1)$ represents the LS or RLS method to adapt the control parameters α_{0k} and α_{1k}.

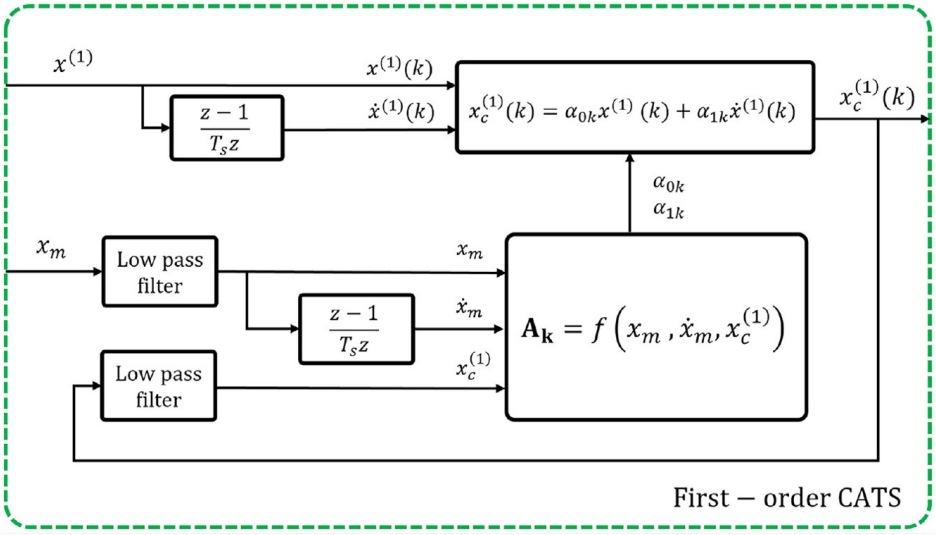

Figure 2.5: Conditional Adaptive Time Series flow chart (Palacio-Betancur and Gutierrez Soto, 2019).

On the other hand, Chen et al. (Chen et al., 2015) proposed the Adaptive Model-based compensator (AMB), which consists of an adaptive feedforward combined with a conventional LQG controller. The adaptive feedforward consists of the inverse of a frequency domain model of the control plant. After the implementation, the architecture results very similar to the ATS and the CATS, but with a different adaptive law. In this case, a gradient adaptive law is defined instead of LS or RLS. The proposed methodology of this study is based on the Adaptive Model-based compensation, so the detailed description of the method is presented in Chapter 6.

The above adaptive feedforward methods (ATS, CATS, and AMB) are formulated based on continuous-time dynamic models, but for the implementation of digital controllers, discrete forms are required. As an alternative, some methods are directly formulated in discrete time. Wang et al. proposed the Two-stage Adaptive Compensator (Wang et al., 2020), where the estimated delay is compensated through the classic polynomial extrapolation, while the uncompensated delay or non-modeled dynamics are compensated using a discrete adaptive feedforward approach with adaptation based on RLS method. Other discrete methods have been proposed using the conventional LS method (Ning et al., 2020a) or discrete Kalman filter to identify the better control parameters (Ning et al., 2020b). Simpson et al. presented a detailed study of discrete data driven adaptive control for RTHS plants (Simpson et al., 2020). Data-driven controllers offer wide flexibility for some design choices such as the controller order, and does not need continuous dynamic models of the control plant. However, it also requires careful

tuning of adaptation parameters.

The flow chart of the Adaptive Discrete Feedforward (ADF) compensation by Ning et al. (Ning et al., 2020a) is presented in Fig. 2.6. Notice that the control and adaptation are very similar to the CATS in Fig. 2.5. The difference is that CATS depends on the target and measured signals and their derivatives, while ADF takes the signals and their values at past time steps. Avoiding numerical derivatives is considered an advantage since noise in measurement can affect the calculation of derivatives.

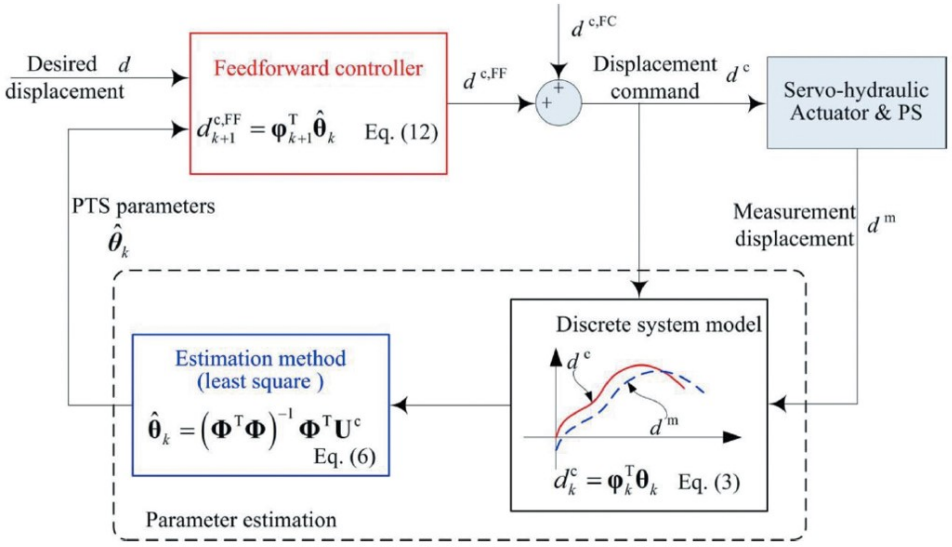

Figure 2.6: Adaptive Discrete Feedforward compensation flow chart (Ning et al., 2020a).

Other different control techniques are based on non-linear control theory. Xu et al. proposed the use of the non-linear technique called Sliding Mode Control (SMC) in combination with Improved Polynomial-based Adaptive Forward predictor (IAPF) (Xu et al., 2019a). Maghareh et al. also introduced the use of Sliding Mode Control in the proposed Self-tuning Robust Control System (SRCSys), where the control consists of two layers, a robustness layer based on Sliding Mode Control, and an adaptation layer to improve the accuracy during a test. The Sliding Mode Control consists in force the control plant to reach and hold a sliding manifold in a finite time. The manifold is designed to achieve the control objective (Khalil and Grizzle, 2002). Sliding Mode Control is a robust and flexible control tool, however, its design is based on Lyapunov function to ensure asymptotically convergence, therefore, to fulfill the RTHS requirements in a short time, the control law must be carefully calibrated. A different non-linear control technique that has been applied to RTHS problem is the Backstepping Adaptive Control (BAC) by Ouyang et al. (Ouyang et al., 2019), which consists in transform the full system into a sequence of design problems of lower order. The flow chart of BAC control is presented in Fig. 2.7 This method offers the possibility of dispense with the structural properties of the physical specimen, nevertheless, the design requires the calibration of several parameters which can be challenging, especially for this complex strategy.

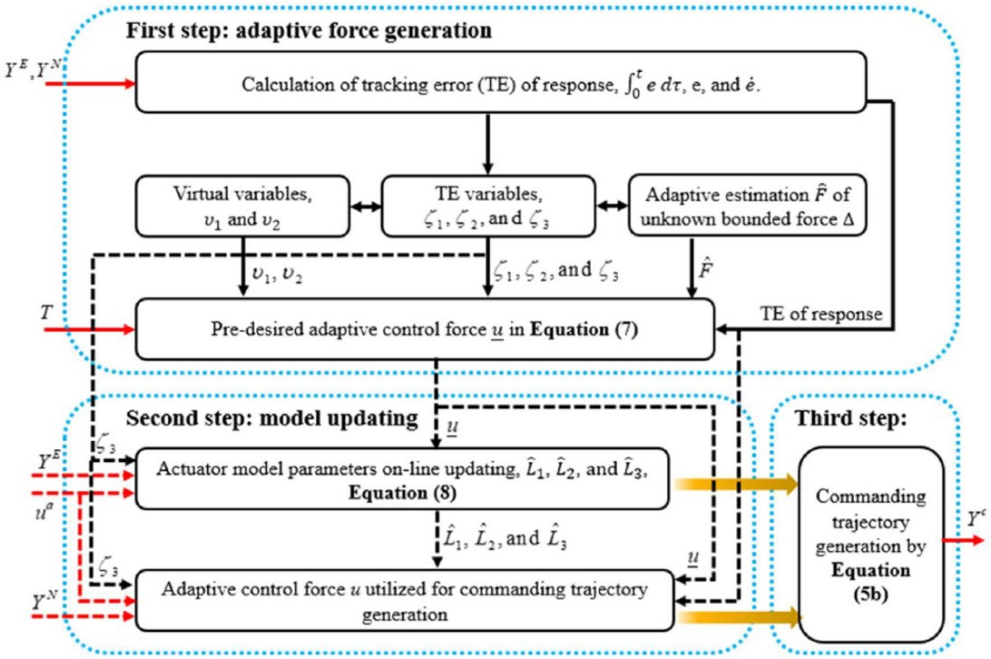

Fig. 2. Adaptive outer-loop controller for time-lag compensation.

Figure 2.7: Backstepping Adaptive Compensator flow chart (Ouyang et al., 2019).

Some alternatives methods are listed herein. Tsokanas et al. introduced the use of Model Predictive Control (MPC) combined with polynomial extrapolation (Tsokanas et al., 2020). MPC consists of a controller where an optimization algorithm is implemented during the test to predict the response for a finite horizon and make the control decision according to new information.

Verma et al. proposed a novel scheme namely Impedance Matching Control (IMC) (Verma and Sivaselvan, 2019), where the classic tracking problem is transformed into a problem in which the goal is to find the control input such that the actuator displaces the same as the numerical substructure would in response to the force from the experimental substructure and the ground motion input. This strategy dismisses a model of the physical specimen but requires a detailed model of each component in the transfer system.

Peiris et al. introduced the passivity control in RTHS (Peiris et al., 2020), where a virtual damper is added between physical and numerical substructure in order to cancel the negative damping produced by the actuator delay. This technique can stabilize the hybrid system but does not solve the synchronization problem, and therefore, the test could lose precision.

From all the reviewed methods, Adaptive Model-based Compensation (AMB) is considered the best alternative to design a controller without prior testing of the physical specimen. An adaptive feedforward controller offers excellent delay compensation and allows to minimize amplitude error at the same time. However, the design and calibration for an extremely uncertain plant is challenging, so the detailed study is presented in Chapter 6 and then implemented in Chapter 7.

3 Substructuring in RTHS

3.1 Dynamic models

In this study, linear dynamical systems are modeled with two very useful representations, the state-space model and the transfer function. Non-linear models are only treated in Section 7.3.3, where the non-linear equations are presented.

Thus, consider the differential equation of motion (EOM) of a multiple degrees of freedom (MDOF) linear structure subjected to a ground motion:

$$M\ddot{x}(t) + C\dot{x}(t) + Kx(t) = -M\Upsilon\ddot{u}_g(t) \tag{3.1}$$

where M, C, and K are the mass, damping, and stiffness matrices, respectively. $x(t)$, $\dot{x}(t)$, and $\ddot{x}(t)$ are the displacement, velocity, and accelerations vectors, respectively, all measured relative to the ground motion. $\ddot{u}_g(t)$ is the ground acceleration, and Υ is the seismic influence vector.

The second-order differential equation in Eq. (3.1) can be rewritten into a first-order differential equation in form of state-space (SS) representation:

$$\{\dot{\mathbf{x}}\} = [A]\{\mathbf{x}\} + [B]\{u\} \tag{3.2}$$

$$\{\mathbf{y}\} = [C]\{\mathbf{x}\} + [D]\{u\} \tag{3.3}$$

Taking the state vector as $\mathbf{x} = \begin{Bmatrix} x \\ \dot{x} \end{Bmatrix}$, and the output vector as $\mathbf{y} = \begin{Bmatrix} x \\ \dot{x} \\ \ddot{x}_{abs} \end{Bmatrix}$; the equation (3.1) rewritten in SS form results as:

$$\begin{Bmatrix} \dot{x} \\ \ddot{x} \end{Bmatrix} = \begin{bmatrix} [0] & [I] \\ -M^{-1}K & -M^{-1}C \end{bmatrix} \begin{Bmatrix} x \\ \dot{x} \end{Bmatrix} + \begin{bmatrix} [0] \\ -\Upsilon \end{bmatrix} \{\ddot{u}_g\} \tag{3.4}$$

$$\begin{Bmatrix} x \\ \dot{x} \\ \ddot{x}_{abs} \end{Bmatrix} = \begin{bmatrix} [I] & [0] \\ [0] & [I] \\ -M^{-1}K & -M^{-1}C \end{bmatrix} \begin{Bmatrix} x \\ \dot{x} \end{Bmatrix} + \begin{bmatrix} [0] \\ [0] \\ [0] \end{bmatrix} \{\ddot{u}_g\} \tag{3.5}$$

where [0] is a matrix of zeros, and $[I]$ is the identity matrix. $\ddot{x}_{abs}$ is the absolute accelerations vector. Equation (3.4) consists of a first-order matrix differential equation, therefore, different numeric solvers can be applied to solve it. Equation (3.5) is used to construct the output using the obtained states. In this study, the SS differential equation is solved using Simulink from Matlab. The block diagram of the SS model is presented in Fig. 3.1.

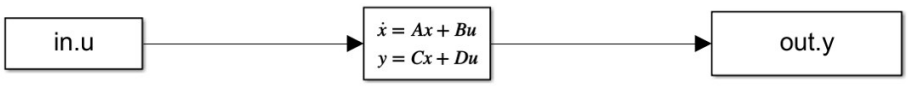

Figure 3.1: State-space model in Simulink

The other dynamic representation used in this study is the transfer function in the Laplace domain. Consider a single input - single output system, for example, a single degree of freedom structure subjected to an external force:

$$m\ddot{x}(t) + c\dot{x}(t) + kx(t) = F(t) \tag{3.6}$$

where m, c, k and $F(t)$ are the mass, damping, stiffness, and external force respectively. Taking the Laplace Transform in Equation (3.6) and solving for displacement:

$$x(s) = \frac{1}{ms^2 + cs + k} F(s) = G_{xf} F(s) \tag{3.7}$$

where s is the Laplace variable and G_{xf} is the transfer function from force to displacement of the dynamical system. Proper transfer functions, i.e. functions with numerator's order less or equal than the denominator's order can be solved in Simulink with the transfer function model presented in Fig. 3.2.

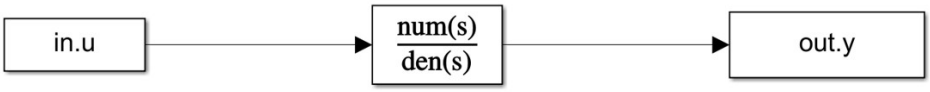

Figure 3.2: Transfer function model in Simulink

In this study, the selected integration method for all numerical simulations is the 4^{th} order Runge-Kutta with a fixed step of 1/4096 sec.

3.2 Substructuring using actuator

The complete structure to emulate is named herein as reference structure. Consider a reference structure subjected to a ground acceleration as shown in Fig. 3.3. The reference structure is separated into a numerical substructure and an experimental substructure. The boundary conditions of the degree of freedom at the interface between substructures x_{n1} is imposed by an actuator over the experimental substructure. In terms of equations, the substructuring is described as follows. The equation of motion (EOM) of the reference structure (subscript r) is expressed as:

$$M_r\ddot{x}_r(t) + C_r\dot{x}_r(t) + K_r x_r(t) = -M_r \Upsilon \ddot{u}_g(t) \tag{3.8}$$

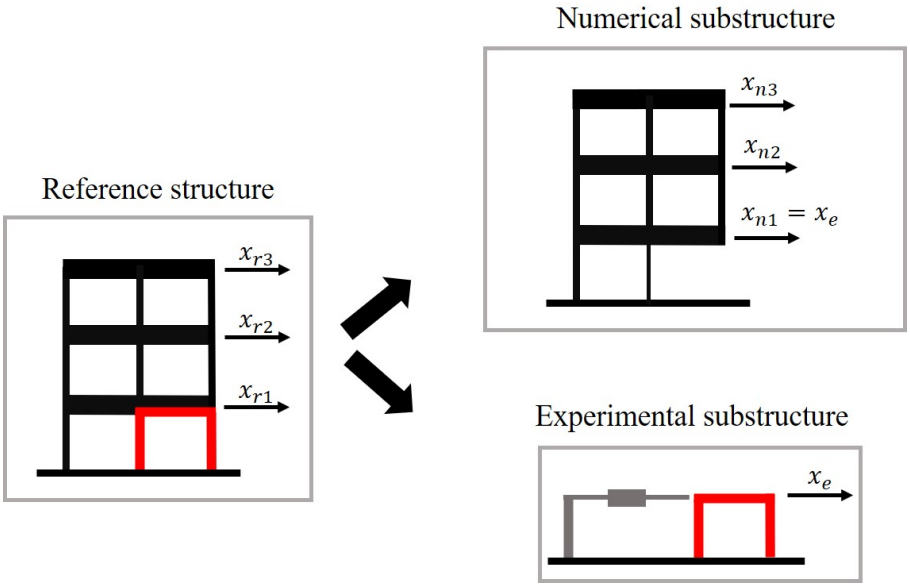

Figure 3.3: Real-time hybrid simulation substructuring example.

where M_r, K_r, and C_r are the mass, stiffness and damping matrices, respectively. $x_r(t)$, $\dot{x}_r(t)$, and $\ddot{x}_r(t)$ are the displacement, velocity, and accelerations vectors, respectively, all measured relative to the ground motion. $\ddot{u}_g(t)$ is the ground acceleration, and Υ is the seismic influence vector.

The reference structure is separated into the numerical (subscript n) and experimental (subscript e) substructures:

$$(M_n + M_e)\,\ddot{x}_r(t) + (C_n + C_e)\,\dot{x}_r(t) + (K_n + K_e)\,x_r(t) = -\,(M_n + M_e)\,\Upsilon\ddot{u}_g(t) \tag{3.9}$$

Then, the EOM of the numerical substructure can be rewritten:

$$M_n\ddot{x}_n(t) + C_n\dot{x}_n(t) + K_n x_n(t) = -(M_n + M_e)\Upsilon\ddot{u}_g(t) - F_e(t) \tag{3.10}$$

where $x_n(t)$, $\dot{x}_n(t)$ and $\ddot{x}_n(t)$ corresponds to the displacement, velocity and acceleration of the numerical substructure, all relative to the ground motion. Notice that the earthquake equivalent forces of both substructures are included in the EOM of the numerical substructure. Additionally, F_e corresponds to the feedback forces from the experimental substructure:

$$F_e(t) = M_e\ddot{x}_e(t) + C_e\dot{x}_e(t) + K_e x_e(t) \tag{3.11}$$

where $x_e(t)$, $\dot{x}_e(t)$ and $\ddot{x}_e(t)$ corresponds to the experimental displacement, velocity and acceleration of the experimental substructure, and in the ideal case, the actuator impose $x_e = x_{n1}$.

Notice that the feedback forces include inertial, viscous, and restorative forces. The inertial force only depends on the relative accelerations, since the ground acceleration is considered in the numerical substructure EOM. Furthermore, in a general case, the viscous and restorative forces can be complex non-linear forces, thus, the feedback force can be expressed as:

$$F_e(t) = M_e\ddot{x}_e(t) + r_e(t) \tag{3.12}$$

where $r_e(t)$ is the restorative force of the experimental substructure.

3.3 Substructuring with shake table

Although hybrid simulation appears as an alternative to shake table testing, there exists a type of hybrid simulation where a shake table is utilized as a transfer system. As shown in Fig. 3.4, a reference structure is divided into two portions. The lower substructure is modeled numerically, while the upper substructure is mounted over the shake table. This configuration is useful to study protective systems such as tuned mass dampers (TMD), tuned liquid dampers (TLD) (Ashasi-Sorkhabi et al., 2015), or inter-story isolation devices (Zhang et al., 2017).

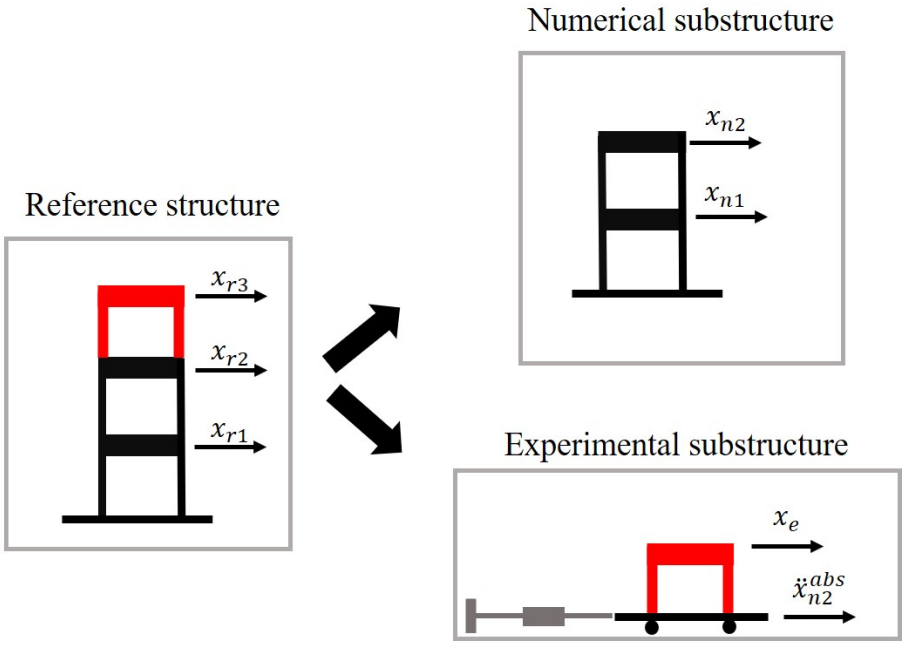

Figure 3.4: Real-time hybrid simulation substructuring example using shake table.

In this case, the equation of motion of the numerical substructure is:

$$M_n\ddot{x}_n(t) + C_n\dot{x}_n(t) + K_n x_n(t) = -M_n\Upsilon\ddot{u}_g(t) - F_e(t) \tag{3.13}$$

where $x_n(t)$, $\dot{x}_n(t)$ and $\ddot{x}_n(t)$ corresponds to the displacement, velocity and acceleration of the numerical substructure, all relative to the ground motion. The numerical substructure's top floor absolute acceleration is the target acceleration for the shake table. Thus, in contrast to a conventional shake table test, in RTHS, the shake table input is unknown prior to the test. Finally, the feedback force F_e, in this case, corresponds to the transmitted force by the experimental substructure which can be obtained from the inertial forces:

$$F_e(t) = M_e \ddot{x}_e^{abs}(t) \tag{3.14}$$

where $\ddot{x}_e^{abs}$ corresponds to the absolute acceleration of the experimental substructure. As an alternative, in the laboratory, this feedback force can be directly measured with load cells.

Notice that in RTHS with a shake table, the displacement tracking problem is replaced by an acceleration tracking problem. Although the target acceleration can be integrated to obtain the target displacement and thus control the transfer system by displacements, it does not ensure accurate acceleration tracking (Tang et al., 2020). Even though, similar techniques can be applied for both displacement tracking and acceleration tracking. However, in this study, the focus is on the displacement tracking problem, especially for servo-hydraulic actuators.

4 Transfer System Dynamics

4.1 Servo-hydraulic actuator model

Servo-hydraulic actuators are often used as transfer system in RTHS due to their capacity to impose displacements at the frequencies of interest for seismic assessment. A detailed model of the transfer system was presented by Dyke et al. (Dyke et al., 1995), where the interaction between the actuator and the physical specimen was modeled and analyzed. The model described herein can be found in (Carrion and Spencer, 2007) and is equivalent to other models presented by Dyke et al. (Dyke et al., 1995) and Maghareh et al. (Maghareh et al., 2018) (These models are based on the same physical equations, but the models may vary depending on how the block diagrams are grouped). The block diagram of a servo-hydraulic system coupled with a physical specimen is presented in Fig. 4.1.

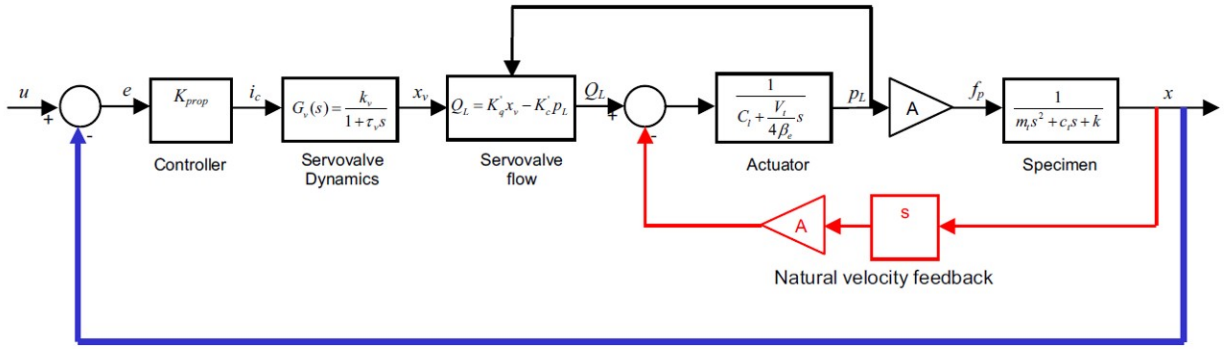

Figure 4.1: Servo-hydraulic actuator model coupled with physical specimen (Carrion and Spencer, 2007).

The input of the transfer system is the commanded displacement u, and then, the error e between the actual displacement x and u, i.e. $e = u - x$, is sent to the internal controller of the servo-hydraulic system to generate the servo-valve input i_c:

$$i_c = K_{prop} e = K_{prop}(u - x) \tag{4.1}$$

where K_{prop} is the internal proportional controller gain. In some servo-hydraulic systems, instead of proportional control, a proportional-integral-derivative control (PID) is implemented. In those cases, the servo-valve input is obtained by:

$$i_c(s) = \left(K_{prop} + \frac{K_{int}}{s} + K_{der} s \right) e(s) \tag{4.2}$$

where K_{int} is the integral gain, and K_{der} is the derivative gain. However, in this section, only proportional control is considered. This internal controller must not be confused with the dynamic compensation method implemented in an external controller. The internal controller is part of the servo-hydraulic system, while the external controller is generally used to compensate for the servo-hydraulic dynamics (including its internal control).

Once the servo-valve input is generated, the servo-valve dynamics can be modeled as a transfer function $G_v(s)$ that generates the spool displacement in the valve x_v:

$$x_v(s) = G_v(s)i_c(s) = \frac{k_v}{1+\tau s}i_c(s) \tag{4.3}$$

where k_v is the servo-valve gain, and τ is the servo-valve time constant. Then, the continuity equation governs the servo-valve flow:

$$Q_L = K'_q x_v - K'_c p_L \tag{4.4}$$

where K'_q is the valve flow gain, K'_q is the valve flow pressure gain, and p_L is the pressure drop. On the other hand, the flow on the actuator is defined by:

$$Q_L = A\dot{x} + C_l p_L + \frac{V}{4\beta}\dot{p}_L \tag{4.5}$$

where A is the area of the actuator piston, C_l is the leakage coefficient on the piston, V is the total fluid volume, and β is the bulk modulus of the fluid. Then, a transfer function model of the actuator can be obtained:

$$p_L = \frac{1}{C_l + \frac{V}{4\beta}s}\left(Q_L(s) - Asx(s)\right) \tag{4.6}$$

Alternatively, by combining the continuity equations (4.4) and (4.5), an equation for the actuator's piston force f_p is obtained:

$$f_p = Ap_L \tag{4.7}$$

$$\dot{f}_p = \frac{4\beta}{V}\left(AK'_q k_v i_c - (K'_c + C_l)f_p - A^2\dot{x}\right) \tag{4.8}$$

Notice that the actuator force is directly affected by the physical specimen response by natural velocity feedback. Finally, the specimen response is governed by the equilibrium force between the actuator piston and EOM of the physical specimen:

$$m\ddot{x} + c\dot{x} + kx = f_p \tag{4.9}$$

where m is the total mass of the physical specimen and piston, c is the viscous damping coefficient of the specimen and the piston, and k is the specimen stiffness. The physical specimen EOM in equation (4.9) can be expressed in the Laplace domain:

$$x(s) = \frac{1}{ms^2 + cs + k}f_p(s) \tag{4.10}$$

Alternatively, an equivalent model presented by Maghareh et al. (Maghareh et al., 2018) considered lumped parameters as shown in Fig. 4.2. In this case the lumped parameters are related to the physical actuator parameters by:

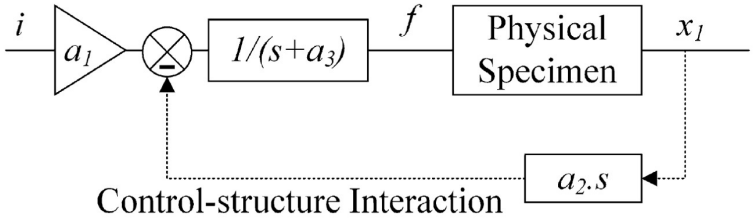

Figure 4.2: Simplified actuator model coupled with physical specimen (Maghareh et al., 2018)

$$a_1 = \frac{4\beta K_q A}{V} \tag{4.11}$$

$$a_2 = \frac{4\beta A^2}{V} \tag{4.12}$$

$$a_3 = \frac{4\beta K_c}{V} \tag{4.13}$$

where $K_q = K'_q k_v$ is the total servo-valve gain and $K_c = K'_c + C_l$ is the total flow pressure coefficient.

Additionally, in the case of a non-linear physical specimen, for both models in Fig. 4.1 or Fig. 4.2, the physical specimen block can be replaced by a non-linear model, representing a non-linear equation of motion:

$$m\ddot{x} + c\dot{x} + r = f_p \tag{4.14}$$

where r is the non-linear restitutive force of the physical specimen.

4.2 Actuator-specimen interaction

To show the behavior of a servo-hydraulic actuator connected to a physical specimen, the relation between commanded and measured signals is studied in this section.

Combining all the elements of the servo-hydraulic model, a transfer function from the commanded displacement u, to the measured displacement x can be obtained:

$$G_{xu}(s) = \frac{N_0}{D_4 s^4 + D_3 s^3 + D_2 s^2 + D_1 s + D_0} \tag{4.15}$$

where each coefficient is defined as:

$$N_0 = K_{prop}\frac{K_q A}{K_c} \tag{4.16}$$

$$D_0 = k + K_{prop}\frac{K_q A}{K_c} \tag{4.17}$$

$$D_1 = c + \frac{V}{4\beta K_c} + \frac{A^2}{K_c}k + k\tau \tag{4.18}$$

$$D_2 = m + \frac{V}{4\beta K_c}c + \frac{A^2}{K_c}\tau + c\tau + \frac{V}{4\beta K_c}k\tau \tag{4.19}$$

$$D_3 = \frac{V}{4\beta K_c}m + m\tau + \frac{V}{4\beta K_c}c\tau \tag{4.20}$$

$$D_4 = \frac{V}{4\beta K_c}m\tau \tag{4.21}$$

Obviously, the control plant transfer function is directly affected by the transfer system parameters, but the goal in this section is to show the influence of the attached physical specimen on the dynamic response of the control plant. Notice that the structural properties of the physical specimen directly affect the coefficients of the transfer function G_{xu}. Now, as an example, the servo-hydraulic model in equations (4.15) to (4.21) is evaluated with the parameters available in (Carrion and Spencer, 2007) and listed in table 4.1.

Table 4.1: Servo-hydraulic actuator and physical specimen model parameters (Carrion and Spencer, 2007).

Parameter	Value	Units	Description
K_p	118.11	mA/m	Proportional gain
τ	0.00332	sec	Servo-valve time constant
K_q	$3.77 \cdot 10^{-4}$	$m^3/sec/mA$	Total servo-valve gain
K_c	$4.63 \cdot 10^{-14}$	$m^3/sec/Pa$	Total flow pressure coefficient
A	$4.84 \cdot 10^{-4}$	m^2	Piston area
V	$7.97 \cdot 10^{-4}$	m^3	Fluid volume on actuator chambers
β	$6.62 \cdot 10^{8}$	Pa	Fluid bulk modulus
m	4.03	$Nsec^2/m$	Specimen and piston mass
c	1665	$Nsec/m$	Specimen and piston damping coefficient
k	$4.10 \cdot 10^{4}$	N/m	Specimen stiffness

The bode plots of the control plant transfer function G_{xu} with different stiffness values (multiples of the stiffness k in table 4.1) are presented in Fig. 4.3. These bode plots present the typical form of the transfer system, where the magnitude is close to zero for low frequencies and decays to negative values at high frequencies, showing the less capability of a transfer system to operate at high frequencies with

accuracy. Notice that, the curves with stiffness k and $0.5k$ do not show notorious differences in terms of magnitude, but for $5k$ and $10k$ the magnitude decays at lower frequencies.

In the case of time delays, it should be noted that delay is frequency-dependent. Although it is possible to approximate the delay as a constant value for low frequencies, this assumption can lead to poor delay compensation. Additionally, it can be seen that a stiffer specimen produces a higher delay. Or in contrast, if a specimen suffers a considerable stiffness degradation, the time delays will change during a test. This phenomenon depends on the capability of the transfer system, for this example, if the stiffness decays from k to $0.5k$ the transfer system does not suffer much change, but if decays from $10k$ to $5k$, the delay at low frequencies change considerably.

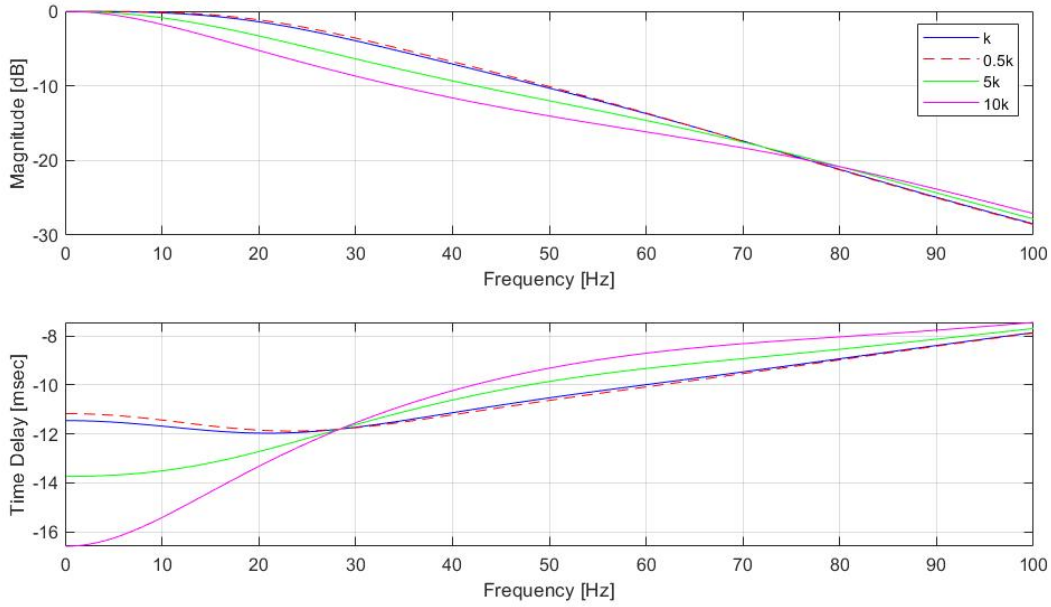

Figure 4.3: Servo-hydraulic actuator connected with specimens with different stiffness.

The interaction between the physical specimen and the transfer system is a crucial issue in RTHS. In general, every time a physical specimen is changed, a new compensator must be designed for the new control plant dynamics. Furthermore, if the physical specimen suffers structural modifications during the test, such as stiffness degradation, crack propagation or hardening effects, the control plant dynamics may change during the test, and the compensator performance can be affected.

5 Stability analysis in RTHS

Two aspects are crucial for the stability in RTHS: (i) problems in numerical integration, and (ii) the time delay in the hybrid loop. There is a vast literature about integration methods and their stability analysis, thus, this issue can be studied off-line once the numerical substructure is defined. Meanwhile, the instability due to time delay, has been attracted special attention for the RTHS community, since is a complex topic that involves numerical and physical components interacting in a closed-loop.

The stability of a hybrid system has been studied from different angles. In this chapter, the stability analysis approaches are classified into three groups: (i) the predictive stability indicators, which are focused on the partitioning between numerical and experimental components; (ii) the complete stability analysis where the dynamics of the actuator and compensator is included in the analysis, and (iii) the on-line stability analysis, where the analysis is executed with information obtained during the test.

5.1 Predictive stability indicators

Some authors have been studied the effect of delay for different partitioning choices, demonstrating that some configurations are more susceptible to instability than others. Wallace et al. studied the analytical delay differential equations of a subtructured system with constant delay (Wallace et al., 2005a) showing stable/unstable regions for different stiffness ratios between numerical and experimental components. Maghareh et al. proposed the predictive stability indicator for multiple degrees of freedom systems (Maghareh et al., 2017). Alternatively, Gao et al proposed other equations to analyze MDOF systems with delay (Gao and You, 2019). To summarize, this kind of analysis have the same goal: find the critical delay that causes instability for a particular partitioning choice.

As an example of how the partitioning affects the stability in RTHS, an alternative method to estimate the critical delay is implemented herein. The procedure consists of obtaining a transfer function for the numerical and experimental substructure, and approximate the actuator delay with a linear transfer function, then a transfer function for the closed-loop system is obtained. The block diagram is presented in Fig. 5.1. The numerical substructure generates the target displacement x_t from the earthquake $\ddot{u}_g$ and the experimental force f as inputs. Then, the target displacement is delayed by the transfer function G_τ. Finally, the experimental substructure produces the experimental force f which is sent back to the numerical substructure.

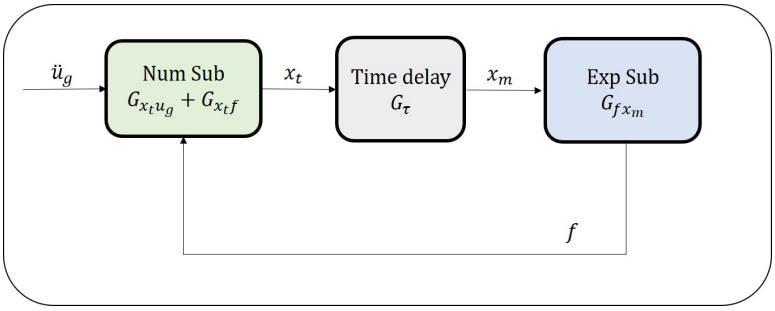

Figure 5.1: RTHS substructuring presented by transfers functions.

Consider the following SDOF system:

$$m\ddot{x} + c\dot{x} + kx = -(m_n + m_e)\ddot{u}_g \tag{5.1}$$

where the m, c and k are the mass, damping, and stiffness of the reference structure (complete structure). Each term is divided into numerical and experimental components:

$$(m_n + m_e)\ddot{x} + (c_n + c_e)\dot{x} + (k_n + k_e)x = -m\ddot{u}_g \tag{5.2}$$

where the m_n, c_n and k_e are the mass, damping and stiffness of the numerical substructure, while m_e, c_e and k_e are the mass, damping and stiffness of the experimental substructure, and $\ddot{u}_g$ is the ground acceleration. The numerical substructure output is the target displacement:

$$x_t = G_{x_t u_g}\ddot{u}_g + G_{x_t f} f \tag{5.3}$$

where the $G_{x_t u_g}$ is the transfer function from the ground acceleration to the target displacement, and $G_{x_t f}$, from the experimental force to the target displacement. Each transfer function corresponds to:

$$G_{x_t u_g} = \frac{-m}{m_n s^2 + c_n s + k_n} \tag{5.4}$$

$$G_{x_t f} = \frac{-1}{m_n s^2 + c_n s + k_n} \tag{5.5}$$

The actuator delay is represented with the Padé approximation, which generates a linear transfer function with a magnitude close to zero and a phase with approximately constant time delay. As an example, a 5 msec time delay can be represented by a second-order Padé approximation:

$$x_m = G_\tau x_t = \frac{s^2 - 1200s + 480000}{s^2 + 1200s + 480000} x_t \tag{5.6}$$

where x_m is the delayed target displacement, i.e. the "measured" displacement in the experimental substructure. Then, the experimental force is obtained by:

$$f = G_{f x_m} x_m = (m_e s^2 + c_e s + k_e) x_m \tag{5.7}$$

Finally, a total transfer function for the closed-loop system is calculated with the ground acceleration as input, and the target displacement as output:

$$x_t = G_{CL}\ddot{u}_g \tag{5.8}$$

$$G_{CL} = \frac{G_{x_t u_g}}{1 - G_{x_t f} G_{f x_m} G_\tau} \tag{5.9}$$

The stability of the closed-loop system can be analyzed by observing the poles of the transfer function G_{CL}. If the poles have a negative real part, the system stable for the considered time delay,

or in contrast, if there are one or more poles with a positive real part, the system is unstable. An unstable system implies that even for a bounded ground acceleration, the target displacements will grow up without limit.

As an example, consider a SDOF system with $m = 100$ kg, natural frequency $f_n = 2$ Hz, and damping $d = \frac{c}{2w_n m} = 3\%$. The partitioning consists in $m_e = 0.1m$, $c_e = 0.4c$, and $k_e = 0.4k$. The critical delay for a particular partitioning can be found obtaining the minimum delay that results in a pole with a positive real part. In this case, the critical delay is $\tau_{cr} = 16$ msec.

The pole-zero map for two different delay values $\tau_1 = 5$ msec and $\tau_2 = 18$ msec, is presented in Fig. 5.2, where it can be seen that the case with $\tau_1 = 5$ msec is stable, while the case with $\tau_1 = 18$ msec is unstable. This asseveration can be corroborated obtaining the impulse response of the closed-loop for each time delay. The impulse response are presented in Fig. 5.3, where evidently, the case with $\tau_2 = 18$ msec presents an unbounded response.

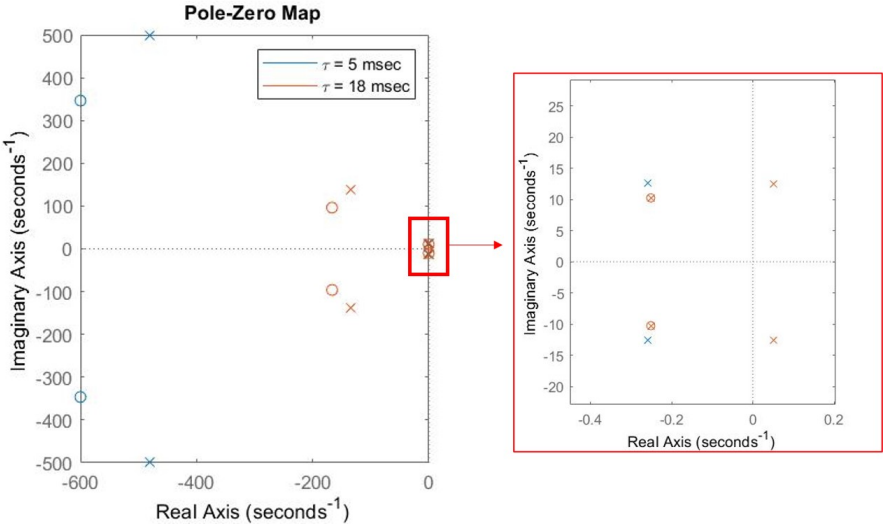

Figure 5.2: Pole-zero map for a particular partitioning and different time delay.

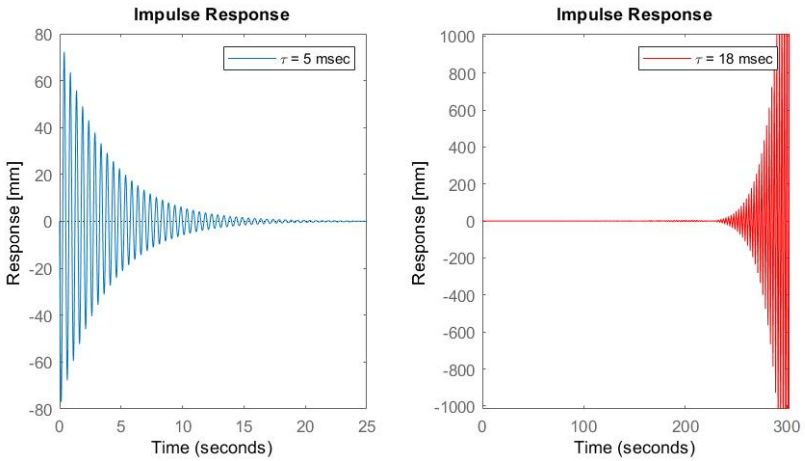

Figure 5.3: Impulse response for a particular partitioning and different time delay.

As another example, consider two SDOF systems: (i) system S_1 with $m = 500$ kg, natural frequency $f_n = 5$ Hz, and damping ratio $d = 3\%$. And (ii) system S_2, with $m = 500$ kg, natural frequency $f_n = 5$ Hz, and damping $d = 6\%$. The partitioning for each system consists in $m_e = 0.2m$, $c_e = 0.2c$. The critical delay for different experimental stiffness ratios is presented in Fig. 5.4. Critical delays are searched between 0 and 100 msec. Some observations about this graph:

- For small stiffness ratios for each case, there is no critical delay in the interest range, i.e. these partitions are not sensitive, and even without compensation does not show a risk of instability. However, for these cases, the actuator delay may not produce instability, but it can produce precision problems.
- At higher stiffness ratio the critical delay decrease. This occurs because the experimental force has more influence on the complete system.
- The system S_2 allows more delay than the system S_1. In general, higher damping implies more stable systems. Nevertheless, excess of added damping to avoid instability may cause unreliable results.

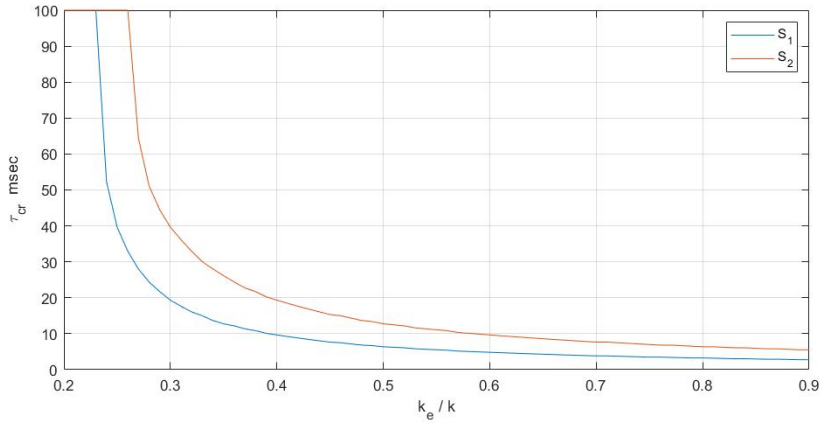

Figure 5.4: Critical delay for different experimental stiffness ratios.

This kind of stability analysis can be useful to evaluate the feasibility of different partitionings at the moment of design an RTHS test. It can be useful to avoid extremely sensitive cases.

5.2 Complete stability analysis

Instead of approximating the actuator dynamics as a pure time delay, another alternative is to represent it with a transfer function. This transfer function can be obtained experimentally for the actuator connected with the experimental substructure. Extensive stability analysis for an SDOF hybrid system was presented by Chen et al. (Chen and Chen, 2020), where a model of the transfer system and the physical specimen was considered. The presented robust stability analysis includes two kinds of uncertainties in the control plant model: (i) parametric uncertainties in the identified model, and (ii), unstructured uncertainties to cover unmodeled dynamics. Then, the stability of the system is examined through the Nyquist stability criterion. The closed-loop is analyzed through its open-loop transfer function by applying Cauchy's principle of argument. The hybrid system is robustly stable if and only if the envelope of the Nyquist plot does not include the point (-1,0).

Additionally, the dynamics of a linear compensation method can be included in this analysis. Chen et al. determined the stability margins for different partitionings and various compensation methods. The results are shown in Fig. 5.5, where solid lines correspond to the margins without considering uncertainties, meanwhile dashed lines includes uncertainties. Red curves do not consider compensation, blue curves correspond to the linear acceleration extrapolation method, gray curves to first-order inverse compensation method, and black curves to second-order phase-lead compensators.

In general, higher natural frequencies admit lower stiffness ratios, and the uncompensated cases are the most restrictive in terms of feasible partitionings. Furthermore, an interesting observation is how the stability margin decrease when uncertainty is included in the analysis.

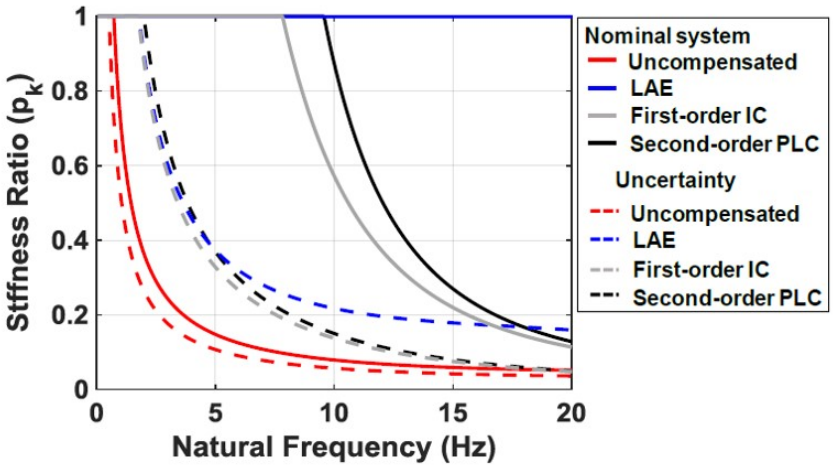

Figure 5.5: Stability margins for different partitionings and compensation methods (Chen and Chen, 2020).

This kind of stability analysis can be useful before a test when the experimental substructure is defined and a model of the control plant is available, even better if the uncertainty in the control plant model can be quantified.

5.3 On-line stability analysis

Some studies are available in the literature where online indicators are proposed for RTHS tests. Guo el at. (Guo et al., 2014) proposed the Frequency Evaluation Index (FEI) to evaluate the tracking performance of an actuator in the frequency domain, obtaining a representative amplitude and delay error for the test. Besides, FEI can be implemented online using a moving window to apply the Fast Fourier Transform (FFT) (Xu et al., 2019b). Although FEI could be used to measure synchronization errors quantitatively, it does not measure the effect of this delay on the hybrid system's stability. Meanwhile, Ahmadizadeh et al. (Ahmadizadeh and Mosqueda, 2009) proposed the Energy Error Indicator (EEI), which can be implemented online to measure the accumulated errors in RTHS. Although experimental errors can trigger instability, the EEI measures the experimental error, but do not recognize unstable cases directly.

5.3.1 Proposed stability indicator

A stability analysis is conducted through an energy balance in the equation of motion of the numerical substructure (Gálmez and Fermandois, 2020). The goal is to detect if the numerical response is growing up abnormally due to the addition of energy produced by a delayed experimental force.

Consider the EOM of the numerical substructure:

$$M_n\ddot{x}_n(t) + C_n\dot{x}_n(t) + K_n x_n(t) = -(M_n + M_e)\Upsilon\ddot{u}_g(t) - F_e(t) \tag{5.10}$$

where $x_n(t)$, $\dot{x}_n(t)$ and $\ddot{x}_n(t)$ corresponds to the displacement, velocity and acceleration of the numerical substructure, all relative to the ground motion. M_n, C_n and K_n corresponds to the numerical mass, damping, and stiffness matrices, respectively. Meanwhile, M_e is the experimental mass, and F_e corresponds to the feedback forces from the experimental substructure described as:

$$F_e(t) = M_e\ddot{x}_e(t) + C_e\dot{x}_e(t) + K_e x_e(t) \tag{5.11}$$

where $x_e(t)$, $\dot{x}_e(t)$ and $\ddot{x}_e(t)$ corresponds to the experimental displacement, velocity and acceleration of the experimental substructure at the physical-numerical interface, and in the ideal case, the actuators imposes $x_e = x_n$. However, in an RTHS test, the experimental displacements are not necessarily equal to the numerical displacements.

Assuming that an appropriate numerical integration method is implemented so that the calculated numerical substructure response is numerically stable, the equation of motion of the numerical substructure can be expressed as an energy balance, allowing to focus the stability analysis on the interaction between hybrid substructures due to experimental errors. If numerical substructure matrices M_n, C_n, K_n are symmetric; the energy balance can be obtained by taking the inner product with an infinitesimal numerical displacement trajectory, dx_n, and then integrating both sides of Eq. (5.10) over the displacement trajectory (in relative coordinates to the ground):

$$\int \ddot{x}_n^T M_n dx_n + \int \dot{x}_n^T C_n dx_n + \int x_n^T K_n dx_n = \int -\ddot{u}_g \Upsilon^T (M_n + M_e) dx_n + \int -F_e^T dx_n \tag{5.12}$$

Eq. (5.12) can be later expressed as a scalar equation as:

$$E_k + E_d + E_s = W_I + W_F \tag{5.13}$$

where E_k, E_d and E_s are the kinetic, dissipated and strain energy of numerical substructure, respectively, and calculated as:

$$E_k = \int \ddot{x}_n^T M_n dx_n; \quad E_d = \int \dot{x}_n^T C_n dx_n; \quad E_s = \int x_n^T K_n dx_n \tag{5.14}$$

meanwhile, W_I is the work done by the earthquake forces (namely as input work), and W_F is the work done by the experimental forces (namely as feedback work):

$$W_I = \int -\ddot{u}_g \Gamma^T M_r dx_n; \quad W_F = \int -F_e^T dx_n \tag{5.15}$$

It is worth mentioning that the energy balance from Eq. (5.13) must be fulfilled during a test even if the experimental force is delayed, and the hybrid system is unstable. In this sense, the feedback force is just another external excitation supplied over the numerical substructure.

When a hybrid system becomes unstable, the mechanical energy of both substructures will grow exponentially even if the earthquake signal goes zero. This issue could happen if the experimental

substructure introduces additional energy to the numerical substructure. It is desirable to detect this problem before the mechanical energy grows up at levels that can damage the experimental equipment.

During an RTHS test, it is normal that the mechanical energy of the numerical substructure increases, because the earthquake equivalent forces introduce energy to the system, but the mechanical energy should not be greater than the input work. Reordering Eq. 5.13 and grouping E_k and E_s in mechanical energy E_{mec}, Eq. 5.16 is obtained:

$$W_I - E_{mec} = E_d - W_F \tag{5.16}$$

If the feedback work, W_F, gets bigger than the dissipated energy E_d, the right side of Eq. (5.16) becomes negative. Due to the energy balance, the left side also becomes negative and indicates that mechanical energy gets bigger than the input energy. Thus, when the hybrid system's inherent dissipated energy is insufficient to counteract the added energy from the feedback force, the system will become unstable.

Therefore, the proposed analysis consists of comparing the feedback work with the dissipated energy through an indicator described in Eq. (5.17):

$$SW = \frac{W_F}{E_d + C_{SW}} H(W_F) \cdot 100\% \tag{5.17}$$

where SW is called the *Stability Warning Indicator*, and $H(\cdot)$ is the Heaviside function used to compute SW only when W_F is positive. Notice that the dissipated energy is always strictly positive (i.e., $E_d > 0$); hence, $E_d - W_F$ could be negative only if W_F is positive. Meanwhile, C_{SW} is a constant chosen to prevent large values of SW when the test starts (i.e., when E_d is close to zero). Notice that $E_d = 0$ at $t = 0$ (i.e., before the earthquake starts), so C_{SW} should be a constant selected that is big enough to make the denominator to be non-zero in the SW and to prevent large values of SW if W_F is dominated by noise in the force measurements. Moreover, C_{SW} should be small enough, so the SW denominator would be dominated by the E_d term during and after the earthquake. As a recommendation, both conditions could be satisfied if C_{SW} is selected as two magnitude orders below the maximum input work over the structural system. It is worth mentioning that this input work can not be calculated before the test since the complete hybrid system's response is unknown. However, an offline estimation of the input work magnitude order is enough to select a proper C_{SW}.

The explanation of the SW values is provided herein. When $SW = 0\%$, due to negative values of W_F, there is no risk of instability because the experimental substructure is removing energy from the numerical substructure. Next, if $0\% < SW < 100\%$, the experimental substructure is adding energy; but, the damping of the numerical substructure is enough to counter this effect. Finally, if $SW \geq 100\%$, then the numerical substructure's mechanical energy overcomes the input work, causing instability.

The main difference between the EEI indicator from Ahmadizadeh and the proposed SW is that the former evaluates simulation accuracy when affected by synchronization errors, and the latter is focused on assessing the stability of the hybrid system. For example, if a hybrid system presents a significant delay in the transfer system, the experimental errors will cause the experimental substructure to add energy to the numerical substructure. Nevertheless, if the numerical substructure has enough damping to maintain the system stable, the SW will be less than 100%; meanwhile, EEI will show large values due to the synchronization errors produced by the delay.

To compute the Stability Warning Indicator (SW) it is necessary to evaluate different energy terms using numerical integration. To calculate the accumulated energy $E[j]$ of a force $P[i]$ over a displacement increment $\Delta x[i]$, $\forall i \in [1, j]$, a trapezoidal rule is formulated:

$$E[j] = \sum_{i=1}^{j} \frac{1}{2} \left(P[i] + P[i-1]\right) \left(x[i] - x[i-1]\right) \tag{5.18}$$

This integration method is implemented in Simulink, as shown in the block diagram of Fig. 5.6, where Discrete Finite Impulse Response (FIR) Filters and Product blocks are employed to obtain the area of each trapezoid, and a Discrete-time Integrator block is required to obtain the accumulation over time. In the case of W_F the input force is $P = f_e$ and the input displacement is $x = x_n^{(1)}$ (scalar signals); meanwhile, to evaluate E_d, the input forces are $P = C_n \dot{x}_n$ and the displacements are $x = x_n$ (vector signals).

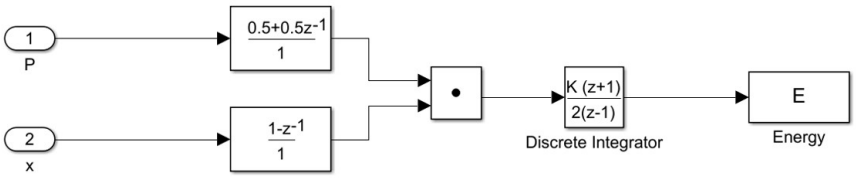

Figure 5.6: Block diagram for energy calculation.

The proposed stability indicator is implemented in numerical examples with linear systems in Section 7.4. It should be mentioned that the proposed methodology is valid only for linear numerical substructures because for non-linear systems there are other sources of energy dissipation, such as hysteresis or friction. Furthermore, a non-linear dynamic system could have multiple equilibrium points, thus the stability analysis becomes more complex.

6 Adaptive compensation

6.1 Adaptive model-based compensation methodology

The adaptive model-based compensation (AMB) architecture is presented in Fig. 6.1, where the displacement to be imposed is named herein as target displacement x_t. A feedforward control that depends on a set of parameters A takes the target displacement to generate the command signal x_c for the control plant. Consequently, the control plant achieves a measured displacement x_m, and the goal is to minimize the synchronization error $e = x_m - x_t \to 0$. Besides, the signals x_c and x_m are taken for the adaptation process of the control parameters A.

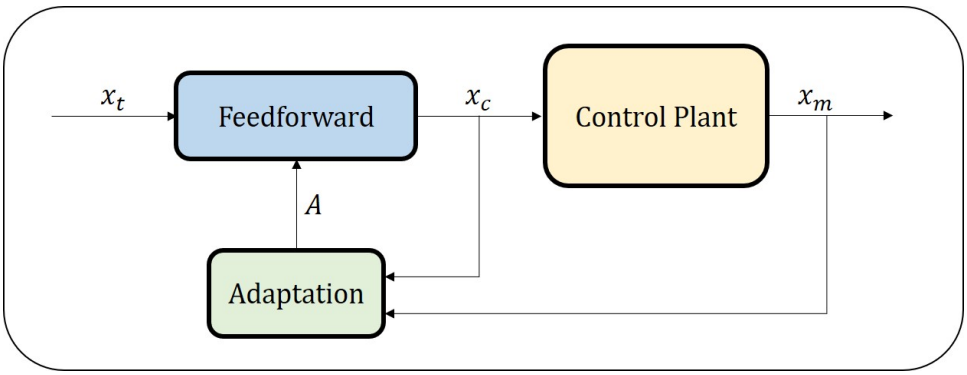

Figure 6.1: Control architecture of the proposed methodology.

The dynamic compensation method presented in this chapter is based on the adaptive model-based method presented by Chen et al. (Chen et al., 2015) with the modifications presented by Fermandois and Galmez (Fermandois et al., 2020).

The control plant can be approximated in the frequency domain by a third order transfer function without zeros $G_p(s)$:

$$x_m = G_p(s)x_c = \left(\frac{1}{a_3 s^3 + a_2 s^2 + a_1 s + a_0}\right) x_c \tag{6.1}$$

where a_i with $i = 0, 1, 2, 3$ are the coefficients of the control plant's transfer function $G_p(s)$; s is the Laplace variable, and x_m is the measured displacement. The coefficient a_0 is known as the DC gain of the transfer function, and it is generally close to 1. It means that at very low commanded frequencies, the measured signal takes $x_m \approx x_c$ at least in terms of amplitude. The parameter a_1 is closely related to the time delay at low frequencies. Finally, a_2, and a_3, affects the system dynamics mainly at higher frequencies.

To compensate for the control plant dynamics, the inverse of $G_p(s)$ is taken to generate the command signal from the target displacement:

$$x_c = G_p^{-1}(s)x_t = (a_3 s^3 + a_2 s^2 + a_1 s + a_0)x_t \tag{6.2}$$

where $G_p^{-1}(s)$ is the inverse feedforward controller, and x_t is the target displacement from the numerical substructure. Notice that the transfer function presented in Eq. (6.2) is improper; however, the controller can be implemented using a backward difference approximation:

$$\begin{bmatrix} x[i] \\ \dot{x}[i] \\ \ddot{x}[i] \\ \dddot{x}[i] \end{bmatrix} = \begin{bmatrix} 1 & 0 & 0 & 0 \\ 1/\Delta t & -1/\Delta t & 0 & 0 \\ 1/\Delta t^2 & -2/\Delta t^2 & 1/\Delta t^2 & 0 \\ 1/\Delta t^3 & -3/\Delta t^3 & 3/\Delta t^3 & -1/\Delta t^3 \end{bmatrix} \begin{bmatrix} x[i] \\ x[i-1] \\ x[i-2] \\ x[i-3] \end{bmatrix} \tag{6.3}$$

where Δt is the sampling period of the simulation and $x[i]$ is a displacement at time step i.Nevertheless, other finite difference rules can be used. Finally, the command signal for the actuator can be obtained from

$$x_c = [a_0 \; a_1 \; a_2 \; a_3][x_t \; \dot{x}_t \; \ddot{x}_t \; \dddot{x}_t]^T \tag{6.4}$$

Notice that the control signal is generated with an inverse feedforward controller with the estimated control plant parameters. Although in the AMB, the controller is formulated from the frequency domain, the implementation in the time domain in Eq. (6.4) is equivalent to the feedforward control presented in Adaptive Time Series (ATS) (Chae et al., 2013) and Conditional Adaptive Time Series (CATS) (Palacio-Betancur and Gutierrez Soto, 2019). The difference between the AMB, the ATS, and CATS is mainly the algorithm chosen to update the control parameters. In the AMB, the parameters are updated with an adaptive gradient law. In contrast, the ATS updates its parameters with the standard least square method considering a moving window of measured and commanded data. In contrast, the CATS parameters are updated with the recursive least square method. These methods can reach similar performance, but it also depends on several carefully chosen design parameters to provide effective adaptation. Furthermore, both CATS and ATS are presented in the literature for first and second-order compensators, and there is no evidence of its performance for higher-order models.

In the proposed AMB, the initial parameters for each a_i are obtained from an identified model of the transfer system without an experimental substructure. Then, these parameters are updated in real-time with the adaptive law presented in Chen et al. (2015). In the original AMB, the parameter a_0, known as DC gain, is taken equal to unity and is not subject to adaptation. But in this study is considered in the adaptation process since the experimental substructure properties can alter the DC gain of the control plant.

The adaptation process is presented as follows. The commanded signal x_c can be approximately estimated by reordering Eq. (6.1) in Eq. (6.5):

$$\hat{x}_c = [a_0 \; a_1 \; a_2 \; a_3][x_m \; \dot{x}_m \; \ddot{x}_m \; \dddot{x}_m]^T \tag{6.5}$$

where $\hat{x}_c$ is the estimated command signal and x_m is the measured displacement. The derivatives of x_m are obtained by two steps, first, x_m is filtered with a Butterworth filter to remove high-frequency noise: then, the time derivatives are calculated with Eq. (6.3). It should be mentioned that in the original AMB, a low-pass filter $\Lambda = 1/(1+s)^3$ is used to make proper transfer functions to obtain the derivatives of x_m. This low-pass filter affects the amplitude of the measured signal deteriorating the adaptation process, reason why that filter is changed to a Butterworth filter, just like in other methods such as

Adaptive Time Series (Chae et al., 2013) and Conditional Adaptive Time Series (Palacio-Betancur and Gutierrez Soto, 2019).

With Eq. (6.5) and the command signal x_c an indirect estimation error of the parameters a_i can be obtained:

$$e = \frac{x_c - \hat{x}_c}{m_s^2} \tag{6.6}$$

where e is the parameter estimation error, x_c is the command signal filtered with the same Butterworth filter to synchronize with the filtered measured signal x_m; $\hat{x}_c$ is the approximated command signal obtained with Eq. (6.5) with the estimated parameters a_i, and m_s^2 is a normalizing signal used to bound e, and taken as $m_s^2 = 1 + (X_m^T X_m)$ with $X_m = [x_m \ \dot{x}_m \ \ddot{x}_m \ \dddot{x}_m]^T$. Then, to update the parameters a_i, a cost function is formulated:

$$J(A) = \frac{e^2 m_s^2}{2} \tag{6.7}$$

where J is the cost function and $A = [a_0 \ a_1 \ a_2 \ a_3]$. Finally, the gradient adaptive law is implemented to update the parameters a_i:

$$\dot{A} = \Gamma e X_m \tag{6.8}$$

where $\dot{A} = [\dot{a}_0 \ \dot{a}_1 \ \dot{a}_2 \ \dot{a}_3]$ contains the rate of change of the parameters a_i, Γ is a diagonal adaptive gain matrix associated with the adaptation rate of parameters a_i, and $X_m = [x_m \ \dot{x}_m \ \ddot{x}_m \ \dddot{x}_m]^T$ are the higher-order time derivatives of the measured signal.

The implementation of the AMB compensator is summarized in the flow chart of Fig. 6.2.

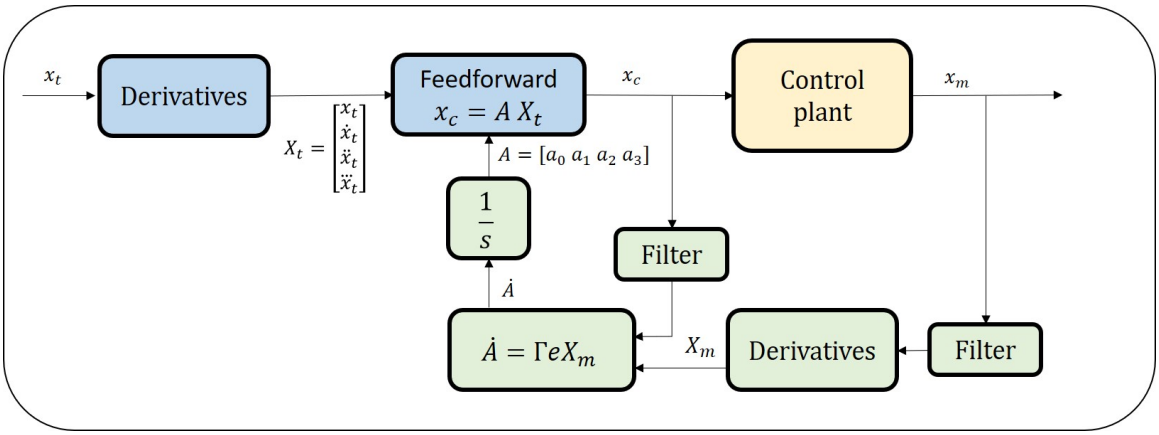

Figure 6.2: Flow chart of Adaptive model based compensator (AMB).

Additionally, it should be mentioned that the adaptive controller presented in this study can be augmented with a feedback control such as LQG control in the original adaptive model-based (Chen et al., 2015), or PI control in work of Ning et al. (Ning et al., 2020a). However, this study did not

consider feedback control for two reasons. First, to demonstrate the efficiency and robustness of the adaptive model-based compensation by itself. It is worth mentioning that a feedforward controller has more authority to compensate for delay errors than feedback controllers. The second reason is that a conventional feedback controller's design requires an accurate model of the control plant, including the experimental substructure. Notice that adequate feedback control can improve the compensation, but a bad design can result in instability of the close-loop of the controller-plant system.

6.2 Design and calibration process

The compensator must be designed to provide excellent delay compensation and quick adaptation, so special attention is given to the selection of initial conditions and adaptive gains. The initial conditions can be selected according to the actuator dynamics, but the selection of the adaptive gains could be a challenging task. Small adaptive gains produce slow adaptation, which can result in uncompensated delay during a part of the test. On the other hand, high adaptive gains can result in instability of the adaptive law, especially in the presence of noise or disturbances Ioannou and Sun (2012). Therefore, it is necessary to adjust the adaptive gains carefully to achieve both robustness and performance.

The design and calibration process is schematized in Fig. 6.3. The first step is to obtain a model of the transfer system without specimen interaction in the form of Eq. (6.1). Then, a feedforward controller is designed taking the inverse of the initial model. Next, the adaptive gains Γ are calibrated through an iterative process. The adaptive gains calibration requires numerical simulations with the following components:

1. A set of target displacements x_t. This data can be obtained from approximated reference structures subjected to earthquakes of interest to emulate in RTHS. Notice that the excitation is extremely uncertain in earthquake engineering, but it is considered to be known for structural performance assessment.

2. A controller based on an initial model, with initial parameters A_{init}.

3. A low-pass filter with a cut-off frequency according to the frequencies of interest and the capacity of the transfer system.

4. Different virtual control plants will be tested in RTHS. These virtual control plants need to be different from the identified model for the transfer system without a physical specimen. Consequently, the controller requires adaptation to reach an acceptable tracking of the virtual plant response x_m.

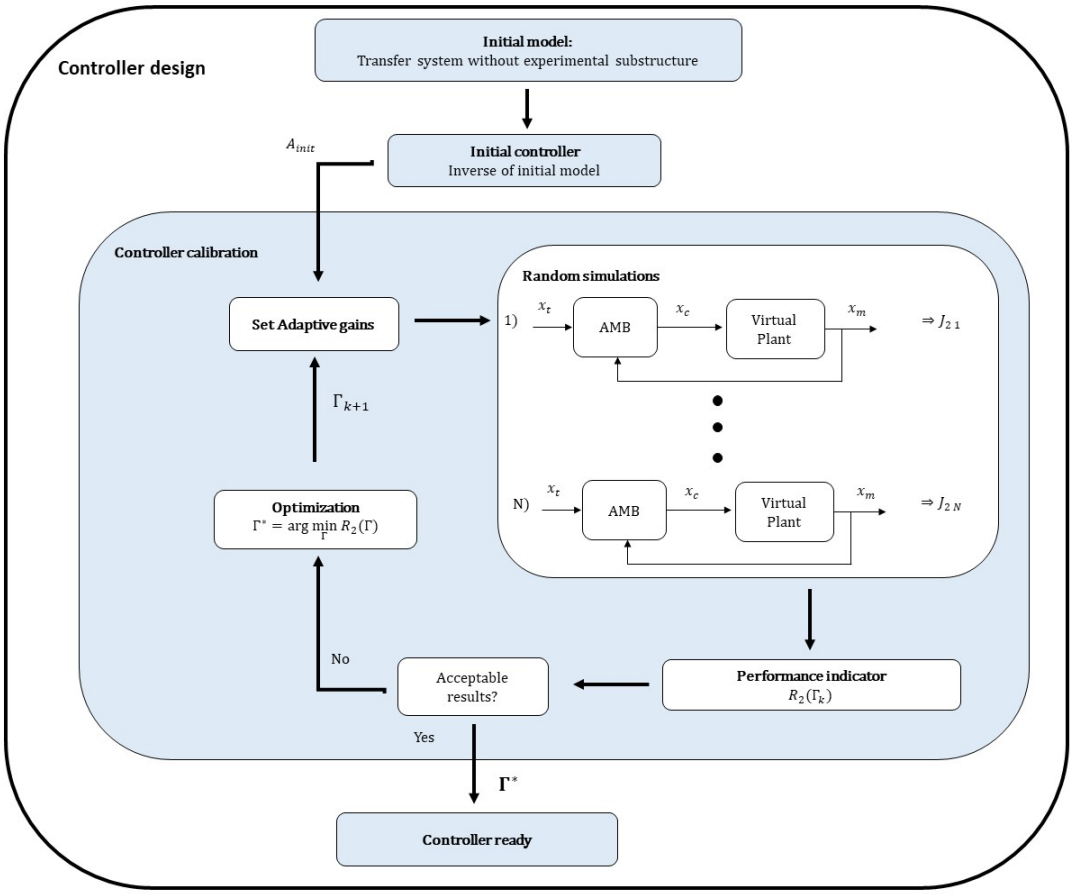

Figure 6.3: Adaptive model based design and calibration process.

At each iteration of the optimization process, a specific set of adaptive gains Γ_k are defined, where index k corresponds to the k-th iteration. A finite number of random simulations N are carried out with different target displacements, and a performance indicator J_{2n} is computed, where index n is the n-th simulation.

$$J_{2n}(\Gamma_k) = \frac{\mathbb{E}\left[(x_{tn} - x_{mn})^2\right]}{\mathbb{E}\left[x_{tn}^2\right]} \tag{6.9}$$

where $\mathbb{E}[\cdot]$ is the expectation operator. Subsequently, the average for the N simulations corresponds to the objective function for the specific set of adaptive gains R_2.

$$R_2(\Gamma_k) = \frac{1}{N}\sum_{n=1}^{N} J_{2n}(\Gamma_k) \tag{6.10}$$

Then, through the optimization algorithm, new adaptive gains are defined to obtain a better performance indicator. This process is realized until the optimization algorithm converges to the optimal

gains Γ^*. Notice that the goal of the calibration process is to find adaptive gains Γ^* that ensures the adaptation capacity maintaining excellent tracking performance and not to find specific adaptive parameters a_i. Finally, once the gains are calibrated to adapts the AMB from the initial model to different virtual plants, the controller is ready for implementation in RTHS.

A detailed design example of the AMB is presented in Section 7.2, where several numerical simulations using Simulink are carried out with different random inputs to evaluate the performance for the adaptive gains. The optimization process is implemented with particle swarm optimization from Global Optimization Matlab toolbox.

7 Numerical application

7.1 The benchmark problem

The virtual RTHS benchmark problem from Silva et al. (Silva et al., 2020) is selected as a platform to evaluate the performance of the proposed compensation method and the on-line stability analysis. The reference structure consists of a three-story moment frame with three lateral degrees of freedom, as shown on the left side of Figure 7.1. The reference structure is divided into a numerical substructure and a linear SDOF experimental substructure, as shown on the right side of Figure 7.1. The equation of motion (EOM) of the reference structure is:

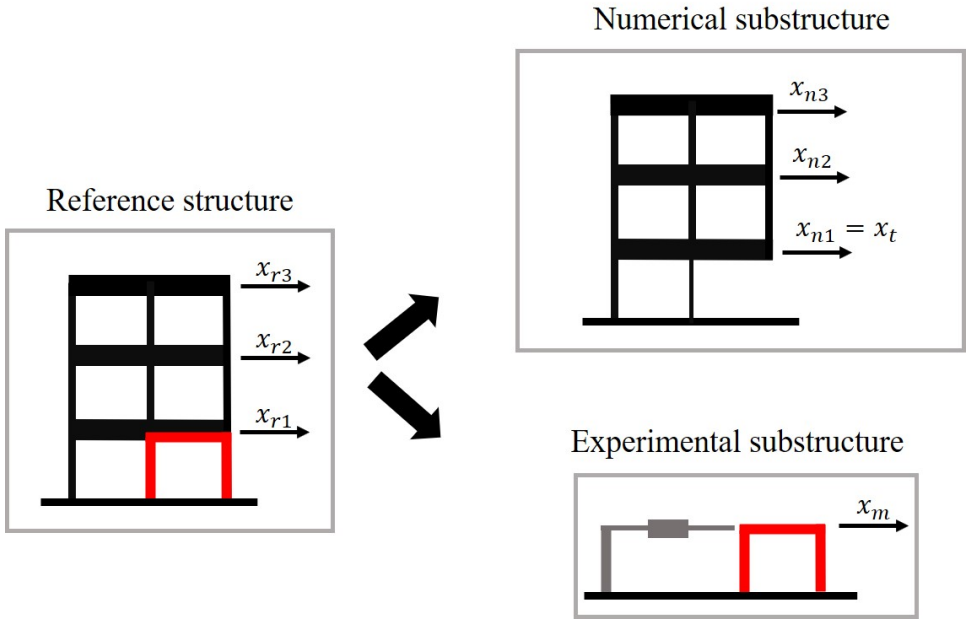

Figure 7.1: Reference structure and partitioning.

$$\begin{Bmatrix} \dot{x}_r \\ \ddot{x}_r \end{Bmatrix} = \begin{bmatrix} 0 & I \\ -M_r^{-1}K_r & -M_r^{-1}C_r \end{bmatrix} \begin{Bmatrix} x_r \\ \dot{x}_r \end{Bmatrix} + \begin{bmatrix} 0 \\ -\Upsilon \end{bmatrix} \{\ddot{u}_g\} \tag{7.1}$$

$$\{x_r\} = \begin{bmatrix} I & 0 \end{bmatrix} \begin{Bmatrix} x_r \\ \dot{x}_r \end{Bmatrix} + [0] \{\ddot{u}_g\} \tag{7.2}$$

where M_r, K_r, and C_r are the mass, stiffness and damping matrices, respectively. $x_r(t)$, $\dot{x}_r(t)$, and $\ddot{x}_r(t)$ are the displacement, velocity, and accelerations vectors, respectively, all measured relative to the ground motion. $\ddot{u}_g(t)$ is the ground acceleration, and $\Upsilon = [1\ 1\ 1]^T$ is the seismic influence vector.

Once the reference structure is separated, the EOM of the numerical substructure is reordered in Eqs. (7.3) and (7.4) where the inputs are the ground acceleration and experimental force and the outputs are the numerical displacements:

$$\begin{Bmatrix} \dot{x}_n \\ \ddot{x}_n \end{Bmatrix} = \begin{bmatrix} 0 & I \\ -M_n^{-1}K_n & -M_n^{-1}C_n \end{bmatrix} \begin{Bmatrix} x_n \\ \dot{x}_n \end{Bmatrix} + \begin{bmatrix} 0 & 0 \\ -M_n^{-1}M_r\Upsilon & -M_n^{-1}\gamma \end{bmatrix} \begin{Bmatrix} \ddot{u}_g \\ f_e \end{Bmatrix} \tag{7.3}$$

$$\{x_n\} = \begin{bmatrix} I & 0 \end{bmatrix} \begin{Bmatrix} x_n \\ \dot{x}_n \end{Bmatrix} + \begin{bmatrix} 0 & 0 \end{bmatrix} \begin{Bmatrix} \ddot{u}_g \\ f_e \end{Bmatrix} \tag{7.4}$$

where M_n, K_n, and C_n are the numerical mass, stiffness and damping matrices, respectively. $x_n(t)$, $\dot{x}_n(t)$ and $\ddot{x}_n(t)$ corresponds to the displacement, velocity and acceleration of the numerical substructure, all relative to the ground. Meanwhile, f_e corresponds to the feedback force from the experimental substructure acting with an influence vector $\gamma = [1\,0\,0]^T$. f_e for a linear experimental substructure is defined as:

$$f_e = k_e x_m + c_e \dot{x}_m + m_e \ddot{x}_m \tag{7.5}$$

where m_e, k_e and c_e are the mass, stiffness and damping of the experimental substructure. x_m, $\dot{x}_m$ and $\ddot{x}_m$ corresponds to the measured (experimental) displacement, velocity and acceleration imposed on the experimental substructure. For the compatibility in the interface between substructures, the response of the first degree of freedom of the numerical substructure x_{n1} is the target displacement x_t to be imposed on the experimental substructure. It means, in the ideal case $x_m = x_t = x_{n1}$.

The transfer system connected to the experimental substructure is modeled with transfer functions as shown in Fig. 7.2 where the parameters of the transfer functions are listed in Table 7.1. The parameters are represented with a truncated normal distribution with the specified mean (nominal) value and a standard deviation. Additionally, to get a more realistic representation of the virtual control plant, the measured signals force f_e and displacement x_m are contaminated with noise modeled as band-limited white noise to represent physical sensors.

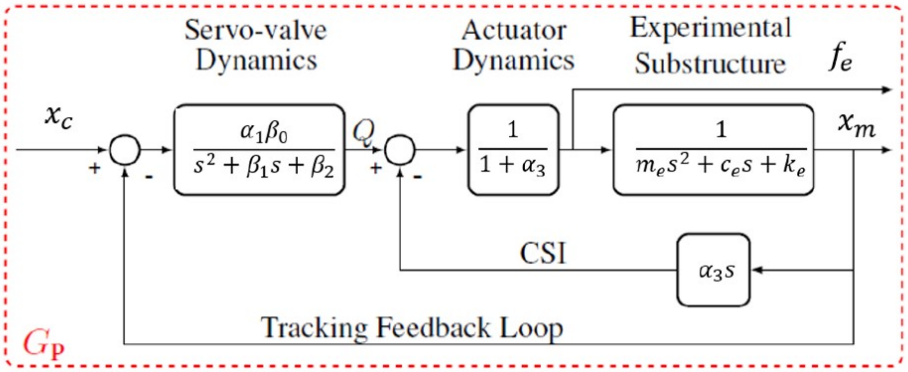

Figure 7.2: Block diagram of the control plant. Adapted from Silva et al. (Silva et al., 2020).

In the benchmark problem, four partitioning cases are defined with different reference structure properties but the same experimental substructure. In this study, two additional cases are defined to consider a wide spectrum of scenarios. The reference structures are listed in Table 7.2. Cases I to IV corresponds to the original benchmark partitioning cases. Cases V and VI consider random linear

Table 7.1: Control plant parameters.

Parameter	Nominal Value	Standard Deviation	Units
$\alpha_1\beta_0$	$2.13 \cdot 10^{13}$	–	m-Pa/sec
α_2	$4.23 \cdot 10^{6}$	–	m-Pa
α_3	3.3	1.3	1/sec
β_1	425	3.3	-
β_2	$1 \cdot 10^{5}$	$3.31 \cdot 10^{3}$	1/sec
m_e	29.1	–	kg
c_e	114.6	–	N sec/m
k_e	$1.19 \cdot 10^{6}$	$5 \cdot 10^{4}$	N/m

experimental substructures with properties uniformly distributed between the limits detailed in Table 7.3.

Table 7.2: Reference structure properties for each case.

Case	Mass/floor kg	Natural frequencies Hz	Damping by mode
I	1000	3.61; 16.00; 38.09	5%
II	1100	3.44; 15.25; 36.32	4%
III	1300	3.17; 14.03; 33.40	3%
IV	1000	3.61; 16.00; 38.09	3%
V	1400	3.05; 13.52; 32.30	5%
VI	900	3.81; 16.86; 40.15	4%

Table 7.3: Experimental substructure properties for cases V and VI.

Parameter	Minimum	Maximum	Units
m_e	10	40	kg
c_e	50	1000	N sec/m
k_e	$1 \cdot 10^{4}$	$2 \cdot 10^{6}$	N/m

The Simulink block diagram for the virtual RTHS is presented in Fig. 7.3.

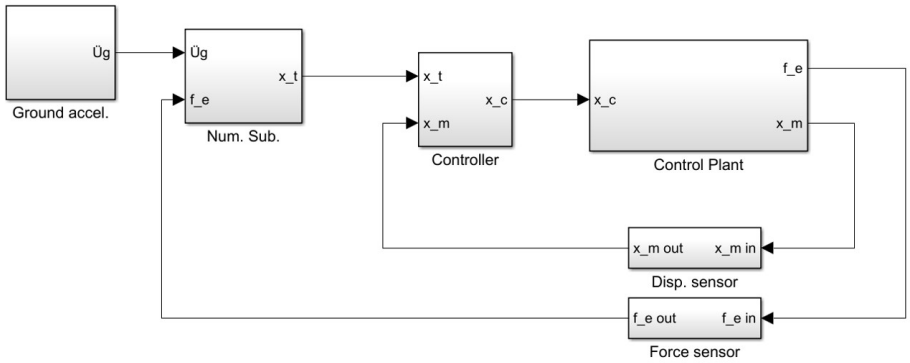

Figure 7.3: vRTHS Simulink block diagram.

7.2 Adaptive compensation design and calibration

7.2.1 Initial controller and calibration simulation

The AMB compensator requires a model of the transfer system (i.e., loading equipment) without any experimental substructure, namely as the initial model. In laboratory, this model can be obtained from system identification, but in this numerical example, the initial model is assumed from the control plant model in Fig. 7.2 evaluated with an experimental substructure with properties $m_e = 0$, $c_e = 0$ and $k_e = 1$ N/m. The initial model transfer function is presented in Eq. (7.6):

$$x_m = G_p^0(s)x_c = \left(\frac{1}{1.986 \cdot 10^{-7}s^3 + 8.440 \cdot 10^{-5}s^2 + 0.0199s + 1} \right) x_c \tag{7.6}$$

where $G_p^0(s)$ is the initial model transfer function and its bode diagram is presented in Fig. 7.4. The initial model can be compared with the benchmark problem control plant defined in Section 7.1 (with nominal parameters). Notice that the initial model presents a considerable time delay, especially for low frequencies (0 to 20 Hz). However, the inclusion of an experimental substructure increases, even more, the time delay and also affects the magnitude. It is expected that a controller designed for the initial model results in insufficient compensation for the different control plants, therefore, the controller must adapt its parameters to reach acceptable performance.

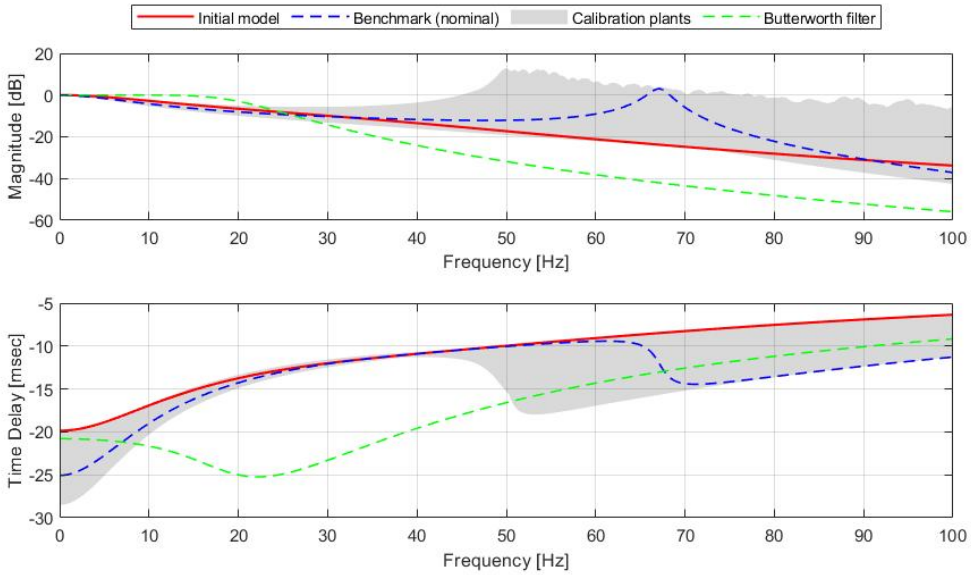

Figure 7.4: Control plant and butterworth filter Bode diagrams.

The initial feedforward controller is formulated taking the inverse of the initial model $G_p^0(s)$:

$$x_c = \begin{bmatrix} 1.0 & 1.99 \cdot 10^{-2} & 8.440 \cdot 10^{-5} & 1.986 \cdot 10^{-7} \end{bmatrix} \begin{bmatrix} x_t & \dot{x}_t & \ddot{x}_t & \dddot{x}_t \end{bmatrix}^T \tag{7.7}$$

For the noise filter design, three principal factors should be considered: (i) the frequency content of the earthquake, (ii) the frequency content of the structure response, which is affected by both substructures, and (iii) the frequency range of operation of the transfer system. For this study, the frequency range of interest is considered between 0 to 20 Hz. Although the third natural frequency of all cases is higher than 20 Hz, the structure response will be principally controlled by the first and second modes due to the excitation properties, additionally, the capability of transfer systems over 30 Hz is generally poor. Therefore the selected noise filter is a 4^{th} order Butterworth with a cut-off frequency of 20 Hz. The bode diagram of this filter is included in Fig. 7.4. This filter keeps an approximately unit gain for low frequencies but adds a time delay to the filtered signals. However, this time delay only affects the adaptation process and does not affect the compensation directly. For example, if the filter generates a delay of 22 msec, the control parameters a_i will suffer 22 msec of delay in its adaptation. However, the delay between the measured signal x_m and the target signal x_c will depend on the actual values a_i and the control plant behavior. If the control plant produces a delay of 26 msec at some frequency, and the initial controller compensates 19 msec at this frequency, therefore, the uncompensated delay between x_m and x_m will be 7 msec and this delay will decrease according to the controller adaptation. Thus, the filter's delay (22 msec) affects the adaptation and not the compensation directly.

Additionally, the adaptive parameters $A = \{a_i, i = 0, 1, 2, 3\}$, can be constrained by defining upper and lower bounds for each parameter. In this example, the parameters are constrained only to $a_i > 0$ because the resulting control plant transfer function for the model in Fig. 7.2 takes non-negative

coefficients. The adaptive parameters a_i also can be upper bounded according to the expected limits for a particular transfer system and the experimental substructures properties of interest, but in this study upper bounds are not considered to observe free adaptation.

For the calibration of adaptive gains, an optimization process is carried out using numerical simulations with the Simulink block diagram presented in Fig. 7.5. For each adaptive gain matrix, a predefined number of simulations are realized with different target displacements and different virtual control plants. At each simulation, the target displacement is generated using SDOF calibration structures subjected to a ground motion. In this calibration, the El Centro earthquake is selected with different scales. The earthquake scales and SDOF properties are modeled as uniform random variables with the specified bounds in Table 7.4.

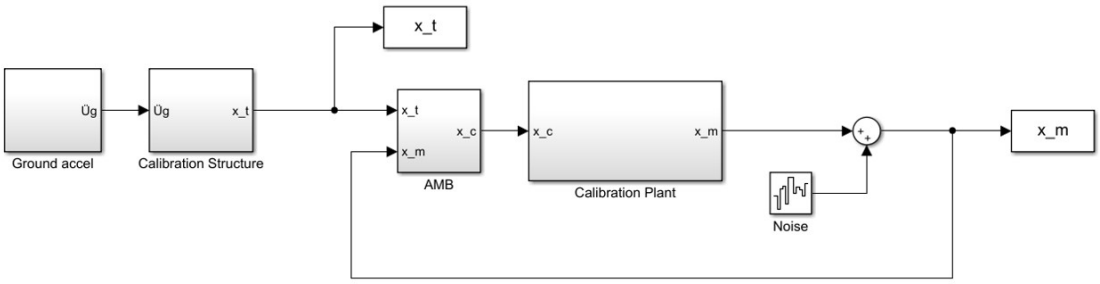

Figure 7.5: Block diagram for the calibration simulation.

Table 7.4: Earthquake scale respect to PGA and SDOF properties bounds for uniform distribution.

Parameter	Minimum	Maximum	Units
Scale	30	60	%
(Scaled PGA)	(0.089)	(0.179)	(g)
Natural frequency	2.8	4	Hz
Damping	3	5	%

On the other hand, the calibration plants do not need to be accurate models of the plants that will be tested in RTHS, it only needs to be an approximate model of the transfer system with interaction with different experimental substructures and must be different from the initial plant to ensure adaptation from the initial model to different models. In this example, the calibration plants are formulated with the transfer system model in Fig. 7.2 with the nominal parameters of Table 7.1 and experimental substructures with properties with uniform random distributions: $m_e \in [10, 40]$ kg, $c_e \in [50, 1000]$ Nsec/m and $k_e \in [1 \cdot 10^4, 2 \cdot 10^6]$ N/m (i.e.,ame distribution as in Table 7.3). The possible bode diagrams for the calibration plants are included in Fig. 7.4.

For each simulation the normalized root square mean error (NRMSE) between x_m and x_t is computed as an error indicator:

$$J_{2n}(x_t, x_m) = \sqrt{\frac{\sum_{l=1}^{L}(x_m[l] - x_t[l])^2}{\sum_{l=1}^{L}(x_t[l])^2}} \cdot 100\% \tag{7.8}$$

where J_{2n} represents the synchronization error of the n^{th} simulation, l is the discrete-time index, and L is the total length of data in each simulation.

For each set of adaptive gains $\Gamma_k = \text{diag}([\Gamma_0\ \Gamma_1\ \Gamma_2\ \Gamma_3])$, a total of $N = 100$ simulations are carried out to account for random earthquake scales, SDOF properties, and calibration plants. Then, the mean value of the J_2 indicators is computed as an error indicator for the specific set of the adaptive gains Γ_k:

$$R_2(\Gamma_k) = \frac{1}{N}\sum_{n=1}^{N} J_{2n}(\Gamma_k) \tag{7.9}$$

where J_{2n} corresponds to the error indicator for the simulation n.

As an example of the calibration simulation, two runs with different adaptive gains, but the same simulation parameters are realized. The ground motion corresponds to the El Centro earthquake scaled to 40% of PGA, the calibration structure is defined with 4% of damping and natural frequency of 3.5 Hz. The experimental substructure properties are: $m_e = 20$ kg, $c_e = 500$ Nsec/m, and $k_e = 1 \times 10^6$ N/m. The synchronization results are presented in Fig. 7.6, where the target and measured displacements, apparently match for both cases, but observing the error subgraph, evidently, the results with Γ_b are better than for Γ_a. Additionally, the adaptation of the control parameters a_i is presented in Fig. 7.7, where it can be seen that Γ_b produce fast adaptation for the most important parameters a_0 and a_1.

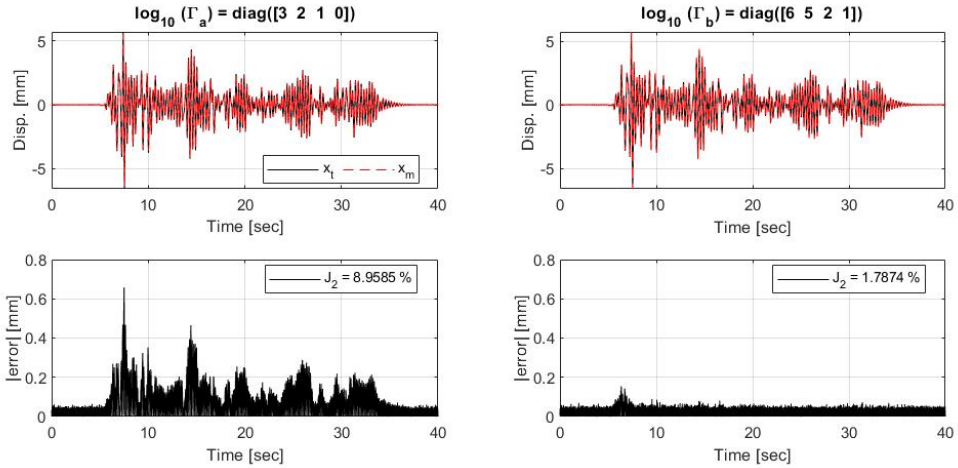

Figure 7.6: Displacement results of calibration simulation example with different adaptive gains and fixed simulation parameters.

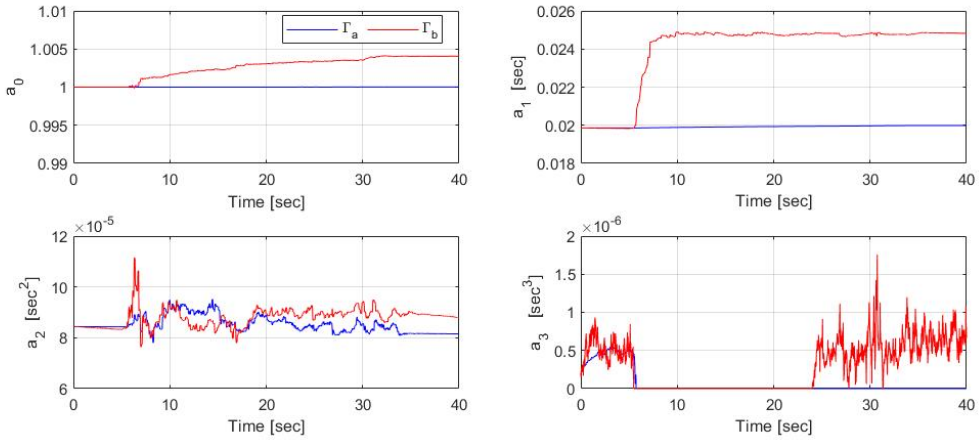

Figure 7.7: Adaptation results of calibration simulation example with different adaptive gains and fixed simulation parameters.

7.2.2 Sensitivity analysis

A sensitivity analysis is conducted in order to account for the effect of the random parameters in the calibration simulation. The first analyzed case is the non-adaptive case, i.e. $\Gamma = \text{diag}[0;0;0;0]$. The results of 100 simulations are shown in Fig. 7.8. The J_2 results are contained between 0.8% and 20% with mean value $R_2 = 8.7\%$ and standard deviation $\sigma R_2 = 4.6\%$. It can be easily observed that J_2 is highly dependant from on the experimental stiffness, while other parameters seem to not have much influence on J_2. This occurs because the controller without adaptation is capable to compensate the actuator dynamics when the experimental substructure does not produce much interaction. Since the experimental stiffness produces more control-structure interaction than the experimental mass or damping, it is possible to observe how the error J_2 increases with the stiffness. Additionally, if the compensator has no adaptation, it acts as a linear system, so the target displacement amplitude does not affect the compensator performance. The target displacement amplitudes are controlled by the earhquake and the dynamic properties of the calibration structure.

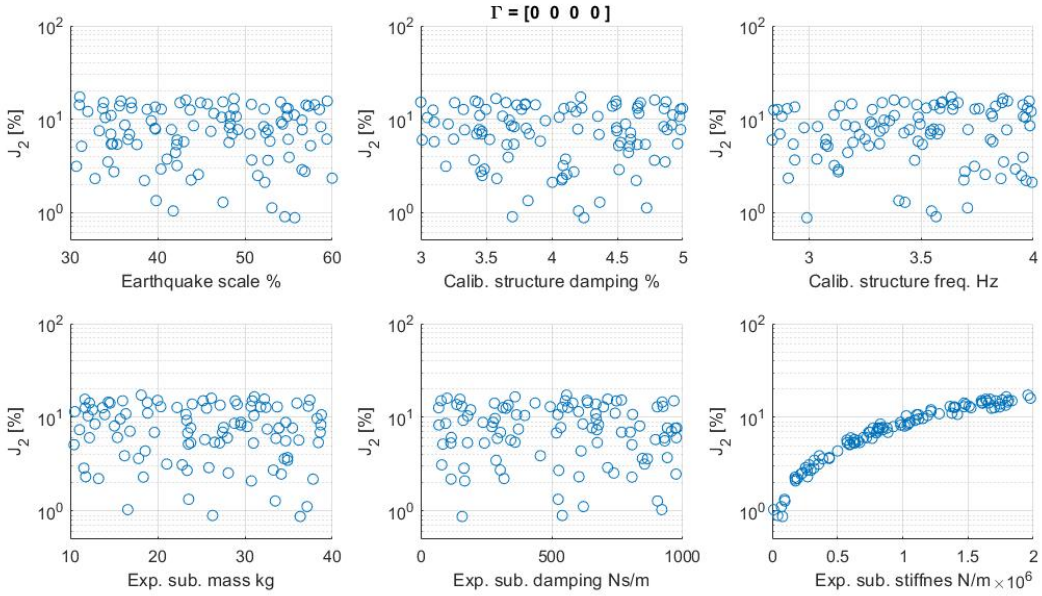

Figure 7.8: Realizations of the calibration simulation ($N = 100$) without adaptation.

The previous observations are valid for the non-adaptive case, but the adaptive case becomes non-linear and obviously depends on the selected adaptive gains Γ. In Fig. 7.9, the results of 400 realizations with "high gains" are presented. In this case, there are several simulations with extremely bad performance. The J_2 errors are between 0.7% and $4 \cdot 10^4$%, with mean $R_2 = 541\%$ and standard deviation $\sigma R_2 = 2800\%$. The simulations with $J_2 > 10\%$ are marked in magenta, notice that in this case, the experimental substructure stiffness has not an evident relationship with the observed errors. On the other hand, the magenta points are concentrated in low calibration structure's natural frequencies ($< 3.4Hz$), and high earthquake's scales ($> 50\%$). Clearly, the compensator performance depends on the target displacement characteristics. Since the parameter adaptation is proportional to the estimated error (Eq. (6.8)) and the adaptive gains, possibly, systems with higher amplitude or lower frequency responses, requires slower adaptation than higher frequency systems.

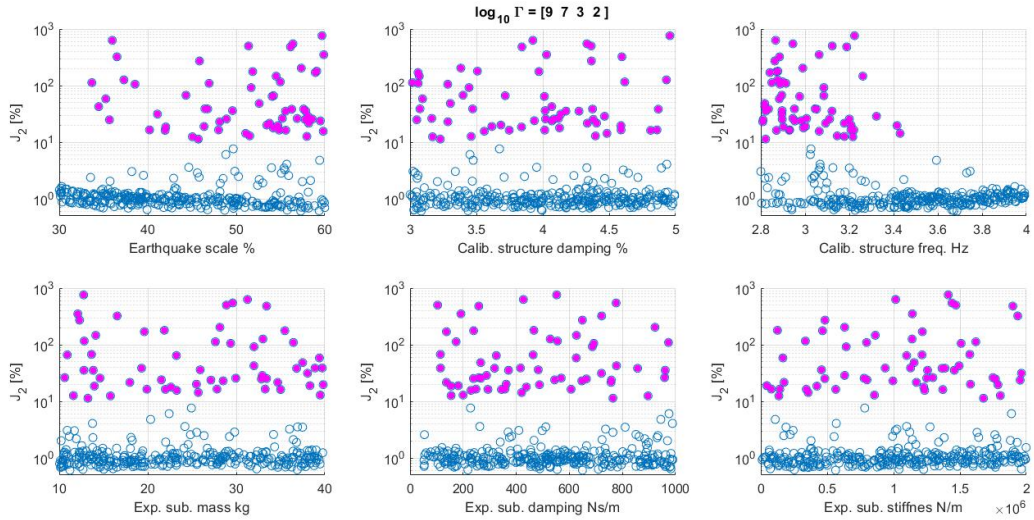

Figure 7.9: Realizations of the calibration simulation ($N = 400$) with high adaptive gains.

Finally, the goal is to find a set of adaptive gains that result in acceptable values of J_2 for every realization for the selected simulation parameters.

7.2.3 Adaptive gains optimization

An optimization algorithm is utilized to find the matrix Γ^* which minimizes the R_2 indicator. Since the objective function R_2 depends on four parameters of the adaptive gain matrix Γ it is difficult to visualize it. Furthermore, since the N simulations have random inputs, there is no analytical function to obtain $R_2(\Gamma)$ so it is very difficult to analyze the multi-variable search space for Γ. Consequently, an appropriate optimization method should be selected.

In this study, particle swarm optimization (Kennedy and Eberhart, 1995) from Global Optimization Toolbox from Matlab is utilized. A Matlab function is defined with a vector $\gamma = [\gamma_0, \gamma_1, \gamma_2, \gamma_3]$ as input. This vector γ is related to the adaptive gains Γ such that $\gamma_i = \log_{10}(\Gamma_i)$. The Matlab function runs the N simulations with the defined adaptive gains and outputs the error indicator R_2.

Particle swarm optimization consists of defining several particles (I particles), where the position of each particle represents a possible solution to minimize a fitness function. In this calibration, $p_i[h]$ represents the position $\gamma = [a, b, c, d]$ for the particle $i \in [1, I]$ at the iteration $h \in [1, H]$, where H is the total number of iterations. Thus, for each position, there is an error indicator $R_2(p_i[h])$ resulting from the 100 simulations with the adaptive gains associated with position $p_i[h]$. The optimization algorithm is described as follows. First, a set of I particles with random initial positions and velocities are defined in a constrained search space. Then, the position and velocity of each particle are updated, according to:

$$v_i[h+1] = \omega v_i[h] + r_1[h]c_1(pm_i[h] - p_i[h]) + r_2[h]c_2[h](g[k] - p_i[h]) \tag{7.10}$$

$$p_i[h+1] = p_i[h] + v_i[k+1] \tag{7.11}$$

where $v_i[h]$ is the velocity of particle i at iteration h. The velocity is updated according to a weighted sum of three components: (i) inertia with weight ω (ii) difference between the position with best result of the particle pm_i and the current position p_i, with a random component $r_1 \in [0, 1]$ and weight c_1, and (iii) the difference between the position with best result of the swarm g and the current position p_i, with a random component $r_2 \in [0, 1]$ and weight c_2. The best position of a particle pm_i corresponds to the position with the lowest R_2 value for the particle i. Whereas, the best position of the swarm g corresponds to the position with the lowest R_2 value for all particles.

So, the search space for the adaptive gains is investigated by trial and error to define a constrained but wide search space for the optimization. The constraints are selected as $\gamma_0 \in [2, 10]$; $\gamma_1 \in [0, 8]$; $\gamma_2 \in [-2, 6]$ and $\gamma_3 \in [-4, 4]$. The sum weights are defined as $\omega = c_1 = c_2 = 0.5$. The particle swarm function is utilized with a swarm size of 15 and maximum iterations of 10. This number of evaluations is considerably small for this kind of optimizer but in this case, is enough to find excellent results between the selected bounds.

After the optimization process, the best result is:

$$\Gamma^* = \text{diag}([10^{8.4}\ 10^{6.2}\ 10^{2.1}\ 10^{0.8}]) \tag{7.12}$$

where the resulting error for the calibration simulation is $R_2 = 0.85\%$.

To visualize the design space and the obtained optimal gains, a sensitivity analysis for the adaptive gains is performed. In this case, 200 random combinations of adaptive gains are created using Latin Hypercube Sampling (`lhsdesign()` in Matlab), which is a technique to generate multivariable samples efficiently. For each set of adaptive gains, the R_2 indicator is computed. The results are presented in Fig. 7.10, where the obtained optimum is marked in red. First, it should be noted that the optimal gains minimize the R_2 indicator. Second, the adaptive gain Γ_1 seems to be more significant than the other adaptive gains. Third, the worst results are obtained for the higher values of Γ_0, Γ_1, and Γ_2. And fourth, the results are not sensitive for Γ_3.

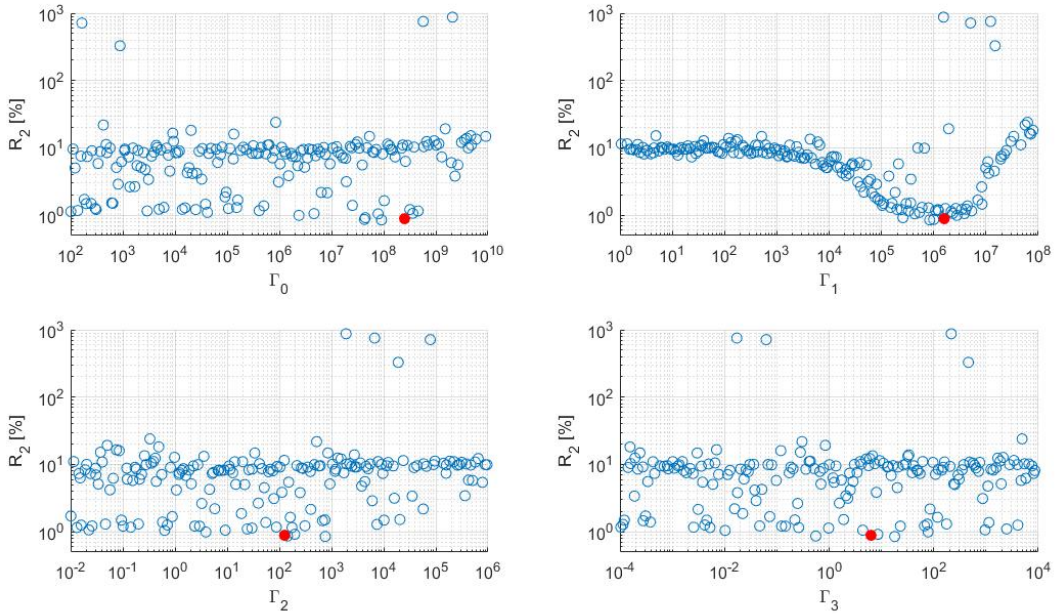

Figure 7.10: R_2 results for different random combinations of adaptive (Note: optimal gain is marked in red).

Since the results are very sensitive for Γ_1, a second sensitivity analysis is conducted with Γ_1 fixed at the optimum value. The results are shown in Fig. 7.11, where it can be seen that there are no good results for higher values of Γ_0 and Γ_2. The bad results for lower gains can be explained as follow. The yellow points correspond to results with $R_2 > 10\%$ and $\Gamma_0 > 10^9$, so the bad results for low values of Γ_2 and Γ_3 are due to infeasible Γ_0. The green points are results with $R_2 > 10\%$ and $\Gamma_2 > 3 \cdot 10^4$, so the bad results for low values of Γ_0 and Γ_3 are due to infeasible Γ_2. Then, the magenta points correspond to results with $R_2 > 10\%$ and $\Gamma_3 > 10^3$, demonstrating that extremely high values for Γ_3 also produce high errors. Finally, the black points correspond to $R_2 > 10\%$ with $\Gamma_0 > 10^9$ and $\Gamma_2 > 3 \cdot 10^4$, these are the worst results because two adaptive gains are too high. Notice that the obtained optimal gains avoid these infeasible zones for each adaptive gain.

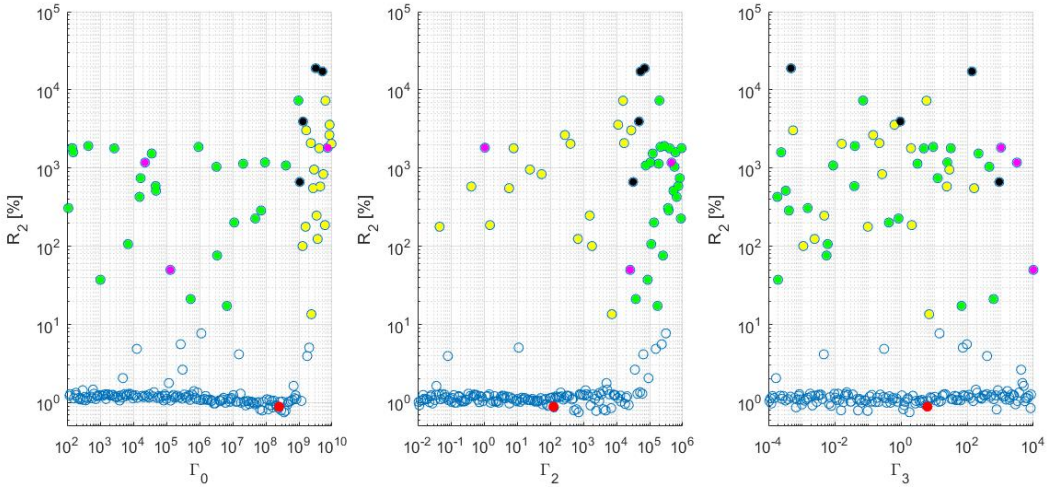

Figure 7.11: R_2 results for different random combinations of adaptive gains with fixed $\Gamma_1 = 10^{6.2}$ (Note: optimal gain is marked in red).

An alternative to analyze the obtained optimum is to explore the neighborhood of the solution. The process consists on fixing two terms of the adaptive gain matrix and generates a grid of adaptive gains for the remaining two terms. The results of the error indicator R_2 for different grids of adaptive gains are presented in Fig. 7.12. For example, the first sub-graph corresponds to different values for Γ_0 and Γ_1 with fixed optimum values for Γ_2 and Γ_3. It can be seen that the optimum is localized in a zone with small values of R_2 for every sub-graph, demonstrating that exists a wide zone of feasible results. For another part, extremely lower and higher gains result in higher values for R_2. The worst scenarios are obtained with extremely higher gains, due to overshooting in the adaptation process. Notice that this color map is obtained for the specified random inputs, so, if the compensator is implemented for different rabndom inputs, the optimum and the color map will change.

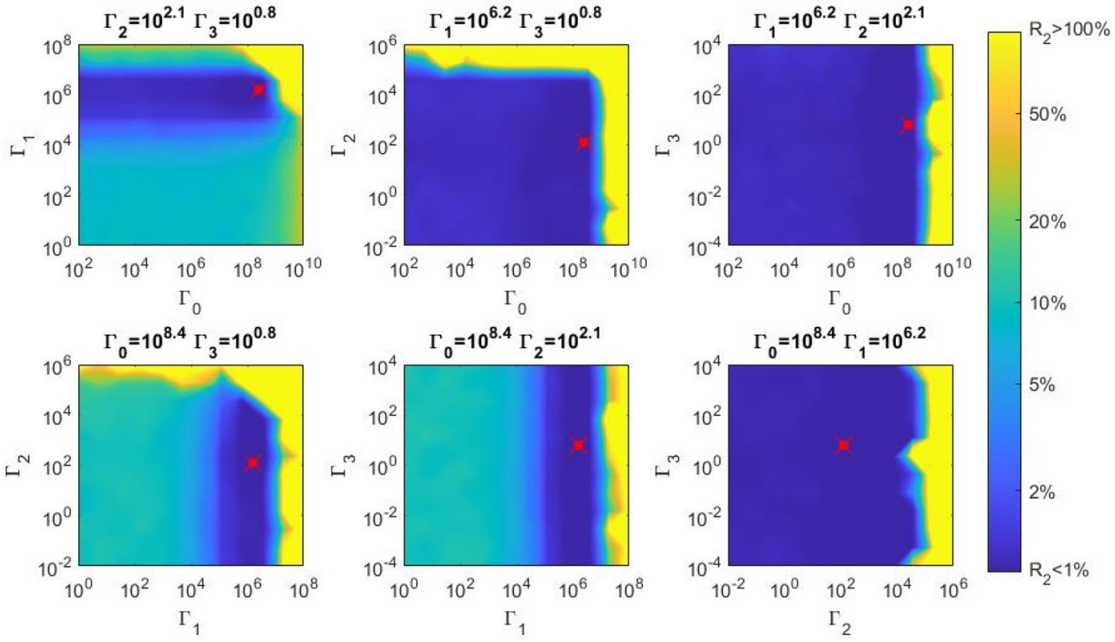

Figure 7.12: Error indicator R_2 for different adaptive gains around the optimum gain (marked in red).

An alternative design is to select lower gains than the obtained optimum, to increase the distance with the unfeasible (yellow) zone while maintaining reasonable R_2 performance. The distance from the unfeasible zone to the selected gains is associated with the degree of robustness. Further studies could take this property into account in the calibration process. However, in this study, the obtained gains Γ^* from the optimization are utilized for the controller in all the different vRTHS simulations in Section 7.3. However, the obtained optimum is considered without modifications for the performance evaluation of the compensator.

Finally, a sensitivity analysis for the random inputs is realized with the obtained optimum to show the robustness of the solution. The results of 200 simulations are presented in Fig. 7.13, where the results show small errors and very low dispersion. The results seem to be dependant on the earthquake scale and natural frequency, but this behavior has an explanation. The target displacement amplitude increase with the earthquake scale and decreases with the natural frequency. For another part, the synchronization error with good compensation is mainly composed by noise in measured displacement, therefore, the ratio between error and target signal increase if the target signal's amplitude decrease.

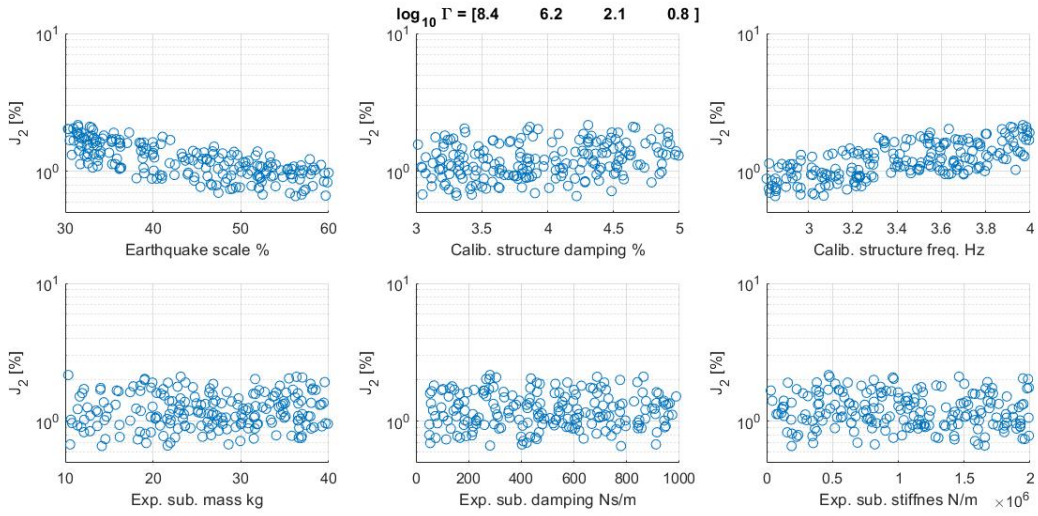

Figure 7.13: Realizations of the calibration simulation ($N = 200$) with the optimal adaptive gains.

7.3 Virtual RTHS results

Different simulations are carried out with the same compensator designed in Sections 7.2.1 and 7.2.3. The results are evaluated through the J_2 error indicator defined in Eq. (7.8), which measures the synchronization error between numerical and experimental displacements. Although the benchmark problem considers many other indicators, only the J_2 is considered in this study because a dynamic compensator aims to minimize this error. Furthermore, if the synchronization error in the numerical-physical boundary is minimized, the response of the hybrid system should be closest to the emulated system response.

7.3.1 Compensation and adaptation analysis

In this subsection, the results for a simulation for case I with nominal values are presented and analyzed. The structure is subjected to the El Centro 1940 earthquake scaled to 60% of the peak ground acceleration (PGA). The synchronization results are presented in Fig. 7.14, where an excellent tracking of displacements can be observed. The synchronization error is mainly composed of noise in the measured displacement and the J_2 indicator is under 2%. It should be mentioned that the noise filters only acts on the measured signal for the adaptation process and not for the simulation results. The results can be filtered on the post-processing of the obtained data.

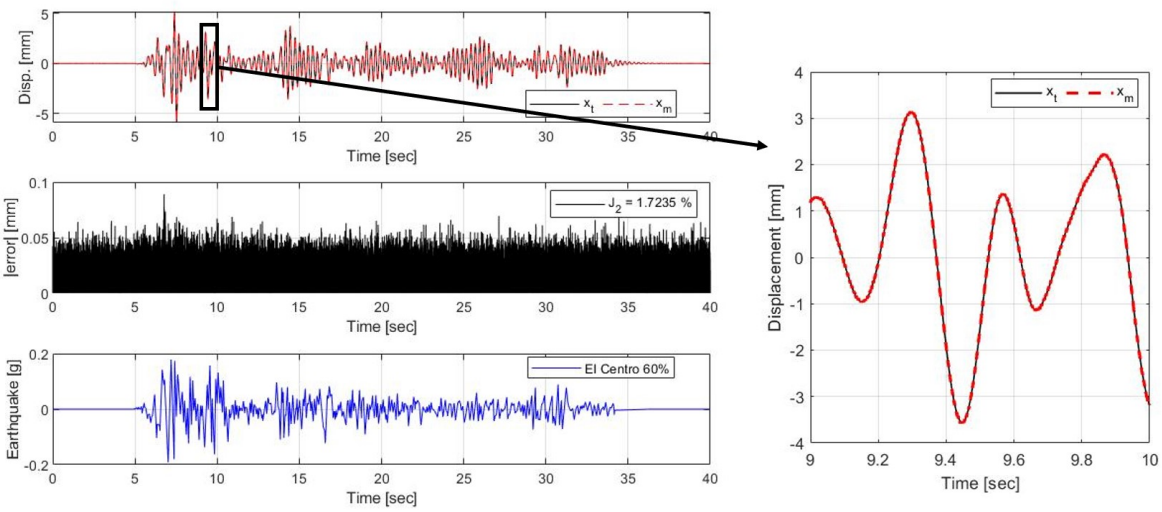

Figure 7.14: Synchronization results for Case I subjected to El Centro 50%.

The adaptation of control parameters a_i is presented in Fig. 7.15, where after 5 sec of simulation, at the beginning of the strong motion, the control parameters presents quick adaptation. After 7 sec, the adaptation seems noisy; thus, smoother adaptation is possible with lower adaptive gains. However, if the compensation results are excellent, the smoothness of the adaptation is not an issue.

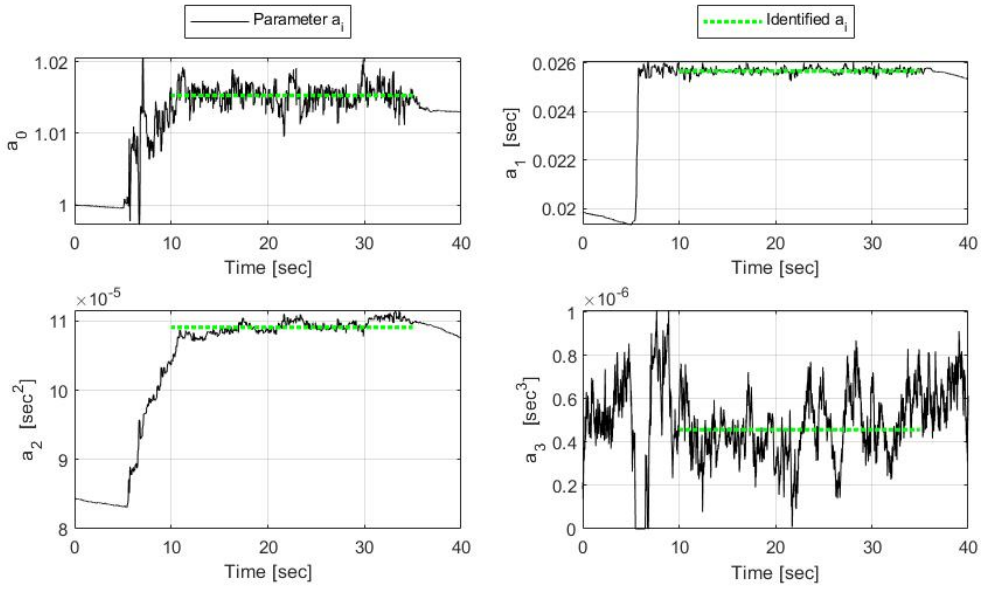

Figure 7.15: Control parameters adaptation results for Case I subjected to El Centro 50%.

Additionally, since the initial conditions of the compensator are based on the initial model, the adaptation process can be interpreted as an online identification problem. Although only the parameter a_1 shows an evident convergence, an identified value is computed for each a_i taking the mean value between 10 sec and 35 sec of simulation. With these identified values, an identified transfer function is calculated and compared with the initial model and the actual control plant in Fig. 7.16. The identified control plant match very well with the actual control plant for frequencies below the cut-off frequency of the Butterworth filter of the adaptation process (i.e. $f_c = 20$ Hz), which explains the good compensation. However, the identified transfer functions do not match for high frequencies for several reasons, first, the control plant results in a 5^{th} order transfer function, thus the 3^{th} order models can not capture the entire dynamics of the control plant. Additionally, the adaptation process information is mainly composed of low-frequency signals due to the excitation and structure properties and mainly due to the filtering process.

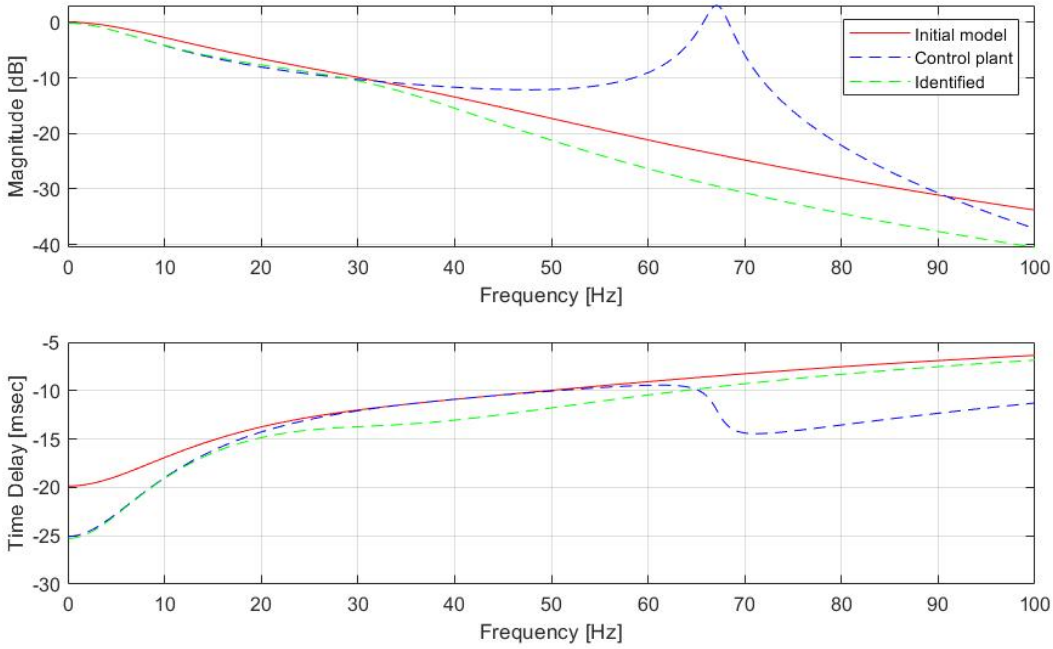

Figure 7.16: Adaptation in frequency domain.

7.3.2 Simulations with uncertainties and different experimental substructures

In this subsection, the results of several simulations with uncertainties in the control plant are presented. Three different earthquakes are selected: (i) El Centro 1940 earthquake (PGA 0.298g); (ii) Kobe 1995 earthquake (PGA = 0.578g); both included in the original benchmark problem, and additionally, (iii) Maule 2010 ($M_w = 8.8$ and PGA = 0.401g). The three unscaled acceleration records are presented in Fig. 7.17.

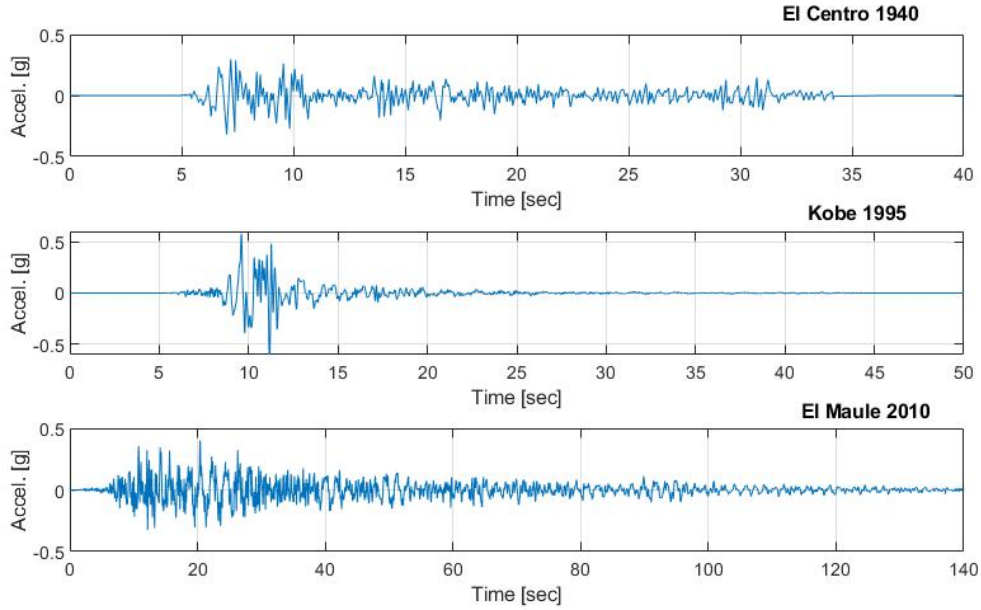

Figure 7.17: Acceleration records of considered earthquakes.

The six defined cases are subjected to each earthquake with 20 simulations per case to evaluate the robustness of the compensator. For the simulations, each earthquake was scaled to obtain responses according to the capacity of the benchmark transfer system. The Bode diagrams for the simulated control plants are presented in Fig. 7.18. The original benchmark control plant with uncertainties in experimental stiffness and transfer system parameters are presented on the left side. In contrast, the right side presents the different control plants simulated for cases V and VI. Notice that the additional cases V and VI cover a broad spectrum of scenarios, especially in terms of time delay at low frequencies.

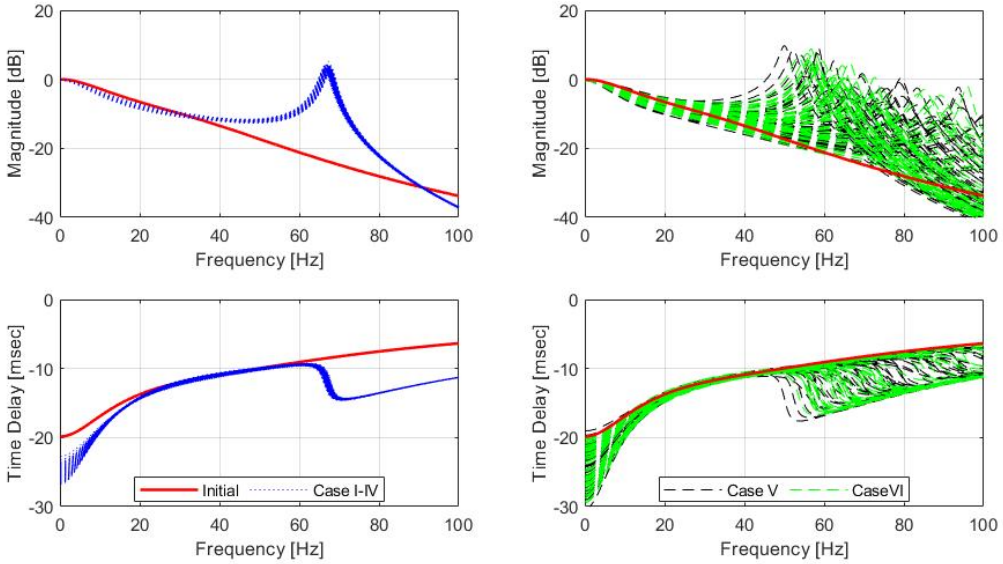

Figure 7.18: Bode diagrams of simulated control plants.

The synchronization results are presented in Fig. 7.19. The first observation is that all cases present a low J_2 error indicator, below 3%. Additionally, the variability for each case is extremely low, demonstrating that the compensator is robust under the uncertainties in the transfer system and experimental substructure. Also, J_2 mean values are computed for each case. These values are different between cases,and can be explained because all cases have the same displacement noise but different responses. Due to the excellent compensation, the synchronization error is mainly composed of noise.

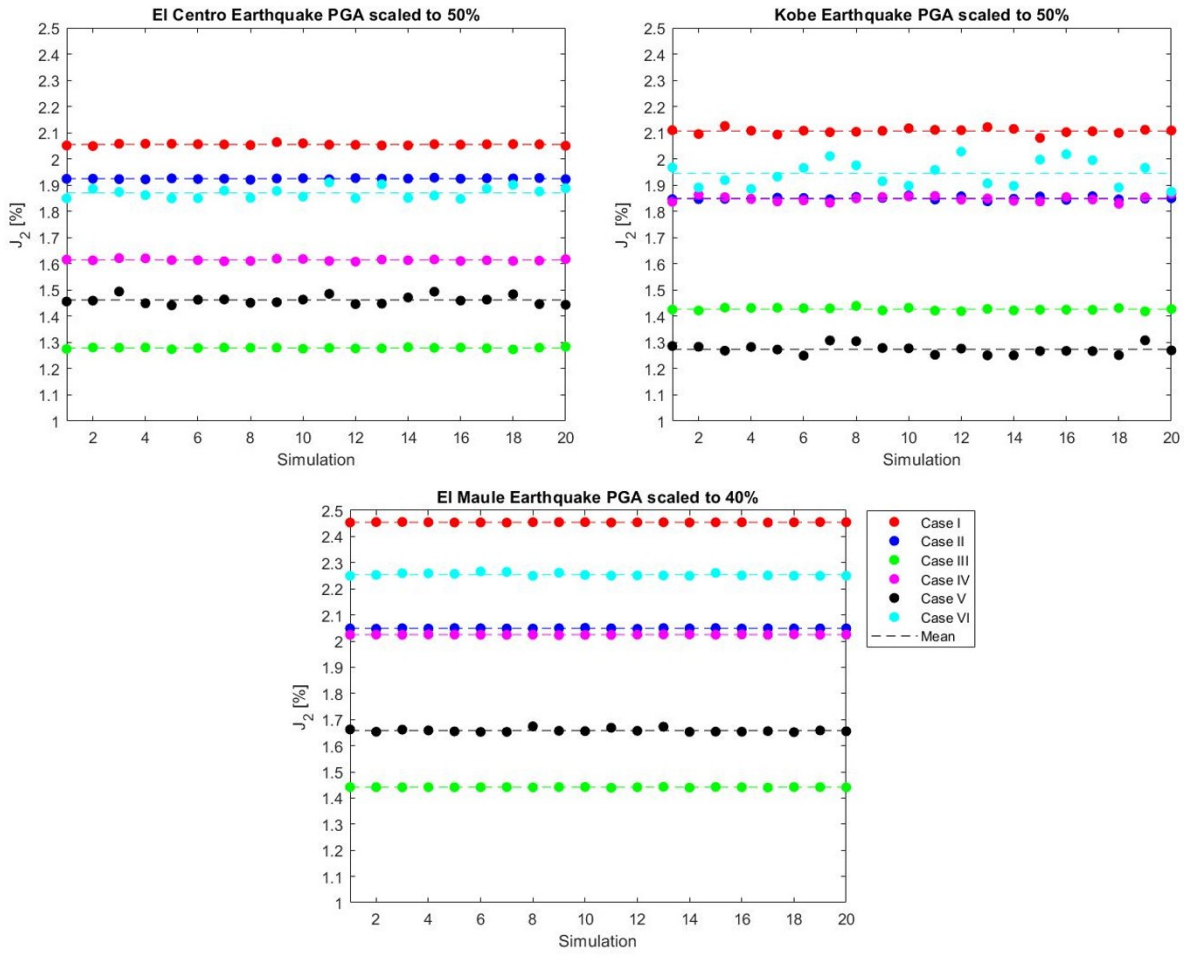

Figure 7.19: J_2 results for case study ($N = 20$).

7.3.3 Non-linear experimental substructures

In this subsection, experimental substructures with different non-linear behaviors are simulated with models presented in Sivaselvan and Reinhorn (2000). In this case, the block corresponding to the experimental substructure in the model of Fig. 7.2 must be replaced by a subsystem that includes the non-linear equations of the experimental substructure.

The non-linear models are based on the Bouc-Wen model with some modifications to include strength and stiffness variations.

The experimental force is calculated with the following expression:

$$f_e = r_e + c_e\dot{x}_m + m_e\ddot{x}_m \tag{7.13}$$

where r_e is a non-linear restitutive force described by the modified Bouc-Wen model:

$$\dot{r}_e = R_k k_e \left(1 - \left|\frac{r_e}{f_y}\right|^N (\eta_1 sign(r_e \dot{x}_m) + \eta_2)\right) \dot{x}_m \tag{7.14}$$

where R_k is a stiffness degradation factor, k_e is the initial elastic stiffness and f_y is the yield force. N, η_1, and η_2 are parameters that control the hysteresis shape. The stiffness degradation factor and the yield force degradation are calculated with the Mostaghel's degradation models (also presented in Sivaselvan and Reinhorn (2000)):

$$R_k = e^{-\alpha H} \tag{7.15}$$

$$f_y = f_{y0}(1 + \beta H)^{-1} \tag{7.16}$$

where α is a parameter that controls the stiffness degradation, β controls the strength degradation, and f_{y0} is the initial yield force. Finally, H is the dissipated hysteretic energy which can be calculated in incremental form as:

$$\Delta H = \left(\frac{r_e + (r_e + \Delta r_e)}{2}\right)\left(\Delta x_m - \frac{\Delta r_e}{R_k k_e}\right) \tag{7.17}$$

Additionally, to consider a hardening effect, a cubic spring is added in parallel with a constant cubic stiffness k_h:

$$f_e = k_h x_m^3 + r_e + c_e \dot{x}_m + m_e \ddot{x}_m \tag{7.18}$$

The reference structure and the initial experimental substructure properties correspond to Case I from the original benchmark problem. Four experimental substructures are defined with the parameters presented in Table 7.5.

Table 7.5: Parameters for non-linear models.

Non-linear Case	f_{y0} (N)	N	η_1	η_2	α	β	k_h N/m^3
A	2380	25	0.5	0.5	0	0	0
B	1904	1	0.6	0.4	0	0	6×10^9
C	2975	5	0.5	0.5	0	0.01	0
D	2678	2.5	0.5	0.5	0.02	0.005	0

Each case is subjected to the El Centro earthquake scaled to 60%. The relationship between measured force and measured displacements for each non-linear case is presented in Fig. 7.20. In these graphs, the measured force includes inertial, viscous, restitutive forces, and noise. The non-linear case A correspond to an almost bi-linear case; non-linear case B is a smooth hysteretic model with hardening; non -linear case C considers strength degradation; and non-linear case D considers both strength and stiffness degradation.

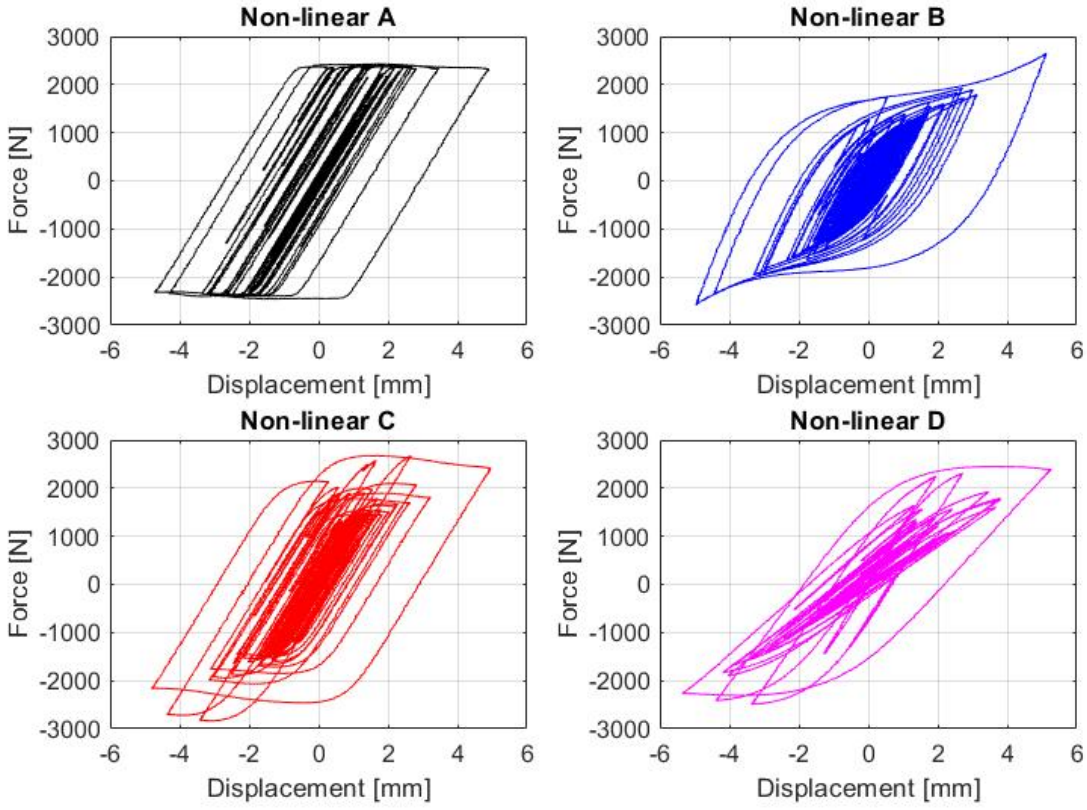

Figure 7.20: Force vs Displacement relation for different non-linear models.

The target and measured displacements of each simulation are presented in Figures 7.21 and 7.22. Additionally, the synchronization subspace plots (SSP) are presented in Fig. 7.23, where the almost 1:1 straight lines show the excellent delay compensation without considerable amplitude errors. In Figures 7.21 and 7.22, small errors can be observed and the J_2 indicator for every case is under 4% which demonstrates good compensation. Observing the synchronization error of each case, a part of the error can be attributed to the measurement noise, but in some instances, the error grows considerably. The biggest error of each case matches the maximum response, where the experimental substructure exhibits a highly non-linear response. While the maximum errors are acceptable, maybe it is possible to reduce these errors by combining the adaptive feedforward control with feedback control. On the other hand, this adaptive controller presents excellent behavior for the time-varying properties of non-linear case IVD, which presents notorious stiffness degradation in fig. 7.20.

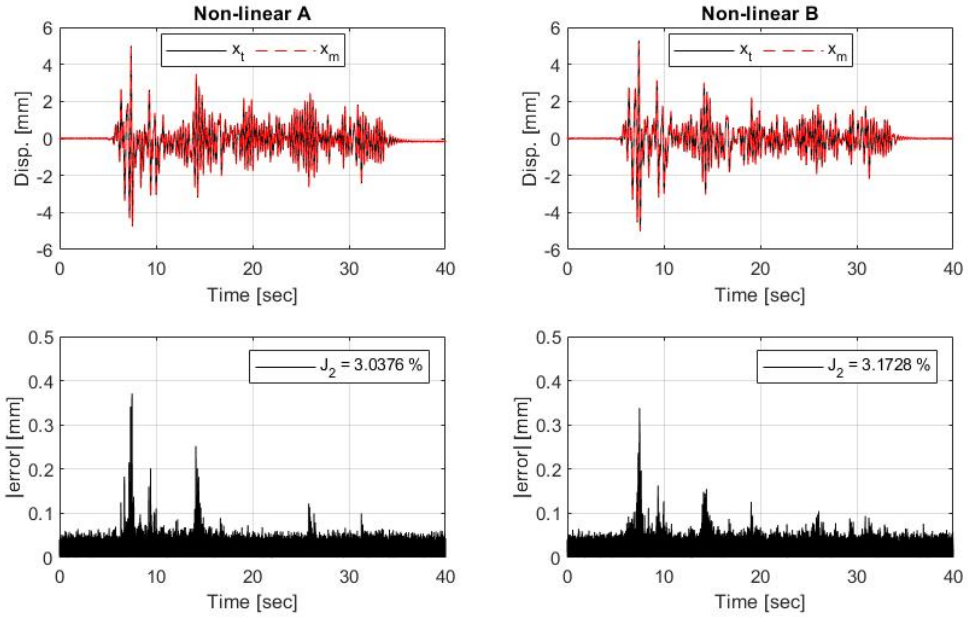

Figure 7.21: Synchronization results for non-linear simulations I and II.

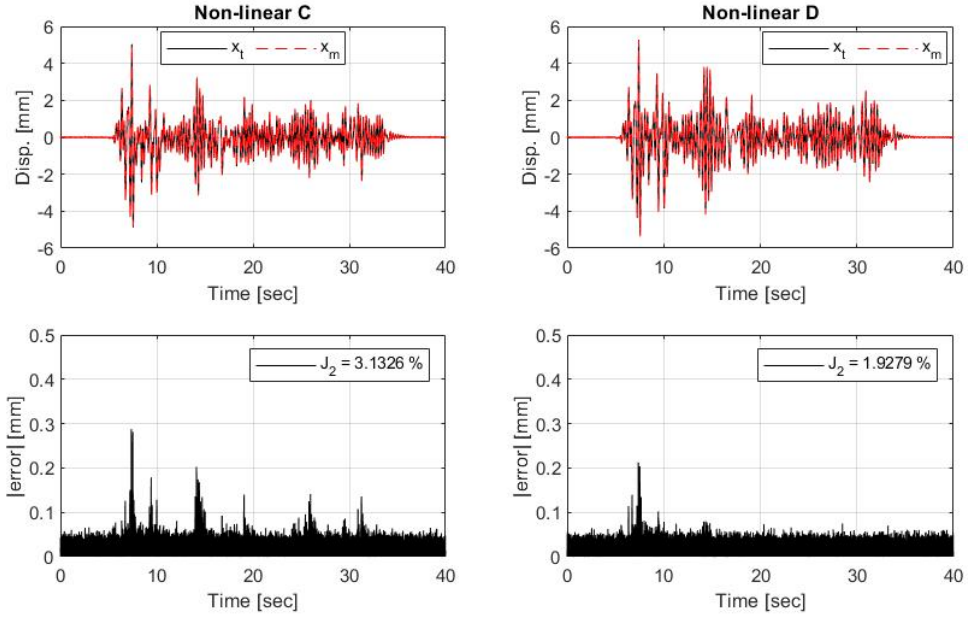

Figure 7.22: Synchronization results for non-linear simulations III and IV.

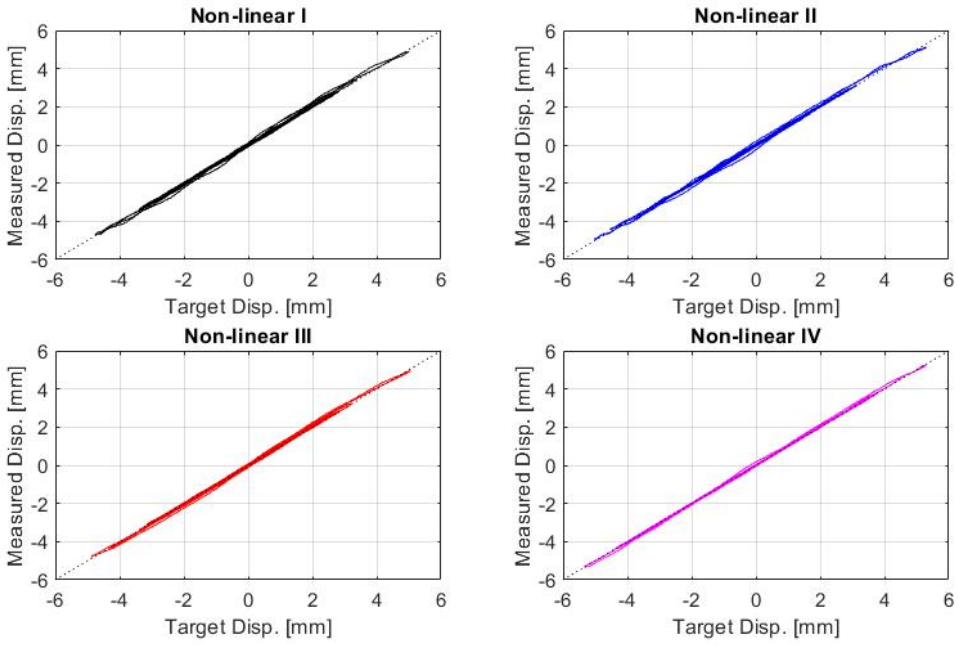

Figure 7.23: Synchronization subspace plots for non-linear simulations.

7.4 On-line stability analysis

In this section, the proposed Stability Warning Indicator (SW) is implemented and compared with the Energy Error Indicator (EEI). The EEI (Ahmadizadeh and Mosqueda, 2009) can be obtained as follow:

$$EEI = \frac{W_I - (E_k^* + E_d^* + E_s - W_{exp})}{W_I + E_E^{max}} \tag{7.19}$$

where E_k^*, E_d^* are the kinetic and dissipated energy calculated with the first derivative of displacement instead of the velocity of the numerical substructure. E_E^{max} is a nonzero elastic energy term utilized to normalize EEI when W_I is close to zero at the beginning of the test. It is important to declare that non-compensated delay implies added energy to the system, resulting in negative values of EEI. W_{exp} is the work done by experimental force over the measured displacement:

$$W_{exp} = \int -f_e^T dx_m \tag{7.20}$$

The reference structure from case IV is subjected to the Kobe earthquake with a peak ground acceleration (PGA) scaled to 40%. The maximum input work from the earthquake is around 100 Joules. This value can be computed from the integration of the reference structure. In a real RTHS experiment, the magnitude order of the input energy can be estimated from the ground motion and global properties of the structure, such as total mass and approximated damping and stiffness. Therefore, the denominator constants are selected considerably smaller, such as 1% of the maximum input work:

$$E_E^{max} = C_{SW} = 1 \text{ Joule} \tag{7.21}$$

This value is big enough to prevent large values for each indicator at the beginning of the earthquake. Also, these constants will have a negligible effect on each indicator during and after the earthquake, since C_{SW} will be relatively small compared with E_d in the denominator of equation (5.17), just like E_E^{max} will be smaller than W_I in the denominator of equation (7.19).

Before conducting the RTHS simulations with different delay values, an estimation of the critical delay is obtained with the method proposed by Gao et al. (Gao and You, 2019). This method consists of constructing the EOM of the hybrid system with some assumptions synchronization errors (delay and amplitude errors). The EOM of the hybrid system has the following equivalent mass, damping, and stiffness:

$$M_{eq} = M_n \Phi \Phi^{-1} + M_e \Phi \Delta \Phi^{-1} - C_e \Phi \Delta \delta \Phi^{-1} \tag{7.22}$$

$$C_{eq} = C_n \Phi \Phi^{-1} + M_e \Phi \Delta \omega^2 \delta \Phi^{-1} + C_e \Phi \Delta \Phi^{-1} - K_e \Phi \Delta \delta \Phi^{-1} \tag{7.23}$$

$$K_{eq} = K_n \Phi \Phi^{-1} + K_e \Phi \Delta \Phi^{-1} \tag{7.24}$$

where Φ is the modal matrix of the reference system, ω is a diagonal matrix with the natural frequencies of the reference system, δ is a diagonal matrix with the delay for each mode, and Δ is a diagonal matrix with the amplitude error for each mode. With the equivalent properties of the hybrid system, the state matrix A_{eq} is constructed as shown in Eq. (7.25):

$$A_{eq} = \begin{bmatrix} 0 & I \\ -M_{eq}^{-1} K_{eq} & -M_{eq}^{-1} C_{eq} \end{bmatrix} \tag{7.25}$$

The hybrid system is stable if the matrix A_{eq} has eigenvalues with negative real part; thus, the critical delay can be obtained by searching the minimum constant delay that produces eigenvalues with a positive real part. For the partitioning of this problem, assuming $\Delta = I$ and $\delta = \text{diag}(\tau_{cr}; \tau_{cr}; \tau_{cr})$, the critical delay is:

$$\tau_{cr} = 8.5 \text{ msec} \tag{7.26}$$

This critical delay serves as a reference for the simulations with constant delay. It is expected that simulations with delays smaller than this critical value would remain stable while running the simulations. In contrast, the opposite will result in an unstable response.

7.4.1 RTHS with constant delay

The Simulink block diagram for the simulations with constant delay is presented in Fig. 7.24, where the output of the numerical substructure, denoted as "target vector", is defined as $x_t = \left[x_n^{(1)}; \dot{x}_n^{(1)}; \ddot{x}_n^{(1)}\right]^T$ (displacement, velocity and acceleration of first degree of freedom). Then, the Delay block generates a discrete delay of the input signal x_t by a specified number of samples d, so the time delay τ is a multiple of the simulation time step. Then, the delayed boundary conditions are:

$$x_d = \left[x_n^{(1)}(t-\tau); \quad \dot{x}_n^{(1)}(t-\tau); \quad \ddot{x}_n^{(1)}(t-\tau)\right]^T \tag{7.27}$$

Finally, the outputs of the experimental substructure are described by:

$$x_m = x_n^{(1)}(t-\tau) \tag{7.28}$$

$$f_e = [k_e; \quad c_e; \quad m_e]\, x_d \tag{7.29}$$

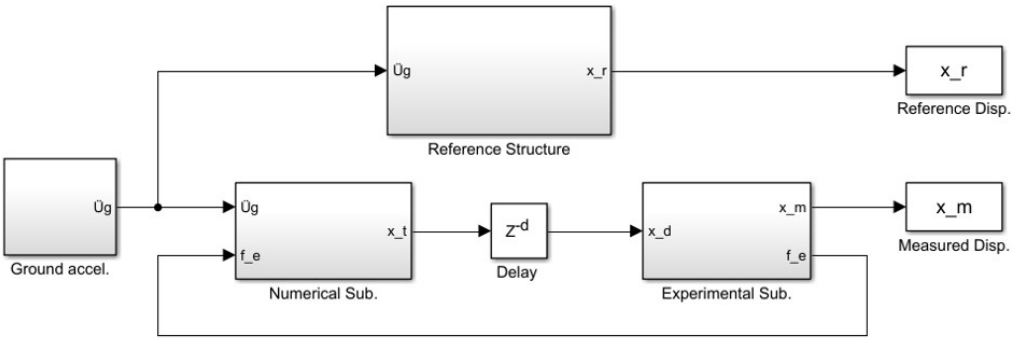

Figure 7.24: Reference structure and RTHS partitioning with delay.

Four simulations are performed with different delay values from 0 msec to 9 msec. The structure is subjected to the Kobe earthquake with a peak ground acceleration (PGA) scaled to 40%. The measured displacement of experimental substructure x_m is compared with the first degree of freedom displacement x_{r1} from the reference structure, as shown in Fig. 7.25. Measured displacements are very close to reference displacements for lower values of delay ($\tau = 0$ msec and $\tau = 0.98$ msec). Then, for higher delay $\tau = 7.1$ msec, a notorious synchronization error in displacements appear, but at least the measured displacement decays at the end of the simulation, in other words, this case is stable but evidently not accurate. This does not happen with $\tau = 9$ msec $> \tau_{cr}$, where the measured displacement grows exponentially after the earthquake reaches zero.

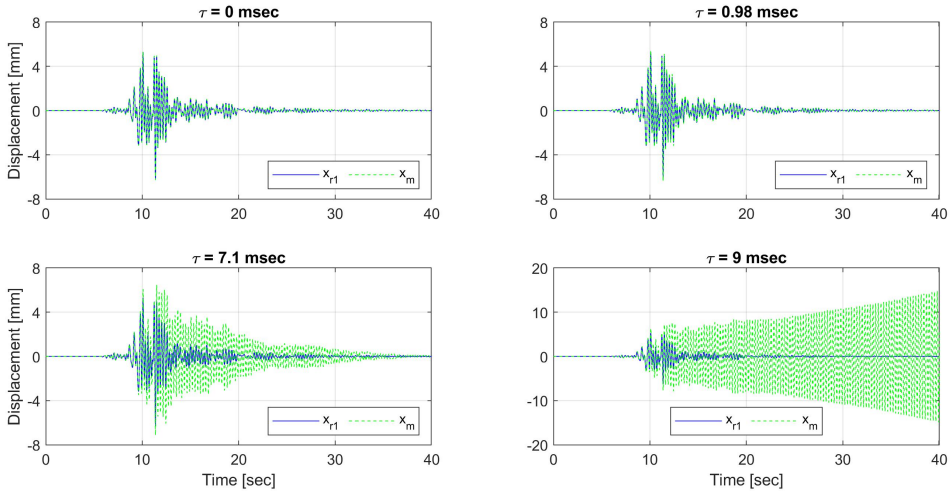

Figure 7.25: Reference and measured displacements for different delay values.

In Fig. 7.26, the error of displacement x_m respect to x_{r1} for each delay is presented, including the normalized root mean square error (NRMSE) for each case. Clearly, for $\tau = 0$ msec and $\tau = 0.98$ msec, the system is stable; while, for $\tau = 9$ msec is unstable (i.e., error grows exponentially). However, for $\tau = 7.1$ msec, the error is considerable, with $NRSME = 144\%$, but the system is still stable. It is easy to classify the case with $\tau = 9$ msec as unstable after the test. Still, it would be beneficial to detect unstable behavior before the system reaches a large response.

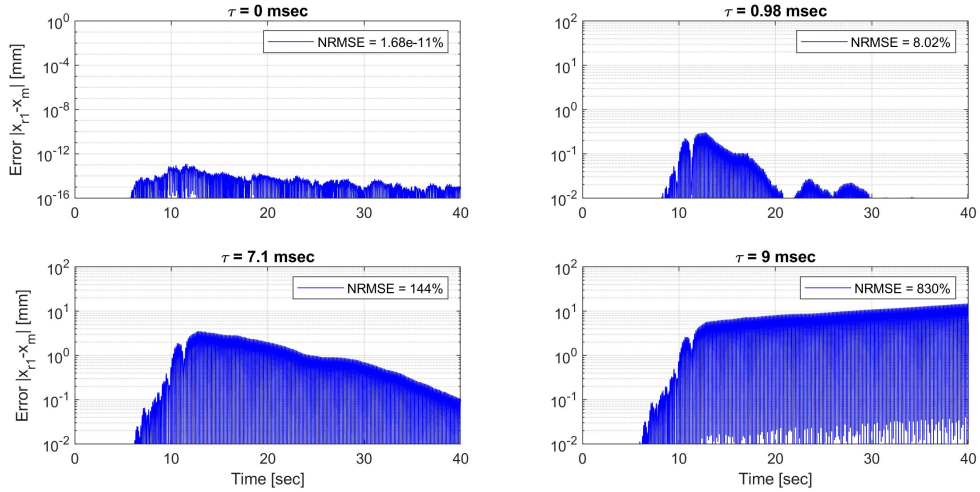

Figure 7.26: Displacement error for different delay values.

In Fig. 7.27, the SW indicator is calculated for each model scenario. For $\tau = 0$ msec, $\tau = 0.98$ msec, and $\tau = 7.1$ msec, the indicator stays under 100% during the entire test, showing the stable behavior of each simulation. In contrast, for the unstable case with $\tau = 9$ msec, the indicator exceeds 100% near

10 sec of simulation, much earlier than the instant when the system reaches the large displacements presented in Fig. 7.25. Thus, the SW indicator could help stop the simulation in time, avoiding any dangerous behavior in the RTHS test.

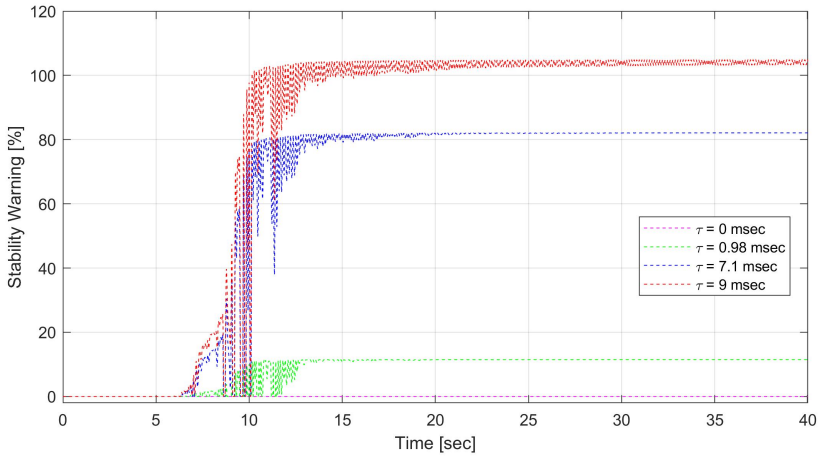

Figure 7.27: Stability warning indicator (SW) for different delay values.

For the sake of comparison, Fig. 7.28 shows the absolute value of EEI for each case scenario. The EEI grows up with higher values of delay but is not evident in which case is stable and in which it is not. For $\tau = 0$ msec, the EEI values are relatively small. Moreover, for $\tau = 0.98$ msec, the EEI stays under 15% during the test; both cases are indeed stable. However, for $\tau = 7.1$ msec, the behavior of EEI is similar to $\tau = 9$ msec before 15 sec of simulation, so it is not possible to detect instability until the earthquake signal dies out. If the EEI is utilized to stop unstable testing, it is quite challenging to define a threshold that relates EEI with instability. For example, for a threshold of $EEI = 100\%$, the simulations with $\tau = 7.1$ msec and $\tau = 9$ msec should be stopped before 10 sec, even when the simulation with $\tau = 7.1$ msec is stable and does not present any risk of large displacements. Nevertheless, it must be recognized that EEI is an excellent tool to assess the accuracy of the results from an RTHS test through a post-processing analysis.

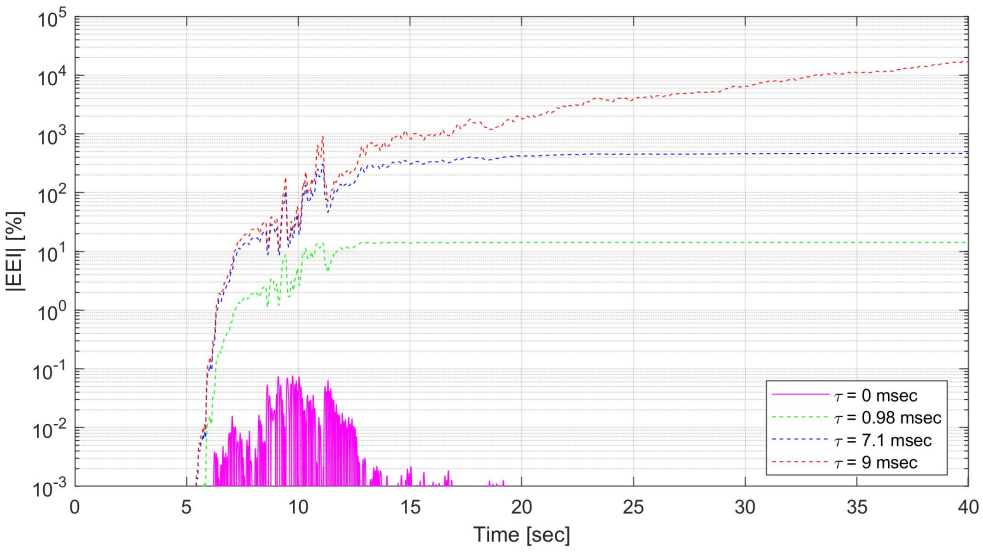

Figure 7.28: Energy error indicator (EEI) for different delay values.

7.4.2 RTHS with actuator model and dynamic compensation

In this subsection, the same partitioning as in the previous subsection is utilized, but in this case, the transfer system model is included, and adaptive compensation with different design parameters is implemented to minimize the errors produced by the transfer system. The block diagram utilized to model this problem in Simulink is presented in Fig. 7.29, where the output of the numerical substructure is the target displacement $x_t = x_n^{(1)}$ (displacement of first degree of freedom). Then, the target displacement is sent to the adaptive controller to determine the commanded displacement for the actuator. The control plant transfer function results in:

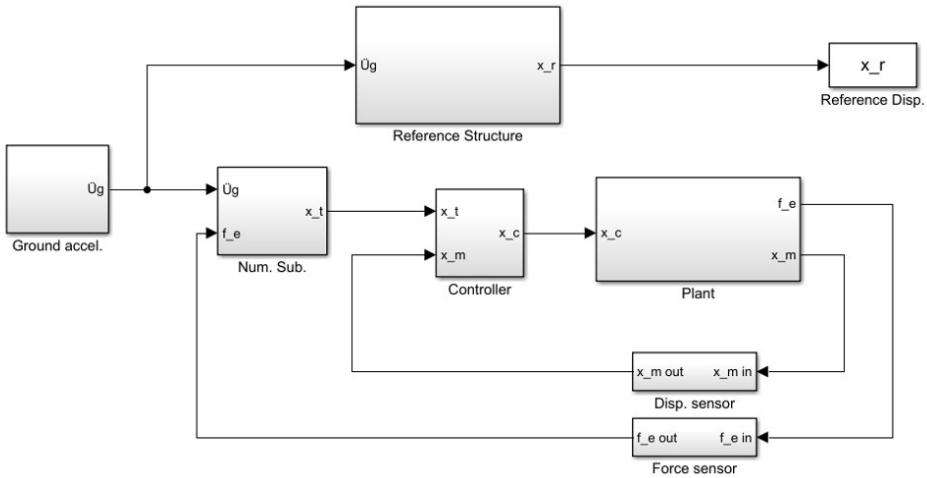

Figure 7.29: Reference structure and RTHS with compensation.

$$x_m = \frac{2.19 \times 10^{13}}{(29.1)s^5 + (1.26 \times 10^4)s^4 + (8.42 \times 10^6)s^3 + (2.33 \times 10^9)s^2 + (5.44 \times 10^{11})s + (2.17 \times 10^{13})} x_c \tag{7.30}$$

Besides, sensor noise has been added to the measured displacement x_m and the experimental force f_e using band-limited white noise (BLWN) blocks to model the physical sensors. Then, the signal x_m is sent to the controller for the adaptation process. Consequently, the signal f_e is fed back to the numerical substructure to be considered in the integration of the numerical EOM. Notice that force measurement noise could impact the experimental force power, but it has a small effect on the work done by this force due to the numerical integration process to calculate work. However, measurement noises can affect the hybrid loop, depending on the structural properties, transfer system, and dynamic compensation.

For simplicity, in this example, a first-order adaptive model-based compensation is implemented. The adaptive compensator is equivalent to the third-order compensator presented in Chapter 6, but in this case, there are only two adaptive parameters a_0 and a_1:

$$x_c = a_0 x_t + a_1 \dot{x}_t \tag{7.31}$$

The adaptation laws of a_0 and a_1 are:

$$\begin{Bmatrix} \dot{a}_0 \\ \dot{a}_1 \end{Bmatrix} = \Gamma e \begin{Bmatrix} x_m \\ \dot{x}_m \end{Bmatrix} \tag{7.32}$$

where $\Gamma = \text{diag}(\Gamma_0, \Gamma_1)$ is the adaptive gain matrix associated with the adaptation rate of parameters a_0 and a_1, respectively, and e is an estimation error of the adaptive parameters:

$$e = \frac{x_c - (a_0 x_m + a_1 \dot{x}_m)}{1 + (x_m^2 + \dot{x}_m^2)} \tag{7.33}$$

Both signals x_c and x_m are filtered with a fourth-order Butterworth low-pass filter with a cutoff frequency of 20 Hz, and $\dot{x}_m$ is obtained with the backward difference method.

This section aims to demonstrate the performance of the SW stability indicator for different compensation scenarios. Notice that the goal of the SW indicator is to detect instability during a test with a predefined compensation design, and not to tune the compensation/adaptation parameters. In these simulations, the initial adaptive parameters are selected as $a_0(t = 0) = 1$ and $a_1(t = 0) = 10/1000$ sec. With these parameters, the controller cannot compensate for the control plant delay successfully; therefore, parameter adaptation is necessary.

Four simulations are performed with different adaptive gains presented in Table 7.6, where Γ_a corresponds to a non-adaptive case, Γ_d to an optimally calibrated case (Fermandois et al., 2020), and Γ_b and Γ_c are intermediate cases of adaptation. The structure is subjected to the Kobe earthquake scaled to 40% PGA.

Table 7.6: Adaptive gains for each case.

Case	Γ_0	Γ_1
Γ_a	0	0
Γ_b	10	5
Γ_c	1×10^5	1×10^4
Γ_d	2.4×10^6	1.1×10^5

The measured displacement of experimental substructure x_m is compared with the first degree of freedom displacement x_{r1} from the reference structure in Fig. 7.30, where the case with Γ_a is unstable, while the case with Γ_b presents large measured displacements, but that decreases after the earthquake. Considering that in true RTHS tests, the reference displacement is not available, it would be difficult to distinguish if the measured displacements are correct or are associated with an unstable response. On the other hand, for Γ_c and Γ_d simulations are stable. In Fig. 7.31 the error of displacement x_m respect to x_{r1} for each adaptive gains is presented, including the normalized root mean square error (NRMSE) for each case. The cases with Γ_a present unacceptable errors, while for Γ_b, the errors are substantial, but at least decrease after the earthquake. For the cases with Γ_c and Γ_d, the errors are relatively small.

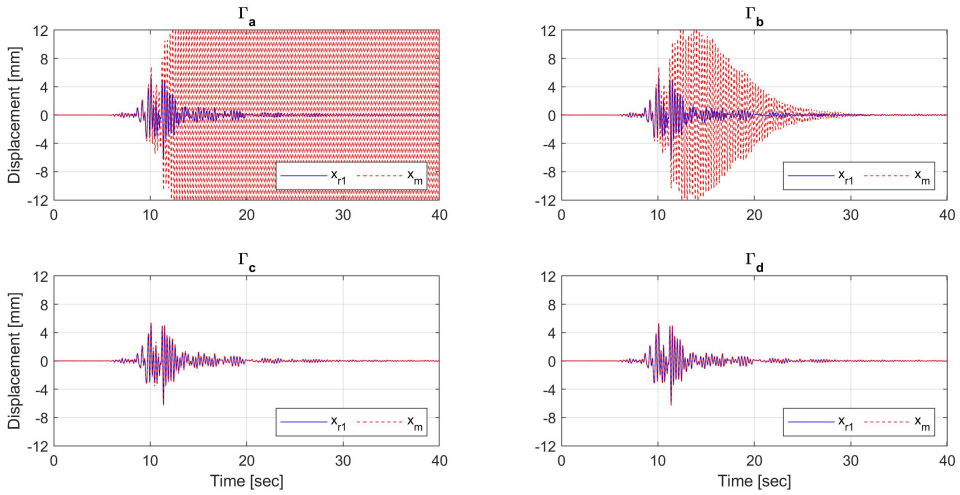

Figure 7.30: Reference and measured displacements for different adaptive gains.

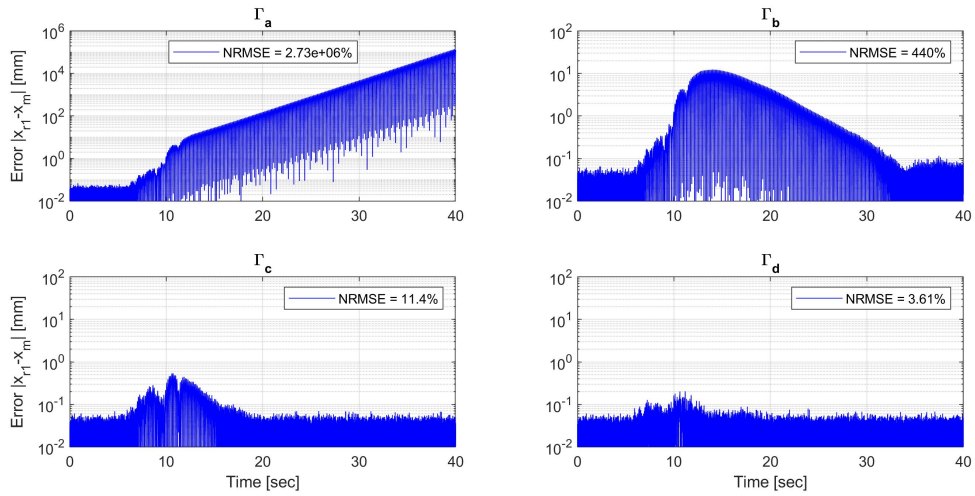

Figure 7.31: Displacement error for different adaptive gains.

The difference between each case is explained by the adaptation process presented in Fig. 7.32, where there is no adaptation for Γ_a, slow adaptation for Γ_b, and the same convergence for Γ_c and Γ_d but with different rates. The parameter a_1 is directly related to the delay compensation, so it is expected that for Γ_a and Γ_b, the non-compensated delay produces large errors in the simulations. However, the adaptation for Γ_b is apparently enough to stabilize the system during the test.

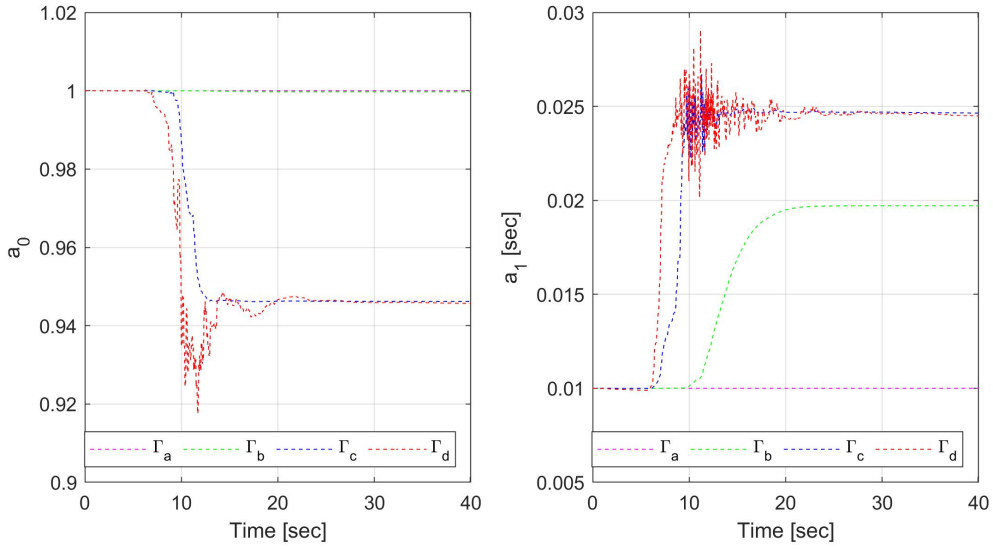

Figure 7.32: Adaptation of control parameters a_0 and a_1 for different adaptive gains.

In Fig. 7.33, the *SW* indicator for each case is presented. For Γ_c and Γ_d, the indicator is growing at the beginning of the earthquake. Then, the *SW* indicator decays due to the adaptation and good

compensation, and stays under 100% during the entire simulation, confirming the stability of these simulations. For Γ_a and Γ_b, the indicator reaches 100% near 10 sec of simulation, so much before each simulation presents large displacements. So, the stability warning indicator could help stop the simulation in time before any damage occurs in the test setup. In the particular case with Γ_b, the stability warning indicator exceeds 100% between 10 and 20 sec, consistent with the large response of the system in that interval. After 20 sec of simulation, when the controller has reached enough adaptation to compensate for the delay, the SW indicator decays below 100%. This result is consistent with the stable behavior of this case at the end of the simulation. However, this simulation could be stopped when the indicator reaches 100% to avoid the behavior shown between 10 and 20 sec.

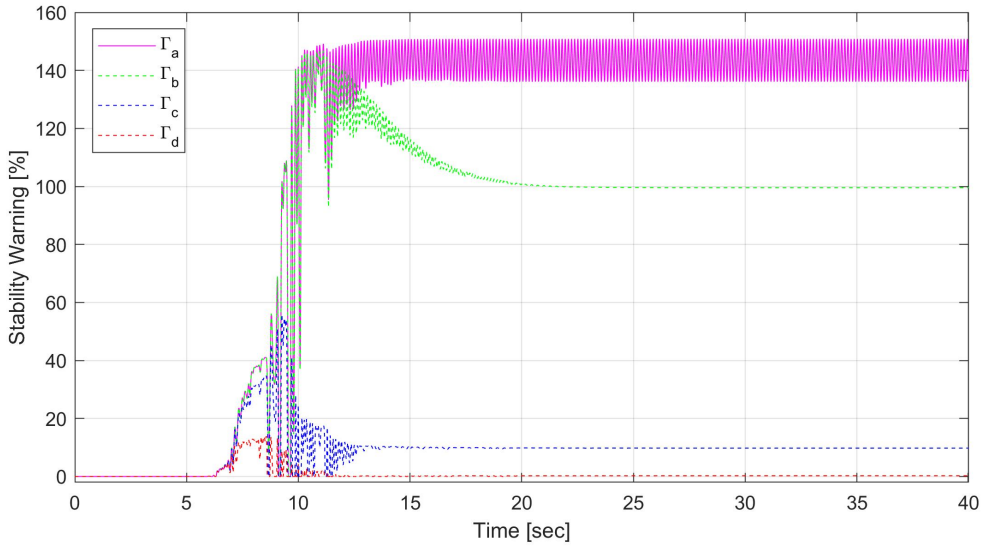

Figure 7.33: Stability warning indicator (SW) for different adaptive gains.

Moreover, notice that for Γ_b and Γ_c cases, the SW does not decay to zero at the end of the simulation. This situation occurs because of uncompensated delay during the earthquake, which causes a surplus of energy inserted into the numerical substructure. Later, when the delay is compensated, displacements and forces are too small, so the work done by the experimental forces remains constant. This effect does not happen for Γ_d, where the delay is compensated early when the earthquake strikes. The experimental substructure dissipates energy during the rest of the earthquake, leading W_F to zero and consequently, SW to zero as well.

Furthermore, the control plant in the benchmark problem is modeled as a linear time-invariant system, but in these simulations, the adaptive controller produces time-varying compensation. Therefore, the delay between target and measured displacements is a time-varying property. This scenario is a complicated situation to predict the stability of a system before the test. However, with the online analysis of the SW it is possible to detect which case results in stable behavior and which are not.

For comparison, Fig. 7.34 shows the absolute value of EEI for each adaptive case scenario. For Γ_a and Γ_b, the EEI presents large values, while for Γ_d, the EEI keeps low during the test. So, the EEI could allow lab technicians to stop the simulations with Γ_a and Γ_b, and accept the simulation with Γ_d.

However, for Γ_c case, the EEI reaches 100% before 10 sec where the displacements are small, and the controller is adapting, and the test still has good chance to give acceptable results without the risk of instability. Thus, the EEI is an excellent tool to analyze the errors after the RTHS test, but it is not reliable for detecting instability online.

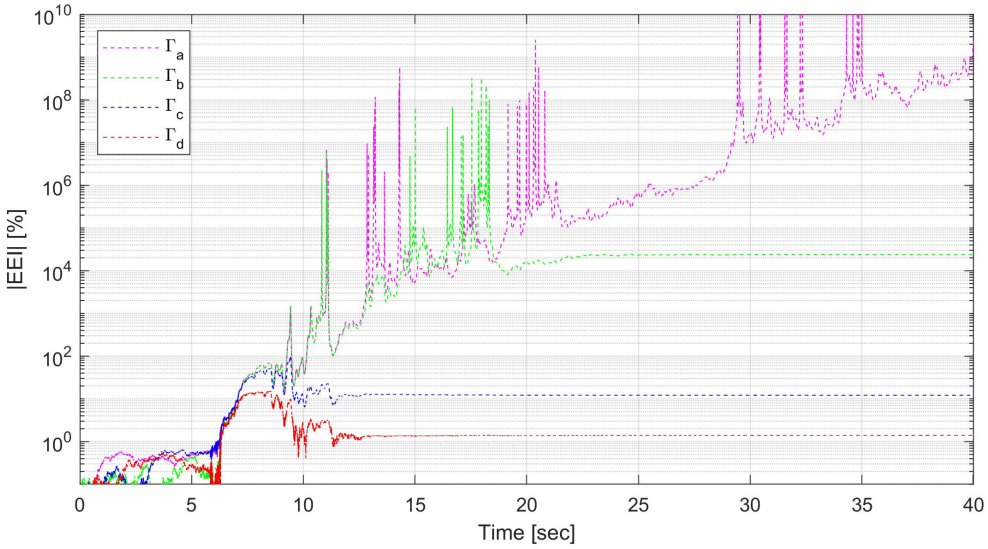

Figure 7.34: Energy error indicator (EEI) for different adaptive gains.

Additionally, in these simulations, displacement and force measurement noises do not have a notorious impact on the hybrid system response. The numerical substructure acts like a low-pass filter for the force measurement, and the adaptive compensator is not affected by the displacement noise.

7.5 Discussion

The proposed methodology was implemented in a virtual RTHS problem, but the experimental validation is still pending. Therefore, a brief discussion and summary about the application of the proposed methodology to physical RTHS test are given in this section. A step-by-step description of the compensator design is presented:

1. The first step consists of obtaining a model of the transfer system without a specimen. Therefore, system identification test must be conducted. The output of this step should be a linear model with a transfer function representation.

2. The initial compensator is designed taking the inverse of the nominal model in step 1. For the implementation, an FIR filter must be designed to obtain the numerical derivatives.

3. The adaptive compensator requires a noise filter for the adaptation process. Butterworth filter is recommended, and the order and cut-off frequency can be selected according to the experimental setup capacity.

4. Finally, the adaptive gains must be calibrated. The optimization process requires different random target displacements. These signals should be defined according to the real capacity of the transfer system in terms of frequency content and amplitudes. These signals can be created using different earthquakes and simple numerical structures with random dynamical properties. Additionally, random virtual control plants are required to evaluate the robustness of the compensator. These virtual control plants can be defined by introducing uncertainty in the identified model of the transfer system. It is crucial that these control plants show significant discrepancies with the original model in order to enforce the adaptation of the compensator to achieve good results. Then, a number of simulations for each set of adaptive gains are selected to obtain a representative sample of the random inputs and an indicator is selected to evaluate the performance of each set of adaptive gains. Finally, the optimization can be carried out to find the optimal adaptive gain matrix.

Additionally, some aspects of the experimental design related to stability and compensation are discussed:

- The partitioning sensitivity must be studied before the test. Tools like the Predictive Stability Indicator (Maghareh et al., 2017) can be applied to quantify the critical delay of a particular partitioning. It is crucial to avoid extremely sensitive cases that become unstable with small non-compensated delays. For example, if the critical delay of a particular substructuring is about 1 msec, and the actuator's delay without compensation is about 20 msec, then even with an excellent compensator, the system is still susceptible to instability. Notice that it is necessary to estimate or measure the dynamic properties of the experimental substructure to study the stability of a hybrid system.
- The experimental substructures must be selected according to the capacity of the transfer system. Extremely stiff specimens could exceed the force capacity of the actuator, and extremely heavy specimens can lead to instability of the control plant.

8 Conclusions

8.1 Conclusions

In this study, an adaptive model-based compensation technique for real-time hybrid simulation is proposed and implemented in numerical simulations. The novel aspect of the proposed method is that the initial conditions of the controller are formulated independently from the physical specimen connected to the actuator.

The proposed compensation method is founded in model-based compensation strategies, that depend on a model of the transfer system and the physical specimen. Servo-hydraulic actuators are often utilized as transfer systems in RTHS to impose the numerical response on the physical specimen. The most utilized dynamic model for servo-hydraulic actuators was studied to show the synchronization errors between commanded and measured displacements. The dynamic model allows analyzing the synchronization errors in terms of amplitude and delay errors. Two aspects should be highlighted: (i) the control plant dynamics depends on the commanded frequencies, and (ii), the control plant dynamics depends on the dynamic properties of the connected physical specimen.

The adaptive model-based compensation method consists of a feedforward model-based controller for transfer system without a specimen, and then an adaptive law that captures the specimen interaction and updates the feedforward control parameters during the test. The initial conditions of the controller are taken from a transfer function model of the transfer system, allowing to avoid system identification that includes the physical specimen. Then, the adaptive law is calibrated off-line, since the controller is capable to reach a quick adaptation and excellent tracking performance, thus, the same controller is capable to compensate the transfer system dynamics with different experimental substructures or time-varying properties.

Special attention is given to the adaptive gains calibration since the controller's performance is highly dependent on the adaptive law. Extremely low adaptation may lead to poor delay compensation, while extremely high gains may result in catastrophic adaptation. The proposed calibration process consists of the optimization of the adaptive gain for a set of numerical simulations with different random parameters as entries.

The designed and calibrated controller was implemented in a virtual RTHS benchmark problem, specially designed to prove different compensation methods. Since, the proposed compensation method has excellent results for the benchmark problem, more unfavorable cases have been added to include different experimental substructures and non-linear models with stiffness and strength degradation. The designed controller demonstrates an excellent tracking performance and robustness in all different scenarios.

On the other hand, the effect of the actuator delay on the stability of a hybrid system was analyzed. The partitioning in RTHS is a crucial aspect that affects the sensitivity of a hybrid system against the time delay in the hybrid loop. Different predictive stability indicators allow evaluating the critical delay for specific configurations of the numerical and experimental substructure. These techniques allow to avoid extremely sensitive cases, which even with excellent dynamics compensation may lead to instability or reliability problems. However, predictive stability indicators require the dynamical properties of the experimental substructure, which are often subjected to high uncertainty. Therefore, an on-line stability analysis was performed through an energy analysis of the numerical substructure

equation of motion

The stability warning indicator (SW) was developed to detect instability of the hybrid system during the test. The features of the proposed indicator to detect instability is demonstrated through numerical simulations with constant delay and simulations, including an actuator model with adaptive compensation for different design scenarios. The stability warning indicator (SW) allows the detection of unstable behavior before the system reaches large displacements that can damage the experimental substructure or laboratory equipment. The proposed indicator only requires the measured force from the experimental substructure and information from the numerical substructure. Hence, it is independent of the compensation method and does not require a model of the experimental substructure or the transfer system (i.e., actuation system).

This stability indicator can be implemented to stop an RTHS test that is rendered unstable automatically. The test should be stopped if the SW reaches 100% (i.e., it is unnecessary to stop a test with a $SW < 100$). So, this indicator is an excellent complement to any compensation method. It provides further safety guarantees to the test, especially for adaptive compensation if there is considerable uncertainty in the plant or the controller's adaptation capacity. It is worth mentioning that the proposed indicator provides safety for the test, but it does not ensure accuracy compared to the reference structure's true response. However, priority should always be given to conducting a safe experiment. Then, the reliability of the results could be studied in detail after the test has ended.

8.2 Future studies

Some of the possible future studies are discussed as follows:

- Experimental validation of the proposed compensation method is expected. It should be noted that an adaptive compensator capable to compensate different and complex experimental substructures, will expand the testing versatility of the laboratory.
- The controller presents excellent results for uncertain linear cases and very good results for non-linear cases. However, the performance for non-linear cases can be improved by combining the adaptive controller with a feedback controller. However, the design of a feedback controller without a model of control plant including an uncertain experimental substructure could be a challenging task. First, every feedback controller may affect the stability of the controlled system, so adding a feedback component without considering the specimen interaction could be dangerous. Furthermore, the feedback displacement may introduce noise to the system. This noise can be reduced with filters; however, noise filters can add delay to the feedback signal deteriorating the feedback controller performance. Other filters like state estimators depend on a model of the control plant, so the specimen interaction may affect this kind of filter.
- The proposed methodology was developed and implemented for RTHS with a single actuator, so future studies may consider adaptive compensation for multiple actuators. In this case, the interaction with the physical specimen and between actuators must be considered.
- Finally, the effectiveness of the SW indicator was demonstrated for linear systems. Future work will consider non-linear systems and the corresponding experimental validation of the proposed indicator.

References

Ahmadizadeh, M. and Mosqueda, G. (2009). Online energy-based error indicator for the assessment of numerical and experimental errors in a hybrid simulation. *Engineering Structures*, 31(9):1987–1996.

Ashasi-Sorkhabi, A., Malekghasemi, H., and Mercan, O. (2015). Implementation and verification of real-time hybrid simulation (RTHS) using a shake table for research and education. *JVC/Journal of Vibration and Control*, 21(8):1459–1472.

Bas, E. E. and Moustafa, M. A. (2020). Performance and Limitations of Real-Time Hybrid Simulation with Nonlinear Computational Substructures. *Experimental Techniques*.

Bonnet, P., Lim, C., Williams, M., Blakeborough, A., Neild, S., Stoten, D., and Taylor, C. (2007). Real-time hybrid experiments with newmark integration, mcsmd outer-loop control and multi-tasking strategies. *Earthquake Engineering & Structural Dynamics*, 36(1):119–141.

Carrion, J. E. and Spencer, B. F. (2007). Model-based Strategies for Real-time Hybrid Testing. Technical Report NSEL-006, Department of Civil and Environmental Engineering, University of Illinois at Urbana-Champaign, Urbana, IL.

Chae, Y., Kazemibidokhti, K., and Ricles, J. M. (2013). Adaptive time series compensator for delay compensation of servo-hydraulic actuator systems for real-time hybrid simulation. *Earthquake Engineering & Structural Dynamics*, 42(11):1697–1715.

Chen, C. (2007). *Development and numerical simulation of hybrid effective force testing method*. Lehigh University.

Chen, C. and Ricles, J. M. (2010). Tracking Error-Based Servohydraulic Actuator Adaptive Compensation for Real-Time Hybrid Simulation. *Journal of Structural Engineering*, 136(4):432–440.

Chen, P.-C., Chang, C.-M., Spencer, Jr., B. F., and Tsai, K.-C. (2015). Adaptive model-based tracking control for real-time hybrid simulation. *Bulletin of Earthquake Engineering*, 13(6):1633–1653.

Chen, P.-c. and Chen, P.-c. (2020). Robust stability analysis of real-time hybrid simulation considering system uncertainty and delay compensation. *Smart Structures and Systems*, 25(6):719–732.

Dermitzakis, S. N. and Mahin, S. (1985). Development of substructuring techniques for on-line computer controlled seismic performance testing. Technical Report UCB/EERC-85/04, University of California, Berkeley.

Dyke, S. J., Spencer Jr., B. F., Quast, P., and Sain, M. (1995). Role of Control-Structure Interaction in Protective System Design. *Journal of Engineering Mechanics*, 121(2):322–338.

Fermandois, G., Galmez, C., and Valdebenito, M. (2020). Optimal gain calibration of adaptive model-based compensation for real-time hybrid simulation testing. In *17th World Conference on Earthquake Engineering (17WCEE)*, Sendai, Japan.

Gálmez, C. and Fermandois, G. (2020). Online Stability Analysis for Real-Time Hybrid Simulation Testing. *Frontiers in Built Environment*, 6(August):1–14.

Gao, X., Castaneda, N., and Dyke, S. J. (2013). Real time hybrid simulation: from dynamic system, motion control to experimental error. *Earthquake Engineering & Structural Dynamics*, 42(6):815–832.

Gao, X. S. and You, S. (2019). Dynamical stability analysis of MDOF real-time hybrid system. *Mechanical Systems and Signal Processing*, 133:106261.

Guo, T., Chen, C., Xu, W., and Sanchez, F. (2014). A frequency response analysis approach for quantitative assessment of actuator tracking for real-time hybrid simulation. *Smart Materials and Structures*, 23(4):045042.

Hakuno, M., Shidawara, M., and Hara, T. (1969). Dynamic destructive test of a cantilever beam controlled by an analog-computer. *Trans Jpn Soc Civ Eng*, 171:1–9.

Hilber, H. M., Hughes, T. J., and Taylor, R. L. (1977). Improved numerical dissipation for time integration algorithms in structural dynamics. *Earthquake Engineering & Structural Dynamics*, 5(3):283–292.

Horiuchi, T., Inoue, M., Konno, T., and Namita, Y. (1999). Real-time hybrid experimental system with actuator delay compensation and its application to a piping system with energy absorber. *Earthquake Engineering & Structural Dynamics*, 28(10):1121–1141.

Horiuchi, T., Nakagawa, M., Sugano, M., and Konno, T. (1996). Development of a real-time hybrid experimental system with actuator delay compensation. In *In Proc. 11th World Conf. Earthquake Engineering*, page Paper No. 660.

Ioannou, P. A. and Sun, J. (2012). *Robust adaptive control*. Courier Corporation.

Kennedy, J. and Eberhart, R. (1995). Particle Swarm Optimization. In *Proceedings of the IEEE International Conference on Neural Networks. Perth, Australia*, pages pp. 1942–1945, Perth, Australia.

Khalil, H. K. and Grizzle, J. W. (2002). *Nonlinear systems*, volume 3. Prentice hall Upper Saddle River, NJ.

Maghareh, A., Dyke, S., Rabieniaharatbar, S., and Prakash, A. (2017). Predictive stability indicator: a novel approach to configuring a real-time hybrid simulation. *Earthquake Engineering & Structural Dynamics*, 46(1):95–116.

Maghareh, A., Silva, C. E., and Dyke, S. J. (2018). Servo-hydraulic actuator in controllable canonical form: Identification and experimental validation. *Mechanical Systems and Signal Processing*, 100:398–414.

McCrum, D. and Williams, M. (2016). An overview of seismic hybrid testing of engineering structures. *Engineering Structures*, 118:240–261.

Mei, Z., Wu, B., Bursi, O. S., Xu, G., Wang, Z., Wang, T., Ning, X., and Liu, Y. (2019). Hybrid simulation with online model updating: Application to a reinforced concrete bridge endowed with tall piers. *Mechanical Systems and Signal Processing*, 123:533–553.

Najafi, A. and Spencer Jr., B. F. (2020). Validation of model-based real-time hybrid simulation for a lightly-damped and highly-nonlinear structural system. *Journal of Applied and Computational Mechanics*.

Nakashima, M. (2020). Hybrid simulation: An early history. *Earthquake Engineering and Structural Dynamics*, 49(10):949–962.

Nakashima, M., Kato, H., and Takaoka, E. (1992). Development of real-time pseudo dynamic testing. *Earthquake Engineering & Structural Dynamics*, 21(1):79–92.

Nakashima, M., Nagae, T., Enokida, R., and Kajiwara, K. (2018). Experiences, accomplishments, lessons, and challenges of E-defense—Tests using world's largest shaking table. *Japan Architectural Review*, 1(1):4–17.

Newmark, N. M. (1959). A method of computation for structural dynamics. *Journal of the engineering mechanics division*, 85(3):67–94.

Ning, X., Wang, Z., Wang, C., and Wu, B. (2020a). Adaptive Feedforward and Feedback Compensation Method for Real-time Hybrid Simulation Based on a Discrete Physical Testing System Model Adaptive Feedforward and Feedback Compensation Method for. *Journal of Earthquake Engineering*, 00(00):1–23.

Ning, X., Wang, Z., and Wu, B. (2020b). Kalman filter-based adaptive delay compensation for benchmark problem in real-time hybrid simulation. *Applied Sciences (Switzerland)*, 10(20):1–19.

Ou, G., Dyke, S. J., and Prakash, A. (2017). Real time hybrid simulation with online model updating: An analysis of accuracy. *Mechanical Systems and Signal Processing*, 84:223–240.

Ou, G., Ozdagli, A. I., Dyke, S. J., and Wu, B. (2015). Robust integrated actuator control: Experimental verification and real-time hybrid-simulation implementation. *Earthquake Engineering and Structural Dynamics*, 44(3):441–460.

Ouyang, Y., Shi, W., Shan, J., and Spencer, B. F. (2019). Backstepping adaptive control for real-time hybrid simulation including servo-hydraulic dynamics. *Mechanical Systems and Signal Processing*, 130:732–754.

Palacio-Betancur, A. and Gutierrez Soto, M. (2019). Adaptive tracking control for real-time hybrid simulation of structures subjected to seismic loading. *Mechanical Systems and Signal Processing*, 134:106345.

Park, D. U., Yun, C. B., Lee, J. W., Nagata, K., Watanabe, E., and Sugiura, K. (2005). On-line pseudo-dynamic network testing on base-isolated bridges using internet and wireless internet. *Experimental Mechanics*, 45(4):331–343.

Peiris, L. H., Plummer, A. R., and du Bois, J. L. (2020). Passivity control for nonlinear real-time hybrid tests. *Proceedings of the Institution of Mechanical Engineers, Part I: Journal of Systems and Control Engineering*, page 095965182095900.

Phillips, B. M. and Spencer Jr, B. F. (2011). Model-based feedforward-feedback tracking control for real-time hybrid simulation. Technical report, Newmark Structural Engineering Laboratory. University of Illinois at Urbana-Champaign.

Shao, X. and Griffith, C. (2013). An overview of hybrid simulation implementations in NEES projects. *Engineering Structures*, 56:1439–1451.

Silva, C. E., Gomez, D., Maghareh, A., Dyke, S. J., and Spencer, B. F. (2020). Benchmark control problem for real-time hybrid simulation. *Mechanical Systems and Signal Processing*, 135:106381.

Simpson, T., Dertimanis, V. K., and Chatzi, E. N. (2020). Towards Data-Driven Real-Time Hybrid Simulation: Adaptive Modeling of Control Plants. *Frontiers in Built Environment*, 6(September).

Sivaselvan, M. V. and Reinhorn, A. M. (2000). Hysteretic Models for Deteriorating Inelastic Structures. *Journal of Engineering Mechanics*, 126(6):633–640.

Takahashi, Y. and Fenves, G. L. (2006). Software framework for distributed experimental–computational simulation of structural systems. *Earthquake Engineering & Structural Dynamics*, 35(3):267–291.

Takanashi, K., Udagawa, K., Seki, M., Okada, T., and Tanaka, H. (1975). Nonlinear earthquake response analysis of structures by a computer actuator on-line system. (Part 1: details of the system.). *Transcript of the Architectural institute of Japan*, 229:77–83.

Tang, Z., Dietz, M., Hong, Y., and Li, Z. (2020). Performance extension of shaking table-based real-time dynamic hybrid testing through full state control via simulation. *Structural Control and Health Monitoring*, 27(10):1–19.

Tao, J. and Mercan, O. (2019). A study on a benchmark control problem for real-time hybrid simulation with a tracking error-based adaptive compensator combined with a supplementary proportional-integral-derivative controller. *Mechanical Systems and Signal Processing*, 134:106346.

Tsokanas, N., Wagg, D., and Stojadinović, B. (2020). Robust Model Predictive Control for Dynamics Compensation in Real-Time Hybrid Simulation. *Frontiers in Built Environment*, 6(August):1–17.

Verma, M. and Sivaselvan, M. V. (2019). Impedance matching control design for the benchmark problem in real-time hybrid simulation. *Mechanical Systems and Signal Processing*, 134:106343.

Wallace, M., Sieber, J., Neild, S. A., Wagg, D. J., and Krauskopf, B. (2005a). Stability analysis of real-time dynamic substructuring using delay differential equation models. *Earthquake Engineering & Structural Dynamics*, 34(15):1817–1832.

Wallace, M., Wagg, D., and Neild, S. (2005b). An adaptive polynomial based forward prediction algorithm for multi-actuator real-time dynamic substructuring. *Proceedings of the Royal Society A: Mathematical, Physical and Engineering Sciences*, 461(2064):3807–3826.

Wang, X., Hutchinson, T. C., Astroza, R., Conte, J. P., Restrepo, J. I., Hoehler, M. S., and Ribeiro, W. (2017). Shake table testing of an elevator system in a full-scale five-story building. *Earthquake Engineering and Structural Dynamics*, 46(3):391–407.

Wang, Y.-P., Lee, C.-L., and Yo, T. (2001). Modified state-space procedure for pseudodynamic testing. *Earthquake Engineering and Structural Dynamics*, 30(1):59–80.

Wang, Z., Yan, X., Ning, X., and Wu, B. (2020). Test Verification of Two-Stage Adaptive Delay Compensation Method for Real-Time Hybrid Simulation. *Shock and Vibration*, 2020:1–14.

Xu, D., Zhou, H., Shao, X., and Wang, T. (2019a). Performance study of sliding mode controller with improved adaptive polynomial-based forward prediction. *Mechanical Systems and Signal Processing*, 133:106263.

Xu, W., Chen, C., Guo, T., and Chen, M. (2019b). Evaluation of frequency evaluation index based compensation for benchmark study in real-time hybrid simulation. *Mechanical Systems and Signal Processing*, 130:649–663.

Zhang, R., Phillips, B. M., Taniguchi, S., Ikenaga, M., and Ikago, K. (2017). Shake table real-time hybrid simulation techniques for the performance evaluation of buildings with inter-story isolation. *Structural Control and Health Monitoring*, 24(10):1–19.

Zhao, J., French, C., Shield, C., and Posbergh, T. (2003). Considerations for the development of real-time dynamic testing using servo-hydraulic actuation. *Earthquake Engineering & Structural Dynamics*, 32(11):1773–1794.